

Insights from Mapping Distributed and Focused Volcanism

by

Rebecca Collette Bussard

A dissertation accepted and approved in partial fulfillment of the

requirements for the degree of

Doctor of Philosophy

in Earth Sciences

Dissertation Committee:

Josef Dufek, Co-Chair

Meredith Townsend, Co-Chair

Kathy Cashman, Core Member

Alan Rempel, Core Member

Sarah Cooley, Institutional Representative

University of Oregon

Spring 2024

© 2024 Rebecca Collette Bussard
This work is licensed under a Creative
Commons Attribution License



DISSERTATION ABSTRACT

Rebecca Collette Bussard

Doctor of Philosophy in Earth Sciences

Title: Insights from Mapping Distributed and Focused Volcanism

This dissertation utilizes a variety of mapping techniques to explore surface and subsurface processes at different volcanic systems. As each volcanic system is unique, it is important to understand which mapping methods can be applied to vents contained within the system and which will face more challenges. This dissertation details the use of statistical analysis and remote sensing for addressing questions of magma transport/storage as well as volcanic surface change at distributed and focused systems.

To begin, Voronoi tessellations are used to map the area between vents in a variety of distributed volcanic fields. The distributions of vent areas are then compared to distributions of areas between randomly simulated vents. If the distribution of vent areas across a volcanic field differs from a random distribution, then clustering is occurring in this field; from this, causes of clustering such as regional tectonic forces, magma supply rates, and magma storage can be explored. Five of the six fields analyzed experience clustering and visualize the length scale at which clustering occurs through Kernel Density Estimation.

The work then shifts from distributed to focused volcanism, specifically Mt. St. Helens, a stratovolcano in southwest Washington. A computationally inexpensive neural network developed with open access code classifies snow cover in optical imagery covering the Mt. St. Helens region through time. The snow cover estimates produced through classification are then compared with coherence maps from Sentinel-1 Interferometric Synthetic Aperture Radar (InSAR) data to quantify how snow cover effects coherence (signal strength). Snow cover reduces coherence up to

70% and widespread snow cover can almost entirely mask out uplift greater than one centimeter from an inflating magma source.

Finally, InSAR timeseries and velocity data over Medicine Lake volcano measures ground deformation from 2017-2021. The vertical velocity data shows subsidence across the broad edifice that increases in magnitude within the volcano's central caldera to ~ 1 cm/yr. Markov Chain Monte Carlo (MCMC) modeling constrains several parameters of a potential volume loss source at depth beneath the volcano, including depth and volume change for a point source and depth, length, wide, opening, and strike for a rectangular sill. The highest likelihood point source sits at 7.7 km depth with a volume decrease of $0.0013 \text{ km}^3/\text{yr}$, and for the sill source sits at 10.1 km depth with a volume decrease of $0.0016 \text{ km}^3/\text{yr}$. Subsidence due to edifice loading is also analytically modeled and is assumed to occur (subtracted from the InSAR vertical deformation signal). When the MCMC is rerun taking loading into account, source depths become shallower and volume changes decrease.

This dissertation includes previously submitted and unpublished co-authored material.

CURRICULUM VITAE

NAME OF AUTHOR: Rebecca Collette Bussard

GRADUATE AND UNDERGRADUATE SCHOOLS ATTENDED:

University of Oregon, Eugene, OR, USA
Pennsylvania State University, PA, USA

DEGREES AWARDED:

Doctor of Philosophy, Earth Sciences, 2024, University of Oregon
Bachelor of Science, Physics, 2019, Pennsylvania State University

AREAS OF SPECIAL INTEREST:

Remote sensing
Volcanology

PROFESSIONAL EXPERIENCE:

USIP Intern, UNAVCO, 2021-2022

Graduate Employee, Department of Earth Sciences, University of Oregon, 2019-2024

Research Assistant, Pennsylvania State University, 2018-2019

Research Experience Undergrad (REU) Intern, University of Texas at Austin, 2017

GRANTS, AWARDS, AND HONORS:

Marthe E. Smith Memorial Science Scholarship, University of Oregon, 2022

ISCE+ Short Course Memoriam, UNAVCO, 2021-2023

Weiser Scholarship, University of Oregon, 2021

Travel Grant, AGU, 2018

Erickson Discovery Grant, Pennsylvania State University, 2018

Elsbach Physics Scholarship, Pennsylvania State University, 2017-2019

Braddock Scholarship, Pennsylvania State University, 2015-2019

Penn State Bookstore Scholarship, Pennsylvania State University, 2015-2019

PUBLICATIONS:

Bussard, R., Harper, C., Cashman, K. & Karlstrom, L. (2024). *An Area-Based Methodology for Deriving Intrinsic Length Scales of Distributed Volcanic Fields*. Manuscript accepted for publication.

Bussard, R., Dufek, J., Wauthier, C. & Townsend, M. (2024). *Quantifying the Effects of Volcano Snow Cover on InSAR Coherence using a Computationally Inexpensive Neural Network*. Manuscript in prep.

Bussard, R., Dufek, J., Townsend, M. & Wauthier, C. (2024). Investigating Decades-Long Subsidence at Medicine Lake Volcano using InSAR, GNSS, and MCMC Modeling. Manuscript in prep.

Kirsten, S., Wauthier, C., **Bussard, R.**, Higgins, M. & LaFemina, P.C. (2020). Assessment of Mitigation Strategies for Tropospheric Phase Contributions to InSAR Time-Series Datasets over Two Nicaraguan Volcanoes. *Remote Sensing*, 782.

Roman, D.C., LaFemina, P.C., **Bussard, R.**, Stephens, K., Wauthier, C., Higgins, M., et al. (2019). *Mechanisms of Unrest and Eruption at Persistently Restless Volcanoes. Insights from the 2015 Eruption of Telica Volcano, Nicaragua*. *Geochemistry, Geophysics, Geosystems*, 20, 4162-4183.

ACKNOWLEDGMENTS

There are so many people in my life that without whom I wouldn't have made it to the point where I'd be writing these acknowledgements in my dissertation. It's impossible to elaborate on all of the ways I've been helped over my lifetime and particularly over the past five years, but I will attempt to show as much of my gratitude as I can here.

To Joe and Meredith, I will always be appreciative of you both for taking me on as a student and letting me grow as a part of your labs. I always enjoyed meeting with you, whether it was discussing science, dealing with issues I was facing, or talking about board games and the newest season of Love is Blind. Kathy, thank you for always encouraging me to ask questions and pursue creative avenues of understanding volcanoes. Alan, and Sarah, I thank you for all of your help and contributions over the last five years.

To the Penn State IGG lab, in particular Christelle, Kirsten and Judit. Kirsten and Judit, you are truly the best mentor graduate students I could have asked for. From helping me process my first interferogram to helping me pin up my poster at my first AGU, you two have been the ultimate support network from the start. Christelle, you introduced me to the field of Earth Science and have continued to help me grow as a student, a researcher, and a person since I first met you. Thank you for always supporting me and for being one of the greatest advisors and people I've ever had the fortune to work with.

To the other mentors that have helped me grow. Chris, interning with you was an amazing experience that not only helped me grow as a remote senser but also helped me feel more connected in the InSAR community. Professor Robinett, the genuine care you gave towards the task of advising me was instrumental in me completing my degree at Penn State and this dissertation.

To the people who are great colleagues but more importantly wonderful friends here at UO, thank you for bringing me joy, laughs, and support over the last five years. Angela, Helena, and Kathy, you are all so genuinely talented and wonderful people, it's been so fun having you all as friends. Paul and Renee, you both are always there to brighten my day with board games, D&D, movies, and have been fiercely supportive to me whenever I've needed encouragement. Lissie, Nicole, Sydney, and Tara, there isn't much more to say that I haven't already tried to impress on you during our time together. You have been with me all five years and have each been lifelines when I have needed you. To have four brilliant researchers, kind souls, and fun friends for the full duration of my PhD is a blessing I will always appreciate.

To Marlee, you have been a constant source of support from across the country and are always there for me whenever I need you. Thank you for always bringing so much fun into my life and never letting me settle for anything less than what you've thought I was capable of. To have a friend like you is a gift and I am forever grateful.

To Jacob, you have my heart always. Long distance for years is not an easy task, and your willingness to adapt to whatever I have needed has been amazing beyond words. You are thoughtful, kind, funny, and so important to me. You have been an amazing friend and a wonderful partner and have picked me up from my lowest points so many times over the past nine years. Thank you for everything, my love.

To my mom and dad, I can never say enough that will encompass everything you have done for me. The continual sacrifices you made for me and my education are innumerable. Your love crafted an iron clad sense of self and willpower within me that were tested constantly throughout my graduate school experience but never faltered. And to my mom now, thank you for always pushing me towards greater heights and being there for me in every way.

DEDICATION

1, 2, 3, 4, can I have a little more? 5, 6, 7 8 9 10, I love you. -The Beatles, All Together Now

This dissertation is dedicated to my dad, thank you for always believing in me. I wish you could be here with me now, but I know you are proud of how much I've grown and how fiercely stubborn I have been when met with the challenges that have come my way.

TABLE OF CONTENTS

Chapter	Page
I. INTRODUCTION	17
1.1 Background.....	17
1.1.1 What We Map at Volcanic Systems	17
1.1.2 How We Map Volcanic Systems	19
1.1.3 Why We Map Volcanic Systems	21
1.2 Outline.....	22
II. AN AREA-BASED METHODOLOGY FOR DERIVING INTRINSIC LENGTH SCALES OF DISTRIBUTED VOLCANIC FIELDS	24
2.1 Introduction	22
2.2 Background.....	26
2.2.1 Previous Spatial Analysis of Volcanic Fields.....	26
2.2.1.1 Analysis Approaches	27
2.2.1.2 Application of Spatial Analysis	28
2.2.2 Regional Studies... ..	30
2.2.2.1 Michoacán-Guanajuato Volcanic Field, Mexico	30
2.2.2.2 Auckland Volcanic Field, New Zealand.....	31
2.2.2.3 Springerville Volcanic Field, Southwest United States.....	32
2.2.2.4 Cascade Volcanic Arc, Western United States.....	33
2.3 Methods.....	35
2.3.1 Data Compilation	35
2.3.2 Voronoi Analysis	36

Chapter	Page
2.3.2.1 Generating Voronoi Tessellations and Bounding Boxes	37
2.3.2.2 Simulating Random Data	37
2.3.2.3 Constructing Areal Distribution and Density Functions.....	39
2.3.2.4 Deriving an Intrinsic Length Scale from the Intersection of Density Functions	41
2.3.3 Kernel Density Estimation.....	43
2.4 Results.....	44
2.4.1. Individual Field Results	45
2.4.1.1 Auckland Volcanic Field (AVF).....	45
2.4.1.2 Springerville Volcanic Field (SVF).....	46
2.4.1.3 Central Cascades	47
2.4.1.4 Washington Cascades	48
2.4.2 Comparing Vent KDE Values	51
2.5 Discussion.....	53
2.5.1 Comparison with Previous Field Findings.....	53
2.5.2 Exploring Structures with Silverman and Voronoi.....	55
2.5.3 A Novel Clustering Length Scale	57
2.5.3.1 Using Area as a Measure of Departure	59
2.5.3.2 Avoiding Inferring an Underlying Distribution.....	60
2.5.4 Future Considerations	61
2.5.4.1 Understanding Length Scales and Artifacts.....	61
2.5.4.2 Additional Statistical Analysis.....	62

Chapter	Page
2.5.4.3 Limitations of Current Data	63
2.6 Conclusions.....	64
2.7 Acknowledgements.....	66
2.8 Data and Code Availability.....	66
2.9 Bridge.....	66
2.10 Supporting Information.....	68
 III. QUANTIFYING THE EFFECTS OF VOLCANO SNOW COVER ON INSAR COHERENCE USING A COMPUTATIONALLY INEXPENSIVE NEURAL NETWORK.....	
	71
3.1 Introduction.....	71
3.2 Geologic Setting.....	73
3.3 Methods.....	74
3.4 Results.....	77
3.5 Discussion.....	81
3.6 Conclusions.....	84
3.7 Acknowledgements.....	85
3.8 Data and Code Availability.....	85
3.9 Bridge	86
3.10 Supporting Information.....	87
 IV. INVESTIGATING SUBSIDENCE AT MEDICINE LAKE VOLCANO USING INSAR, GNSS, and MCMC MODELING.....	
	89
4.1 Introduction.....	89

Chapter	Page
4.2 Geologic Setting.....	92
4.2.1 Edifice Deformation.....	94
4.3 Methods.....	96
4.3.1 Network Modification and Post Processing.....	96
4.4 Results.....	100
4.4.1 Velocity Data	100
4.4.2 MCMC Model Setup	102
4.4.3 MCMC Model Results.....	103
4.5 Discussion.....	107
4.5.1 Effect of Loading	107
4.5.2 Comparing Model Residuals.....	110
4.6 Conclusions.....	110
4.7 Acknowledgements.....	112
4.8 Data and Code Availability.....	112
4.9 Supporting Information.....	113
V. CONCLUSIONS AND FUTURE DIRECTIONS.....	120
REFERENCES CITED.....	126

LIST OF FIGURES

Figure	Page
2.1. Global distribution of volcanic fields	25
2.2. Examples of analysis approaches to characterizing volcanic fields.	29
2.3. Vent locations	34
2.4. Simple Voronoi tessellation generation	39
2.5. Areal CDFs for observed and simulated data for six study regions	40
2.6. Areal PDFs for observed and simulated data for six study regions.....	42
2.7. AVF Voronoi tessellation with convex hull boundary	46
2.8. SVF Voronoi tessellation with convex hull boundary	47
2.9. Voronoi tessellation for Central Cascades	48
2.10. Voronoi tessellation for Washington Cascades	50
2.11. CDF plots for normalized density values.....	52
2.12. Map of AVF with vents that erupted in spatial and temporal proximity	56
2.13. CDF plots for normalized density values.....	58
2.14. Simulated vent locations	59
2.15. Three PDFs for simulated normally distributed scattered vents.....	63
2.S1. Voronoi diagrams for Springerville Volcanic Field colored by residuals.....	68
2.S2. Mean center (large blue/orange circle), standard distance (red).....	69
2.S3. Plots showing the expected value, observed value.....	70
3.1. Optical image with natural band color band combination	77
3.2. Time series spanning 2014-2020 showing the percent of pixels covered	79
3.3. Snow cover masks paired with corresponding InSAR coherence maps.....	80

Figure	Page
3.4. Maps of deformation from a Mogi point source at 10 km depth	84
3.S1. Perpendicular baseline plot for Sentinel-1 Track 115 acquisition dates.....	87
3.S2. Loss as a function of node amount for the hidden layer.....	87
3.S3. Confusion matrix for test dataset snow prediction accuracy	88
3.S4. NDSI values compared with snow prediction values for each pixel	88
4.1. Map of region surrounding Medicine Lake	92
4.2. Topographic map of region surrounding Medicine Lake	95
4.3. Perpendicular baseline plots	98
4.4. Timeseries data	99
4.5. Vertical velocity map over Medicine Lake.....	101
4.6. Distribution of depths, volume loss, center latitude, center longitude.....	104
4.7. Distribution of depths, strike, center latitude, center longitude.....	105
4.8. Distribution of depths, strike, center latitude, center longitude.....	106
4.9. Zoomed in topographic map of region surrounding Medicine Lake	109
4.10. Maps of residuals for each best fitting source	111
4.S1. InSAR ascending and descending line of sight velocity maps.....	113
4.S2. InSAR ascending and descending timeseries	114
4.S3. Histogram plots showing distribution of accepted guess values for point	115
4.S4. Histogram plots showing distribution of accepted guess values for sill.....	116
4.S5. Likelihood plot for each of the five chains in the MCMC sill scenario 1	117
4.S6. Histogram plots showing distribution of accepted guess values for sill.....	118
4.S7. Likelihood plot for each of the five chains in the MCMC sill scenario 2	119

LIST OF TABLES

Table	Page
Table 2.1. Summary of Field Distances/Statistics	45
Table 2.S1. Table listing calculated R-values for Poisson Nearest Neighbor (PNN)..	70
Table 4.1. Upper and lower bounds for each variable parameter	103

CHAPTER I

INTRODUCTION

Very well. So the universe is not quite as you thought it was. You'd better rearrange your beliefs then. Because you certainly can't rearrange the universe.

Isaac Asimov, Nightfall

1.1 Background

What do maps tell us about the processes affecting these volcanoes at and beneath the surface? How can we utilize different tools and techniques to map different volcanic systems? Why do we use maps to study volcanic hazards? These questions frame the work of this dissertation, which maps a variety of volcanic systems with a suite of tools to understand their formation and evolution through time. Understanding these aspects of volcanoes can help us address their local hazards and can allow us to compare different volcanic systems to uncover why they behave differently. Before we reach this why however, we will start with what we map at volcanic systems and different ways how to map them depending on their structure and behavior.

1.1.1 What to Map at Volcanic Systems

Distributed volcanism refers to volcanic systems whose eruptions are constrained neither in time nor space, and commonly manifest as volcanic fields that consist of tens to hundreds of short lived vents contained within an area. Eruptions in volcanic fields typically lead to new vent formation, and different eruptions can occur years to thousands of years apart and be within hundreds to thousands of meters apart depending on the size of the field. Typically, compositions of erupted products are basaltic (SiO_2 ~45-52%) and the prevalent type of vent found in these fields are monogenetic cinder cones formed from solidified basaltic lava (Valentine et al., 2021; Condit et al., 1996; Hasenaka & Carmichael, 1985). However, not every cinder cone is

monogenetic, and other eruptive products with a wider range of compositions also can exist in these fields such as shields, lava flows, maars, domes, and tuffs (Hasenaka, 1994; Hopkins et al., 2020). Volcanic fields can occur in a variety of tectonic settings including extensional (e.g. Springerville, San Francisco, and Portillo fields in the southwestern U.S.), strike slip (e.g. Pinacate (Mexico), Armenia (Armenia), Es Safa (Syria) fields), and compressional environments (Abu field, Japan) (LeCorvec et al., 2013). Subduction zones can also host widespread distributed volcanism, such as at the Michoacán-Guanajuato Volcanic Field (MGVF) in central Mexico that has ~1000 vents and sits 200-440 km from the Middle America Trench (Hasenaka & Carmichael, 1985). The Cascade Volcanic Arc also contains hundreds of cinder cones, shields, and domes in addition to its larger composite centers (O'Hara et al., 2020).

Focused volcanism refers to volcanic systems that have the location of eruption constrained in space; typically this manifests as large shield and composite volcanoes with long eruptive histories. Since the location of eruption is constrained, focused volcanism is also associated with magma storage and evolution over time, leading to eruptive products with a wide range of compositions and behaviors (lava flows, lahars, pyroclastic density currents, eruption columns, etc.). These large shields and composite volcanoes are found in 1) continental or island arcs that are the result of subduction zone tectonics or 2) volcanic centers or chains produced from mantle hot spots. An example of the former is the aforementioned Cascade Volcanic Arc formed from the subduction of the Juan de Fuca oceanic plate beneath the continental North American plate (Hildreth, 2007). Additional examples of subduction zone volcanic arcs include the Central American Volcanic Arc, the Aleutian island arc, and the Andes, while hot spot volcanism includes the Hawaiian island volcanic chain, the Canary Islands, and Iceland (Sleep, N.H., 1992).

1.1.2 How to Map Volcanic Systems

Early mapping techniques that are still used to provide critical data on volcanoes involve field work where different characteristics of volcanoes (slope, height, width, etc.) are measured and samples from the region are collected. The physical traits of the volcanoes can be used to classify them into different groups (Hasenaka, 1994) while the samples are processed to find additional properties such as melt storage depths, eruption ages, and magma compositions (Condit & Connor, 1996; Deligne et al., 2016; Bacon & Lanphere, 2006). Results of this field work are often maps of volcanoes with different key features identified such as eruptive units, faults, and topographic changes. Additional field techniques that provide observations of the subsurface are seismic arrays (e.g. Evans & Zucca, 1988; Heath et al., 2019; Waite & Moran, 2009) and gravity surveys (Poland et al., 2018; Williams et al., 1987; Deng et al., 2017). While the work of this dissertation focuses on methods that either analyze field data already collected or collect data remotely, field mapping methods remain a vital part of analyzing a variety of volcanic systems.

Spatial analysis of volcanic systems uses different statistical techniques to understand processes such as clustering, alignment, and density of vents within distributed volcanic fields. Early spatial analysis included comparing cinder cone volume with lava flow volume to find explosivity and viscosity of magmas (Hasenaka & Carmichael, 1985), and measuring small vent (cinder cone) and medium vent (shield) distance from subduction zone trench to understand magma availability (Hasenaka, 1994). Distribution of distances between vents can be used for the various nearest neighbor (NN) methods-Poisson Nearest Neighbor (PNN), normalized PNN, logistic NN, and “scavenged PNN”-to understand if vents are clustered, which indicates different processes such as crustal storage or faulting impacting vent location (Clark & Evans, 1954; Baloga et al., 2007; LeCorvec 2013). Alignments of field vents can be identified using the two-point azimuth (Lutz, 1986), Hough transform (Wadge & Cross, 1988) and strip-filter (Zhang & Lutz,

1989) methods to determine if linear chains of vents are due to tectonic control or are the result of fissure eruptions (LeCorvec et al., 2013). Clusters of vents in volcanic fields can also be identified using k-means and hierarchical approaches to separate different groups potentially impacted by different storage bodies and/or fault systems (e.g. Connor & Hill, 1995; Connor, 1990). Kernel Density Estimation is a method that visualizes the density of vents in volcanic fields to indicate areas of increased and decreased volcanism across the regions (e.g. Lutz & Gutmann, 1995; Connor, 2000; Bebbington, 2015).

In the last half century, remote sensing methods have emerged as a primary way to map volcanic systems and their hazards. Generally remote sensing refers to measuring characteristics of the earth using space-borne or air-borne satellites. For remote sensing of volcanoes, there are numerous methods that can be decently summarized into four volcanic properties they map: thermal emissions, gas emissions, ash clouds, and surface change (Pritchard et al., 2020). Thermal satellites utilize Thermal Infrared (TIR), Short Wave Infrared (SWIR), and Mid Infrared (MIR) wavelengths to observe thermal anomalies such as volcanic hot spots, lava flows, and fumaroles (Flynn et al., 2000; Harris, 2013). For detecting gas emissions, satellites typically utilize wavelengths in the ultraviolet (UV) region in addition to MIR and TIR (Carn et al., 2016). Volcanic ash clouds are often tracked with geostationary meteorological satellites (Prata, 2009). Multi-spectral optical satellites that use visible and infrared wavelengths, as well as Synthetic Aperture Radar (SAR) satellites that use microwave sensing, are used to track surface changes at volcanoes such as lava flows, dome growth, ashfall, pyroclastic flows, and deformation (Wadge et al., 2012; Pallister et al., 2019; Poland et al., 2014). GNSS satellites continuously track three-dimensional deformation (ground movement) at a single point in space, and Interferometric Synthetic Aperture Radar (InSAR) differences two SAR images taken at different times to produce maps with wide

spatial coverage of deformation that can be projected into vertical and east-west directions (GNSS reference; Massonnet et al., 1995; Zebker et al., 2000; Hooper et al., 2012).

1.1.3 Why Map Volcanic Systems

The reasons behind mapping volcanoes are as numerous as volcanoes themselves, but they all fall under the purpose of trying to better understand volcanic hazards and improve mitigation efforts for these hazards. This motivation is clear for remote sensing data, which is often used to map volcanic centers before, during and after eruptions. Deformation data from InSAR can track magma movement beneath the surface to provide better constraints on where within a volcanic system there could be an eruption. Weather satellites can track ash movement through the atmosphere to help pilots navigate aircraft safely around eruption columns. Lava flows can be tracked using optical and radar data to determine future flow paths and evacuate residents and livestock.

Mapping volcanic systems can also constrain different processes affecting the systems to use the past evolution to determine potential future activity. This is particularly important at volcanic fields, where it is difficult to monitor the entire field; using statistical mapping to understand if there are subsurface tectonic or magmatic controls that can help constrain what processes might currently impact eruption location, duration, and style. Even for focused volcanic centers, mapping these systems can produce data that can be inverted to find magma chamber properties (size, shape, depth, etc.) which can inform future estimates of eruption size and style.

Another motivation behind mapping volcanoes is to understand which mapping techniques work on which volcanic systems and how to improve upon existing data. As stated previously, the large spatial extent and unconstrained eruption location at most volcanic fields makes monitoring them with remote sensing difficult, but statistical methods can be effective tools for summarizing

behavior across these wide areas and multitudes of vents. In contrast, statistical methods are difficult at focused centers, but monitoring over these systems can be performed. These methods aren't mutually exclusive however, particularly in regions like the Cascades where there is both distributed and focused volcanism. There are also challenges to the methods themselves. SAR data can be difficult to use in heavily vegetated, snow covered, or submerged areas, while UV gas sensing can occur only during the day, and thermal monitoring can be obscured by cloud cover. For statistical analysis, there are often decisions that have to be made with thresholding data, scale of study, and vent identification that all impact results. However, only by trying these mapping methods and learning their advantages and disadvantages across different volcanic systems can we adapt our maps to better illuminate the hazards associated with these systems.

1.2 Outline

This dissertation begins with Chapter II where we map distributed volcanism in a variety of environments; the Auckland Volcanic Field in Auckland, New Zealand, the Springerville Volcanic Field in Arizona, USA, and fields along Cascade Volcanic Arc segments in Oregon and Washington, USA. We map the area between vents for each field using a variety of statistical techniques to develop a methodology for determining if clustering exists in different fields and at what length scales. Understanding if clustering exists in volcanic fields is important for determining if processes such as faulting or magma storage will impact the next vent location. The work in this chapter is done in collaboration with Chris Harper, Katharine Cashman, and Leif Karlstrom, and is under review for publication in a USGS special issue.

Chapter III of this dissertation transitions to mapping a focused center, Mt. St. Helens, which is located in southwest Washington along the northern section of the Cascade Volcanic Arc. This chapter is focused on tracking seasonal snow cover across the Mt. St. Helens region to develop

a better understanding of how snow cover changes over time and how drastically snow cover impacts InSAR signal coherence. To do this, snow cover is mapped using image classification of Landsat 8 optical imagery by a computationally inexpensive neural network and then compared with coherence images from Sentinel-1 InSAR data. We are able to find which regions of Mt. St. Helens are consistently snow covered and how significantly that snow cover degrades coherence, which is useful for understanding how much deformation could be seen with InSAR in the case of a chamber inflation event. This work is done in collaboration with Josef Dufek, Christelle Wauthier, and Meredith Townsend, and will be submitted to JGR: Machine Learning.

In Chapter IV we focus on another volcanic system, Medicine Lake volcano, that resides in Northern California at the southern extent of the Cascade Volcanic Arc and on the western edge of the Basin and Range extensional province. Due to this intersection of tectonic regimes, Medicine Lake is a large, broad shield volcano peppered with monogenetic cones; this work focuses on Medicine Lake's central caldera and the steady subsidence signal that has been mapped across the caldera since 1954. We use Sentinel-1 InSAR as well as GNSS data to track present ground deformation, and then use a combination of models to describe processes potentially causing this deformation. This work is done in collaboration with Josef Dufek, Meredith Townsend, and Christelle Wauthier and will be submitted to JGR: Solid Earth.

Chapter V presents concluding remarks and thoughts on future directions in the field of mapping volcanic systems.

CHAPTER II

AN AREA-BASED METHODOLOGY FOR DERIVING INTRINSIC LENGTH SCALES OF DISTRIBUTED VOLCANIC FIELDS

From Bussard, R., Harper, C., Cashman, K. & Karlstrom, L. (2024). *An Area-Based Methodology for Deriving Intrinsic Length Scales of Distributed Volcanic Fields*. Manuscript submitted for publication. The writing of this chapter was done by me, Chris Harper, and Kathy Cashman with Leif Karlstrom providing editorial assistance. Chris Harper, Kathy Cashman, and I conceptualized the work presented in this chapter. Leif Karlstrom provided one of the datasets used for analysis. Chris Harper and I performed the analysis.

2.1 Introduction

Collections of volcanic vents known as distributed volcanic fields (Fig. 2.1) can be found in both intraplate and arc settings. The sheer number of volcanic vents, together with the infrequency of eruptive activity in most volcanic fields, means that the usual tools for studying the underlying magmatic system – petrology, geophysics, and physics-based modeling – are challenging to apply. For this reason, many studies of volcanic fields have focused on measuring and interpreting the spatial and, where available, the temporal distribution of individual vents/eruptive episodes. When compared with the overall footprint of the field and patterns of regional tectonics, vent distributions have been used to either (1) forecast the probable location of future activity (Connor & Hill, 1995; Conway et al., 1998; Germa et al., 2013; Bebbington, 2013)

or (2) infer characteristics of the field through time. Key characteristics include the geometry of the magma source region (Condit & Connor, 1996), the thickness of the underlying crust (Mazzarini 2004; Mazzarini et al., 2008; 2010), controls on magma movement (Le Corvec et al., 2013; Grosse et al., 2020; Morfulis et al., 2020; Valentine et al., 2021), magma storage locations (Pozzobon et al., 2015; Mazzarini et al., 2016; O’Hara et al., 2020), and post-emplacement erosion patterns (Rodriguez-Gonzales et al., 2011; O’Hara & Karlstrom, 2023). To find these characteristics, various statistical methods have been developed and applied. Each method, however, requires choices of parameters, data binning, and benchmark distributions, all of which affect both the results and their interpretation.

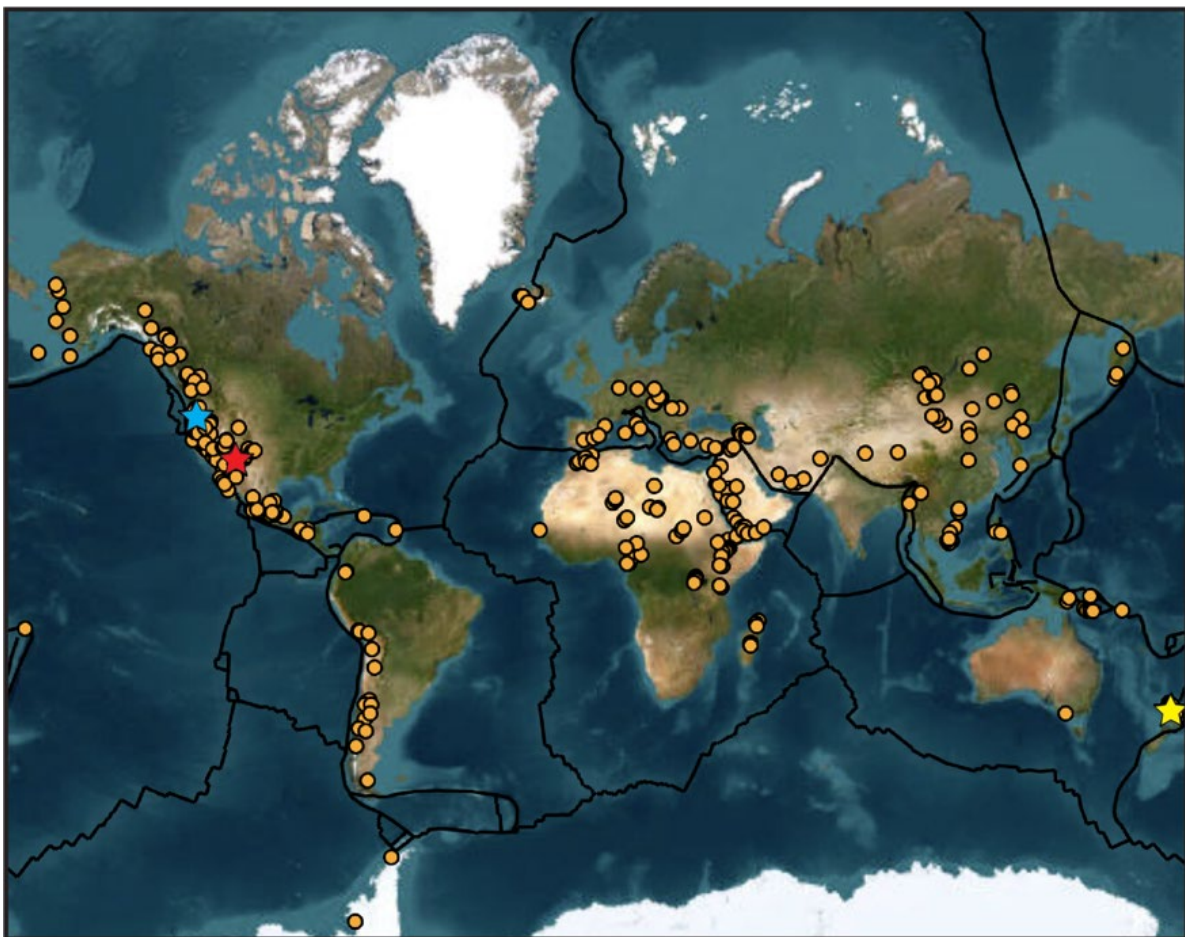


Figure 2.1. Global distribution of volcanic fields active in the Pleistocene and Holocene [GVP]. Stars represent the fields analyzed in this study (yellow = Auckland Volcanic Field; red = Springerville Volcanic Field; blue = Cascades Volcanic Arc).

In this work, we seek to answer the following specific question: Is there a length scale intrinsic to each volcanic field that signifies the initiation of non-random behavior (i.e. clustering of vents in space)? To answer this question, we use the areal distribution of vents instead of the more commonly used linear distance to compare with the distribution expected from a random process. The result is an area, which can then be converted to a length scale, that represents the length at which behavior departs from random. We perform this analysis on multiple volcanic fields in a variety of tectonic settings and with different magmatic histories and visualize our results with maps of vent density. We discuss the differences between our methodology and examples of current methods, then compare vents characterized by our length scale with distance and area metrics from full field data and simulated vent data. We then explore the relation between vent age and spatial density from the Kernel Density Estimations produced by our workflow to connect the spatial structure of these fields with emplacement sequence to begin exploring causes of clustering in these fields.

2.2 Background

2.2.1 Previous Spatial Analysis of Volcanic Fields

Numerous techniques of spatial analysis have been used to assess the distribution of individual vents (typically scoria cones) within volcanic fields (e.g., Connor, 1990; Connor et al., 1992; Lutz and Gutman, 1995; Conway et al., 1998; Le Corvec et al., 2013; Traglia et al., 2014; Mazzarini et al., 2010; 2016; Deng et al., 2017; Grosse et al., 2020; Morfulis et al., 2020). Spatial analysis techniques can be divided into two broad categories: analyses designed to assess (1) the structure of volcanic fields for comparison with associated tectonic structures/stress fields and (2) patterns of vent locations, which can provide information about the underlying magmatic system and, under some circumstances, be used to anticipate future vent locations. Here we briefly review

both analysis types and their application to questions about volcanic field formation, evolution and patterns of eruption.

2.2.1.1 Analysis Approaches

The simplest structural analysis measures the overall shape of the volcanic field, which is often inferred to mirror the mantle source. Volcanic field shapes are commonly measured by fitting a minimum area ellipse to a convex hull formed by connecting perimeter vents (Fig. 2.2a). The overall field shapes can be compared with vent alignments and other stress indicators, such as the spatial distribution of faults, geophysical structures and/or stress maps. User-defined criteria for identifying alignments include the minimum number of features (typically taken as three), tolerances set for mis-alignment ('length'; Fig. 2.2b inset) and the distance over which alignments are accepted. An empirical estimate for the latter (Le Corvec et al., 2013a) infers a maximum correlation distance that is inversely proportional to the mean vent density (Fig. 2.2b). Also important is the timing of the alignment: vents aligned along a fissure during a single eruption may record dike propagation (typically in the direction of maximum principal stress), whereas repeated eruptions along a structural lineament can reflect strong control of pre-existing faults (Gómez-Vasconcelos et al., 2020).

Several approaches have been used to determine the spatial distribution of vents within volcanic fields. The first is Poisson Nearest Neighbor analysis (PNN), which compares the mean distances between nearest neighbor vents to those of an idealized statistical model (e.g., a Poisson distribution). Here the area analyzed is defined either by the convex hull fit to the overall field (Fig. 2.2a) or by adding a buffer to the convex hull determined by the mean nearest neighbor distance (Le Corvec et al., 2013b). The ratio (R) of the observed distribution (R_o) to the distribution expected (R_e) is used to define the overall vent distribution, with $R < 1$ showing regions where

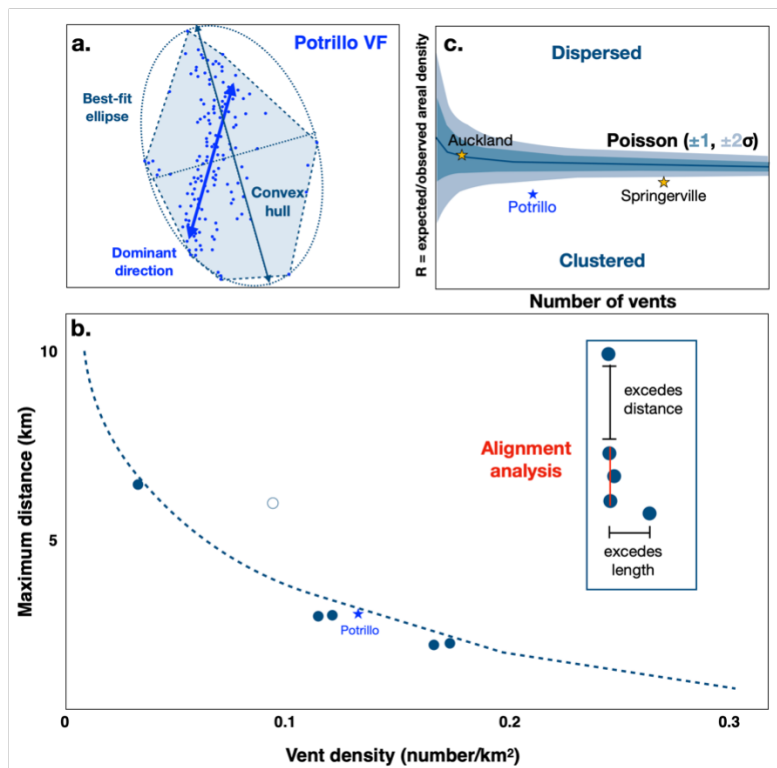
vents are more clustered than expected and $R > 1$ denoting fields where the vents are more distributed than expected (Fig. 2.2c). In their analysis of 37 volcanic fields, Le Corvec et al. (2013a) find that most (28) have clustered vents. A more visual measurement of vent distribution is cluster analysis. A simple approach to cluster analysis uses a k-means algorithm; this approach has the disadvantage, however, of requiring the user to specify, a priori, the number of clusters. The same problem arises with a hierarchical approach to cluster analysis (Connor & Hill, 1995). Kernel Density Estimation (KDE) is a commonly employed technique that estimates the probability density of vents using a smoothing filter (the kernel), which is typically an isotropic Gaussian kernel, although anisotropic Gaussian kernels can also be applied to find alignments and structures (Bebbington, 2015; Connor et al., 2019; Kiyosugi et al., 2012). The primary challenge to KDE is determining the bandwidth over which smoothing occurs; similar to other types of cluster analysis, the results are non-unique (Canon-Tapia, 2020). Here, we develop a methodology to determine an empirical clustering length scale for a given volcanic field that provides functionality as a bandwidth for KDE and allows for comparison among fields of different sizes and shapes.

2.2.1.2 Application of Spatial Analysis

In general, studies of vent distributions distinguish between fields with relatively high (10-100 km³/Myr) and low (< 1 km³/Myr) rates of magma supply (Valentine & Perry, 2007). Where magma supply rates are high, vents are clustered and radially oriented around centers, attesting to magmatic control on patterns of eruptive activity (Karlstrom et al., 2015). Where magma supply rates are low, vents often align with surface structures, providing evidence of tectonic control (Bacon, 1982). Importantly, analysis of vent locations in mafic volcanic fields is usually confined to scoria cones. In arc environments, however, the volumetric contribution of magma output

related to scoria cone eruptions is commonly substantially less than that recorded by associated shield volcanoes (Hasenaka and Carmichael, 1985; Hasenaka, 1994; O’Hara et al., 2020). Moreover, a recent study suggests that large ($\sim 10 \text{ km}^3$) shield volcanoes can form rapidly (in decades to a few centuries; Pivarunas et al., 2022) and therefore pose hazards that are similar in time, as well as space, to those posed by cinder cone eruptions. The conditions that favor shield building over more focused composite centers, on the one hand, and distributed cinder cones, on the other, are not well understood. Other complicating factors include multiple vents formed during a single eruptive episode (the “vents to event” problem; Condit and Connor, 1996; Runge et al., 2014; Gallant et al., 2021) and coverage of older vents by the products of younger eruptions (“hidden vents”; Runge et al., 2014).

Figure 2.2. Examples of analysis approaches to characterizing volcanic fields. (a) Overall field shape [Potrillo, NM], showing vents, convex hull enclosing vents, best-fit ellipse to convex hull, and apparent dominant direction of vents. (b) Vent alignment analysis, illustrating user-assigned parameters of length and distance (inset) and empirical estimate of distance parameter from highlighted points. (c) Example of Poisson nearest neighbor analysis, showing fields for Poisson vent distribution (including both 1σ and 2σ limits) as well as fields where vents are either more clustered or more distributed than a Poisson model. For illustration, plotting positions of Potrillo, NM (see (a)), Auckland, NZ, and Springerville, NM. All figures redrafted and modified from Le Corvec et al. (2013a).



Spatial analysis has also been used to constrain the nature of the underlying volcanic system, for example, using the apparent relation between self-similar vent spacing (Mazzarini et al., 2003) and either crustal thickness (Mazzarini et al., 2010) or depth to crustal magma reservoirs

(Mazzarini et al., 2016). Addition of both compositional analyses and age data can be used to track the magmatic evolution of volcanic fields (Brenna et al., 2012; Stelten et al., 2018). When combined with both volume measurements and geophysical datasets, vent analysis can provide important information about magma supply and transport (O'Hara et al., 2020).

Finally, spatial analysis has been used to provide likelihood estimates of future vent locations. Here assumptions relate to the inferred spatial stationarity of the magma source through time. Optimally, spatial and temporal data are used together, such that vents are clustered by both location and age (Condit and Connor, 1996; Gallant et al., 2021). Analysis of temporal recurrence rates, however, requires detailed analysis of vent/eruption ages, which is challenging for fields with hundreds of individual vents. Geomorphic measurements of scoria cone degradation provide potential age constraints, although they must be corrected for climatic variation (Fornaciai et al., 2012; Jaimes-Viera et al., 2018; Grosse et al., 2020; O'Hara and Karlstrom, 2023). A spatio-temporal analysis of the Springerville volcanic field, moreover, found a poor correlation between locations with high recurrence rates and sites of future eruptions (Condit & Connor, 1996).

2.2.2 Regional Studies

Here we provide a brief overview of a detailed study of a mafic distributed volcanic field (the Michoacán-Guanajuato Volcanic Field Mexico) followed by summaries of the volcanic fields that we analyze (Fig. 2.3).

2.2.2.1 Michoacán-Guanajuato Volcanic Field, Mexico

One comprehensive regional study of a large distributed volcanic field is Hasenaka and Carmichael's (1985) analysis of the Michoacán-Guanajuato Volcanic Field (MGVF) in central Mexico. This study used topographic maps to analyze morphometric parameters of cinder cones and their associated lava flows. Important observations include a 1:10 relation between the

volumes of individual cones and related lava flows and the degradation of both cones and flow surfaces with time. Analysis of eruption ages further showed that the youngest vents occur only in the southern part of the field, consistent with recent evidence for trenchward migration of the volcanic arc because of slab rollback (Ferrari et al., 2012). An associated study of shield volcanoes (Hasenaka, 1994) showed that they represent almost twice the dense rock equivalent (DRE) volume of the cinder cones; adding these data thus greatly extends estimates of the magma production rate of this volcanic field (0.7 km³/1000 yr for the past 1Ma; 1.2 km³/1000 yr for 0.04 Ma-present). Subsequent studies of the MGVF have examined the tectonic origin of vent alignments in parts of the field (Wadge and Cross, 1988; Cebriá et al., 2011; Gómez-Vasconcelos et al., 2020) and have used the Hasenaka and Carmichael database to test methods of cluster analysis (Connor, 1990; Mazzarini et al., 2010; Canón-Tapia, 2020), semi-automated identification of volcanic edifices (Di Traglia et al., 2014) and application of fractal analysis to crustal thickness determinations (Mazzarini et al., 2010). From a volcanic hazards perspective, it is important to note the repeated recent magma intrusions into the upper crust (six seismic swarms since 1997, with the most recent in 2021; Legrand et al., 2023) in close proximity to the youngest cinder cone, Parícutin, which last erupted in 1943-1952 (Luhr and Simkin, 1993). This activity raises questions about both conditions of pre-eruptive magma storage and possible triggers for future eruptive activity.

2.2.2.2 Auckland Volcanic Field, New Zealand

The Auckland Volcanic Field (AVF; Fig. 2.3a) is arguably the most intensely studied volcanic field globally, because of its clear threat to New Zealand's largest city (population > 1.6 million; Hopkins et al., 2020). In contrast to the >1000 cinder cones in the MGVF, the AVF hosts only 53 vents. The most recent eruption was ~500 years ago at Rangitoto, a shield volcano that is

also the only location of vent reoccupation. The volume of Rangitoto accounts for almost 50% of the total erupted volume of the field (Hopkins et al., 2020). Hydrovolcanism also played a key role in eruptions within the AVF, with 83% of the identified eruptions initiating with phreatomagmatic activity (Kereszturi et al., 2014). In contrast to the vent clustering observed in many volcanic fields, Poisson Nearest Neighbor analysis of vents in the AVF produces results that are indistinguishable from a Poisson distribution, that is, the vents are randomly distributed in space (Le Corvec et al., 2013a). Age constraints on most vents provide important underpinning for probabilistic forecasting models. Statistical analysis of spatio-temporal data shows that within the AVF, there is no consistent pattern to vent location in time (Molloy et al., 2009; Bebbington and Cronin, 2011; Le Corvec et al., 2013a) although there is evidence for strong structural control on vent locations (Cassidy & Locke, 2010; Bebbington & Cronin, 2011) and some evidence that larger eruptive volumes may fill gaps in vent distributions (Bebbington, 2015). Geochemical studies show little evidence of crustal magma storage, but instead argue for small melt batches from a heterogeneous mantle that ascend rapidly to the surface (Brenna et al., 2018; Rowe et al., 2020). Taken together, studies of the AVF suggest that volcanism in this small volume field is likely controlled by conditions of mantle melting, with magma ascent from the mantle strongly influenced by crustal tectonics.

2.2.2.3 Springerville Volcanic Field, Southwest United States

A recent review of volcanic fields in the southwest US provides an overview of the petrology, geochronology, landforms and eruption recurrence rates for 37 recognized Quaternary volcanic fields, with detailed maps of vent locations for the 8 major fields (with >100 vents each). In planform shape, these fields range from highly elongate (e.g., Lunar Crater, NV; Portrillo, NM) to more equant (e.g., Springerville and San Francisco, AZ); some strong vent alignments document

fault control (e.g., Uinkaret, AZ). Vent distributions have been most extensively studied for Springerville (Fig. 2.3b), where detailed mapping (Condit et al., 1992; Condit & Connor, 1996; Mnich & Condit, 2018) provides both compositional and temporal constraints on the evolution of this large (409 vents) Quaternary field. A spatio-temporal analysis of vent distribution shows extensive clustering and rates of localized magmatism that have waxed and waned through time; interestingly evolved magmas occur only in locations of frequent activity. Comparison with gravity measurements shows a correlation between high spatial vent density and regions of inferred high magma flux (Deng et al., 2017). A similar analysis of the elongate Zuni-Bandera field shows it to be aligned with a steep gravity gradient caused by an abrupt change in crustal density, suggesting crustal controls on magma pathways to the surface. More broadly, mantle melting driving volcanism on the Colorado plateau is likely controlled by edge-driven convection (Reid et al., 2012).

2.2.2.4 Cascade Volcanic Arc, Western United States

The distribution of volcanic vents along the US portion of the Cascade arc has been compiled for the Quaternary by Guffanti and Weaver (1988), Hildreth (2007), Ramsey & Siebert (2017), and O'Hara et al. (2020). These compilations include not only cinder cones and mafic shields, but also domes and stratovolcanoes. Not surprisingly, composite volcanoes and large shield volcanoes (such as Newberry, OR) account for much of the erupted volume, while cinder cones comprise the largest number of vents (O'Hara & Karlstrom, 2020). Although most Quaternary vents are strongly aligned N-S, parallel to the offshore subduction zone, there is substantial 'smearing' of vents to the west in the vicinity of Portland OR, and to the east in regions of back arc volcanism in central Oregon (associated with Newberry volcano) and northern California (associated with Medicine Lake volcano and volcanic fields east of Lassen volcano).

Analysis of magma composition, volume and heat flux demonstrates the role of mantle-derived basalt in modulating along-arc patterns of volcanism (Till et al., 2019). A spatio-temporal comparison of the normalized spatial density of vents and the edifice volumes (both measured in along-arc bins of 0.5° latitude and across-arc bins of 0.5° longitude) shows strong clustering of distributed vents in central Oregon and northern California, particularly since the mid-Pleistocene. These clusters align with anomalies in heat flow, seismic tomography, gravity, and interseismic upper plate deformation (O'Hara et al., 2020). In large part, this pattern illustrates the influence of back-arc volcanism, centered particularly around Newberry and Medicine Lake volcanoes. Erosion rates of Cascade volcanoes mirror eruptive patterns, with E-W asymmetry associated with long-lived orographic precipitation gradients (O'Hara & Karlstrom, 2023).

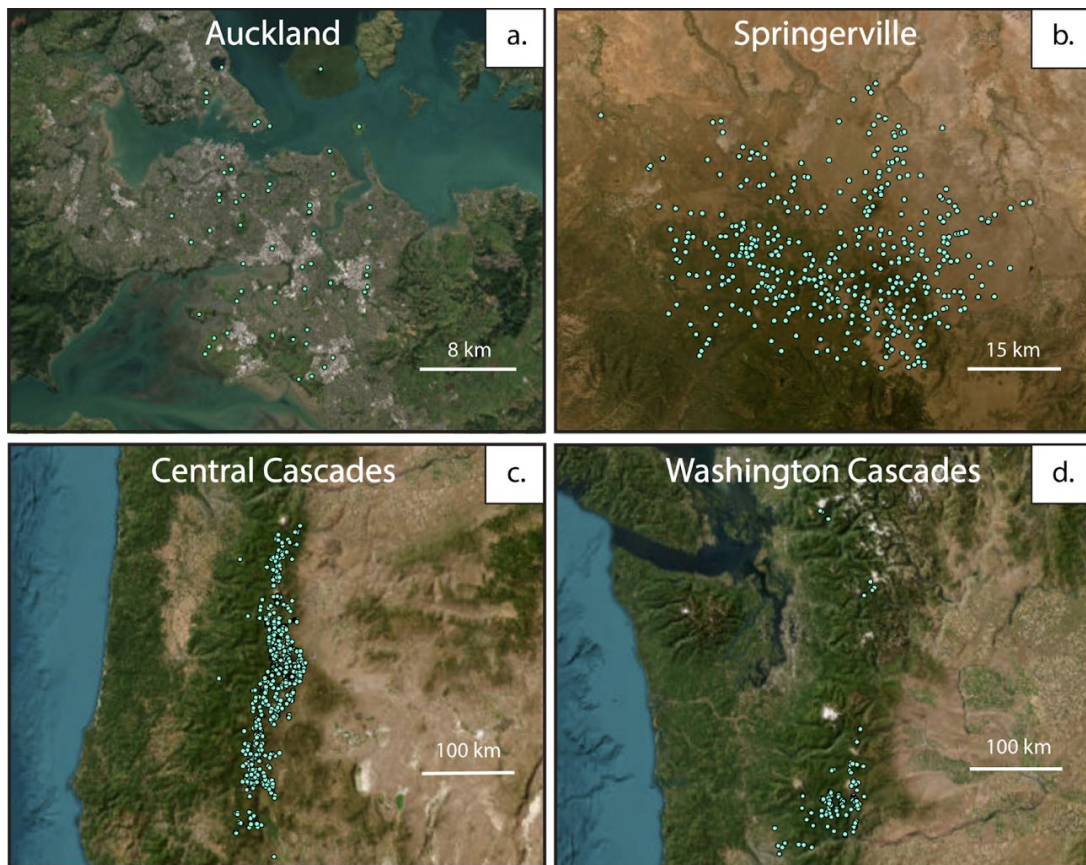


Figure 2.3. Vent locations across the (a) Auckland Volcanic Field (53 vents), (b) Springerville Volcanic Field (409 vents), (c) Central segment of the Cascades (588 cinder cone vents and 92 shield vents), and (d) Washington segment of the Cascades (88 cinder cone vents and 39 shield vents) used for Voronoi analysis and Kernel Density Estimation.

2.3 Methods

2.3.1 Data Compilation

We obtained vent location data for the Auckland and Springerville volcanic fields as well as the Cascade volcanic arc from previous studies that each dealt differently with the challenge of defining vents. Fifty three discrete vents have been mapped in the Auckland Volcanic Field (AVF) using both traditional field methods and more recently, by remote sensing techniques such as Light Detection and Ranging (LiDAR) (Fig. 2.3a; Hayward & Hopkins, 2019; Hopkins, 2020). To remain consistent with the current definition of the vents in the AVF, we marked the location of the Rangitoto shield volcano with a single data point corresponding to a single vent location, while recognizing that, atypically, it has been the site of more than one eruption. The Springerville volcanic field (SVF), in contrast, has been mapped as 409 eruptive units with distinct locations (Fig. 2.3b; Condit & Connor, 1996); as single cones (vents) have been identified for most eruptive units, we assign each unit a ‘vent’ point, such that each point corresponds to an eruption. Vent location data for the Quaternary Cascades has been compiled by Ramsey & Siebert (2017) to identify 2836 vents, which include cinder cones, domes, shields, and composite centers. We analyzed only the cinder cone and shield data over latitudes from just south of Mt. Hood to the California state border (designated the Central Cascades segment, although we note that various arc segmentations have been proposed, e.g., Schmidt et al., 2008). We chose to start south of Mt. Hood to closer replicate the Oregon segment as defined in Hildreth (2007); we also omitted cinder cones and shields associated with Newberry volcano. The resulting catalog includes 588 cinder cones and 92 shield volcanoes (Fig. 2.3c). We then defined a Washington Cascades segment where we use cinder cones and shields north of the Washington-Oregon state border but omitted the older and off-axis Simcoe volcanic field. This produced a Washington segment that includes 88 cinder

cones and 39 shield volcanoes (Fig. 2.3d). Note that pre-Quaternary vents are not included in the Cascades dataset.

For each region of interest, we also compiled available supporting data. For example, 51 of the 53 vents in the AVF have been dated, and type(s) of eruption at each vent (phreatic, phreatomagmatic, and dry magmatic) recorded (Hayward & Hopkins, 2019; Hopkins, 2017). Age data from both radiometric dating and stratigraphic analysis are also available for the SVF, with compositional data for 260 of the 418 vents (409 distinct location vents with additional 9 vents of associated erupted units). The Cascade dataset includes broad age and compositional classification in addition to edifice volumes for most vents (O'Hara et al., 2020; O'Hara & Karlstrom, 2023).

2.3.2 Voronoi Analysis

Approaches to spatial statistics used to identify physically relevant features within volcanic fields compare the observed features with random behavior (Le Corvec et al., 2013; Mazzarini et al., 2003; Condit & Connor, 1996; Connor, 1990). We call such features structures, with common examples including clustering, periodicity, and dispersion. Structures are tied to how we define random, most commonly generated from a Poisson point process and using the distributions of distances between points as a measure of comparison. Vent locations are, however, two-dimensional, and for this reason we used the two dimensional measure, area. This approach allows us to compare area- and distance-based metrics to explore the structures.

We describe the areas of the points' distribution using Voronoi tessellations, which create a unique polygonal partition of the vents. Here each point is represented by a polygon that has an area that can be used to extract an intrinsic length scale from the vent location data. We use four steps; the first two steps are inspired from the methodology by Bray et al. (2014): (1) generate a Voronoi tessellation and bounding box, (2) simulate random data and calculate residuals, (3)

construct areal distribution functions from both observed and simulated data and (4) use the intersection point between these two function as an intrinsic length scale for clustering.

2.3.2.1 Generating Voronoi Tessellations and Bounding Boxes

The simplest construction of a Voronoi diagram is built from the successive intersection of half-planes formed between one point and each other point in a dataset. A more computationally efficient (albeit less intuitive) construction comes from a Delaunay Triangulation of the vent location data. The Delaunay triangulation maximizes the minimum of all the angles of the triangles and produces a boundary that serves as a convex hull for our set of points. With this triangulation (implemented in our work through the `DelaunayTriangulation` package in Julia), we construct the convex hull that will serve as the bounding box for analysis. While there are other methods to construct bounding boxes (e.g., a rectangular bounding box), we tested both geometries and found no discernable differences in the resulting area distributions (Fig. 2.S1). We chose to use the convex hull because it is constructed only from the location data, reducing the potential to introduce bias by involving additional area around the field. Although there are instances where a convex hull boundary at a specific time in the history of a volcanic field does not encapsulate the future footprint of the field, the convex hull provides an unbiased approximation of volcanic field boundaries that allow us to explore spatial structures in vent distributions. Each triangle from the constructed Delaunay Triangulation uniquely defines a circumscribed circle; a Voronoi diagram is constructed by connecting the centers of each circle (Fig. 2.4).

2.3.2.2 Simulating Random Data

We use this Voronoi diagram as an adaptive mesh over which we randomly scatter points contained within the boundary of the convex hull. We simulate five-thousand instances of randomly scattered vents. In each iteration, we (1) generate the number of vents to be scattered, k ,

from a homogeneous Poisson distribution and (2) randomly scatter these k points over the Voronoi diagram mesh with the convex hull boundary. We choose the Poisson distribution for our random generating process because it maximizes entropy (assumes the least information) over the natural numbers:

$$p(k) = \frac{\lambda^k e^{-\lambda}}{k!} \quad (1)$$

Equation 1 shows that the probability of generating k vents is controlled by λ . For Poisson processes playing out through time λ represents the expected rate at which events will occur; for spatial processes it represents the density of expected events. We estimate λ by calculating the vent density within the bounding box (convex hull). For a field of N vents contained within a convex hull of area A , this yields the estimated density parameter $\hat{\lambda} = N/A$. Once our k vents are generated from our estimated density parameter, we scatter them randomly over the convex hull by leveraging the Delaunay triangulation and properties of Poisson and uniform distributions. A Poisson process conditioned over a constant number of points and a bounded area becomes uniformly distributed. A point can be uniformly distributed over the triangle in three steps.

1. Let A , B , and C be vectors which define the three sides of a triangle. Without loss of generality, we can construct a parallelogram by reflecting the triangle over the midpoint of side C .
2. Let u_1, u_2 be two random numbers generated from the uniform distribution on the closed interval from zero to one ($U(0,1)$). Then the linear combination of $u_1 \cdot A + u_2 \cdot B$ yields a random point in the parallelogram.
3. If $u_1 + u_2 > 1$ then the point falls outside of the original triangle. However, reflecting across C places the point back in the original triangle. Since the complement of the uniform distribution is also a uniform distribution, we can randomly scatter a point within our

original triangle by adding the constraint that if $u_1 + u_2 > 1$ we instead take the linear combination of $v_1 \cdot A + v_2 \cdot B$ which are equal to $1 - u_1$ and $1 - u_2$ respectively.

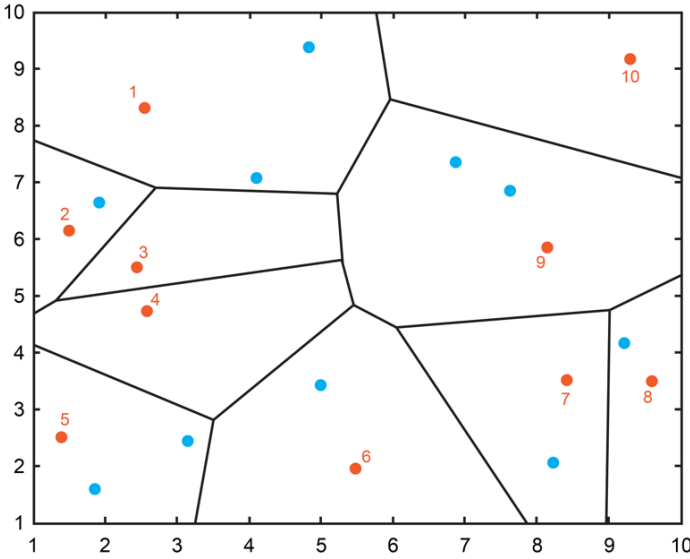


Figure 2.4. Simple Voronoi tessellation generation with ten cells contained within a rectangular bounding box. Observed locations are the orange numbered points while simulated locations are the blue points.

Now each point can be randomly scattered over the hull by first randomly selecting a triangle weighted by its area and then randomly placing the point within that triangle. The null hypothesis is that the observed vent location data was created from a Poisson process with the same intensity, thus by construction the expected number of points in each Voronoi cell of the mesh is one, and the residual becomes one subtracted by the number of simulated points that fall into each cell. This is illustrated in Figure 2.4 where the blue dots represent a simulation of points scattered over the mesh generated by the Voronoi tessellation of the orange dots. The residual in cell nine, for example, is negative one. These residuals help to visualize cells containing higher or lower than expected randomly simulated vents (Fig. 2.S1a-b). Areal and density functions are also constructed for each simulated iteration, with all five thousand functions being averaged to create one areal function to describe the simulated data.

2.3.2.3 Constructing Areal Distribution and Density Functions

We represent the distribution of Voronoi cell areas produced from the observed vent location data as a cumulative distribution function (CDF), with the x-axis normalized by the area

of the largest Voronoi cell of the tessellation. The result is an area distribution function that can be used to compare the computed CDF of the observed data and simulated random data for each study field (Fig. 2.5). Note that the CDF of the simulated data appears smoother because it is the average of five thousand CDFs.

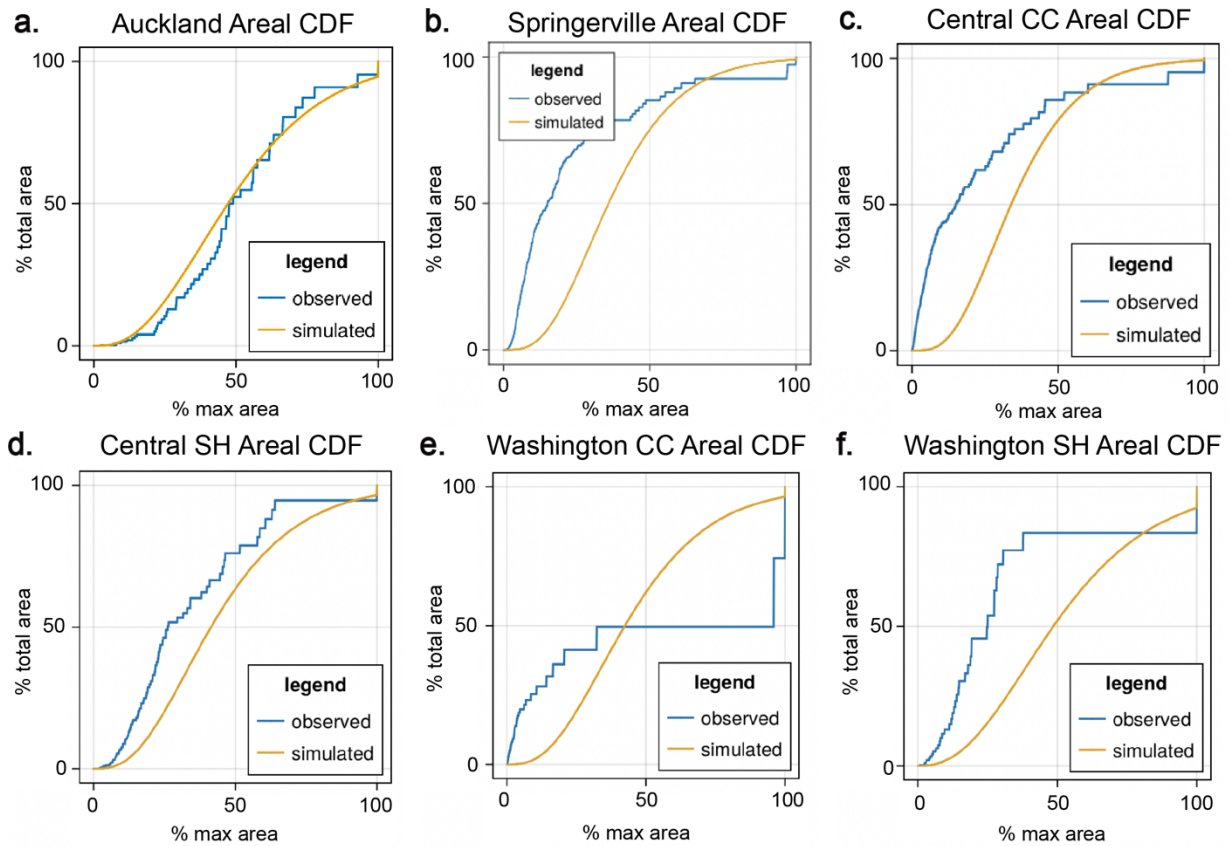


Figure 2.5. Areal CDFs for observed and simulated data for six study regions, (a) Auckland Volcanic Field, (b) Springerville Volcanic Field, (c) Central Cascades cinder cones, (d) Central Cascades shields, (e) Washington Cascades cinder cones, and (f) Washington Cascades shields.

The CDF of the Auckland Volcanic Field (AVF) closely follows the curve for the random simulated data (Fig. 2.5a); the CDF for the Springerville Volcanic Field (SVF), in contrast, shows a pronounced early departure from the simulated random process. The disproportionate contribution of small Voronoi cells to the total area reflects compression of space between clustered points (Fig. 2.5b). This rapid growth transitions into slower discrete jumps, signifying a shift towards fewer but larger cells within the tessellation. The Central Cascades cinder cones CDF

shows similar behavior (Fig. 2.5c), while the CDF for the Central Cascades shields shows initial rapid growth but an earlier transition to discrete jumps, indicating fewer small Voronoi cells than its cinder cone counterpart (Fig. 2.5d). The large gap between the cinder cone groups in the Washington Cascades yields a CDF dominated by large jumps (Fig. 2.5e). The CDF behavior of the Washington Cascades shields is similar to the Central Cascades shields although with a few cells of much larger area (Fig. 2.5f).

We can further emphasize the individual contribution of smaller Voronoi cell areas to the total distribution of areas by taking the derivative of the CDF to produce probability density functions (PDFs) of the observed and simulated data. Here the likelihood of having cells of a given size decreases as the interval over which the derivative is calculated decreases. This creates the jagged appearance of the density functions, and should be considered when setting the resolution for approximating the derivative.

2.3.2.4 Deriving an Intrinsic Length Scale from the Intersection of Density Functions

An intrinsic length scale can be derived for each study field of interest from the intersection of the observed and random density functions (Fig. 2.6), which peak at the most common values of Voronoi cell area. The simulated data have a PDF peak at 30-35% of the maximum cell area, consistent with the assumption of a Poisson random process; the peak of the observed data varies with the nature of each volcanic field. The intersection of the two PDFs indicates a change in behavior of the observed data relative to the random behavior of the simulated data. The first intersection point between the observed and simulated PDFs defines a corresponding point on the x-axis that represents a Voronoi cell area above which cells no longer contribute disproportionately to the total area of the Voronoi tessellation (they are no longer clustered). Note that in the Auckland volcanic field (AVF), the simulated and observed PDFs are similar, and there is no peak showing

a high contribution of smaller Voronoi cell areas. The resulting absence of an intersection point (Fig. 2.6a) indicates that the whole field can be described by random behavior, as noted by other studies (Le Corvec et al., 2013).

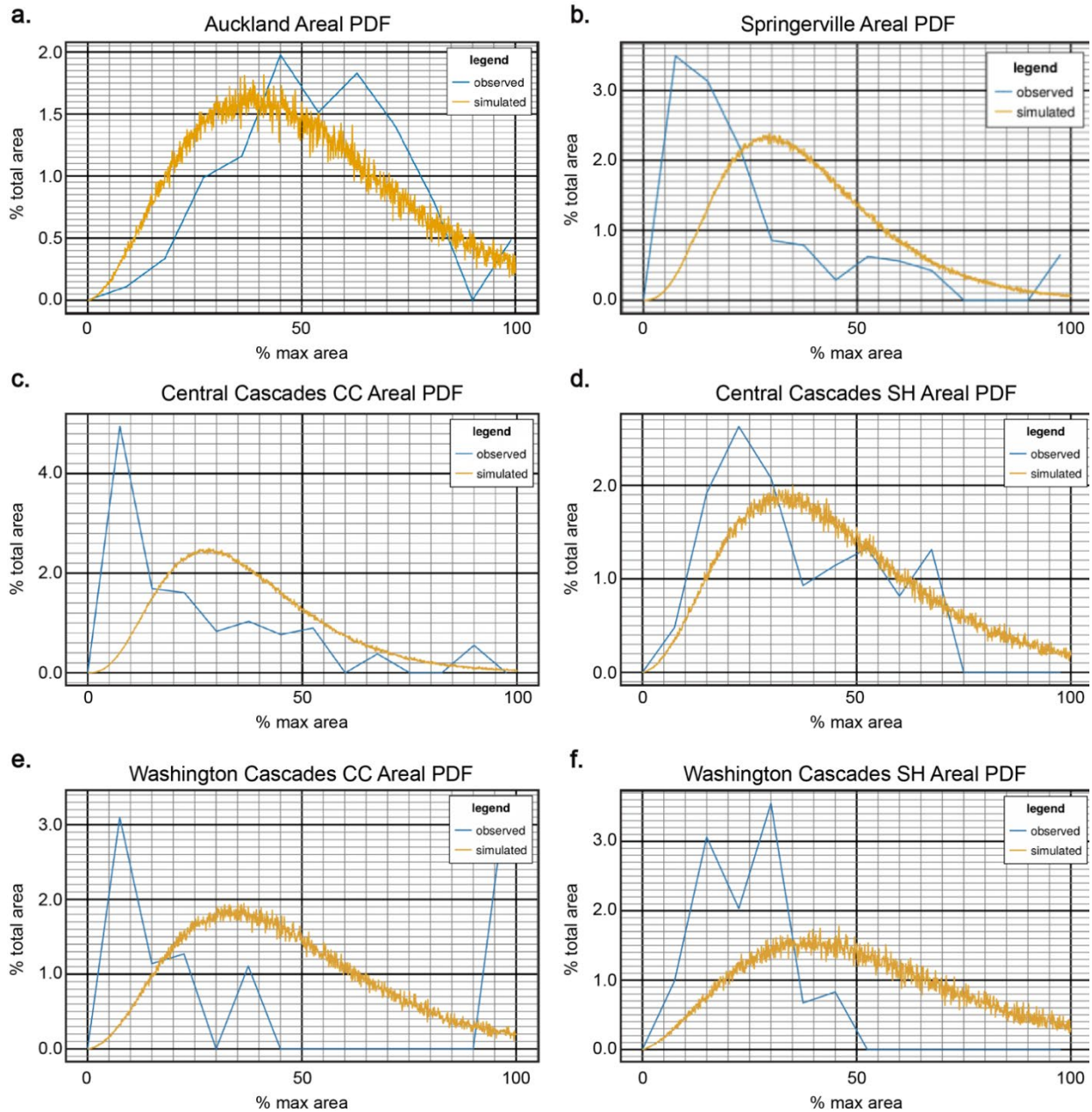


Figure 2.6. Areal PDFs for observed and simulated data for six study regions, (a) Auckland Volcanic Field, (b) Springerville Volcanic Field, (c) Central Cascades cinder cones, (d) Central Cascades shields, (e) Washington Cascades cinder cones, and (f) Washington Cascades shields.

Once an intersection point is located, the value can be converted to an area by multiplying the area of the largest cell in the Voronoi tessellation. The resulting area can be converted to a length scale by setting the area as a circle and solving for the radius. The result is an intrinsic length scale that marks the maximum length scale of clustering, as summarized in Table 1. This length scale can be visualized initially by use of the Voronoi tessellation, or by using the length scale as a bandwidth for Kernel Density Estimation.

2.3.3 *Kernel Density Estimation*

Kernel Density Estimation (KDE) is one of many techniques used to estimate the probability density function producing a given set of discrete data points. The main equation governing KDE is:

$$\hat{f}(x) = \frac{1}{nh} \sum_{i=1}^n K\left(\frac{x - X_i}{h}\right) \quad (2)$$

where X_i represents the points of the data set, h is the bandwidth (smoothing parameter), K is the kernel function, and n is the number of data points (Silverman, 1986). Strengths of KDE are that it does not rely on binning data and each data point retains its original location via the kernel function, which changes each piece of data from a point located at X_i to an interval centered at X_i (Węglarczyk 2018). User choices that affect the output of KDE are, most notably, the choice of kernel function and the bandwidth; while the kernel function can affect the results of the KDE (we use a quartic (biweight) kernel in ArcGIS), the choice of bandwidth has more impact (Silverman, 1986; Cressie, 1991; Lutz and Gutmann, 1995; Condit and Connor, 1996; Connor et al., 2019). A bandwidth that is too small produces low bias in the resulting PDF but high variance (undersmoothing), while a bandwidth that is too large has the inverse properties of high bias and low variance (oversmoothing). One technique for choosing bandwidth is Silverman's Rule of

Thumb ('Silverman's rule'; Silverman, 1986). It is adapted for use in two dimensions through ArcGIS' Kernel Density tool and is as follows:

$$h = 0.9 * \min(SD, \sqrt{\frac{1}{\ln(2)} * D_m}) * n^{-0.2} \quad (3)$$

and compares the standard distance (SD) and the median distance (D_m) from the calculated mean center of data points (h is the calculated bandwidth and n is the population of data points). SD measures the compactness of a distribution and is typically represented as a circle around the mean center. D_m is calculated as the median of the distance of each point from the mean center. Silverman's rule compares both distances: the standard distance is more applicable for data without strong directional trends while the median distance works well in cases of skewed data. In this way, an appropriate bandwidth for KDE can be calculated for volcanic fields that vary in overall shape (Fig. 2.S2).

We perform KDE analysis on the four volcanic fields described above (Auckland, Springerville, Central Cascades and Washington Cascades) using the bandwidth produced by Silverman's rule and the intrinsic length scale from the Voronoi methodology (Table 1). Each dataset is read into ArcGIS as a point layer with latitude and longitude coordinates. The coordinate system of the data is then converted from WGS84 to UTM to allow two-dimensional distance analyses. The boundary region used for each field is the convex hull generated for the Voronoi analysis.

2.4 Results

The goal of this work is to use the derived length scale to visualize clustering where present for the studied volcanic fields and to begin exploring structures that cause this clustering. To do this, we visualize the volcanic fields in two ways. The first is by shading the Voronoi diagram for

each field by the critical area, which provides an overview of how many vents are associated with cells within the critical area range and where they sit in the field. The second is through KDE maps produced using both the Silverman and Voronoi bandwidths (Table 2.1). Trends in clustering are identified by comparing KDE distributions between fields.

Volcanic Field	SD (m)	D_m (m)	Silverman's Bandwidth (m)	Voronoi Intersection (%)	Voronoi Bandwidth (m)
Auckland	8220	9608	3344	-	-
Springerville	17215	18459	4633	16	2125
Central Segment of Cascades (Cinder Cones)	72645	53528	13454	16.5	7633
Central Segment of Cascades (Shields)	77882	67320	24545	32	7702
Washington Segment of Cascades (Cinder Cones)	95414	47234	17359	17.5	17845
Washington Segment of Cascades (Shields)	29149	22916	9964	35	8683

Table 2.1 Summary of Field Distances/Statistics. For each volcanic field and type of vent (cinder cone or shield) analyzed in this study, the standard distance, median distance, Silverman's bandwidth, intersection percentage with Voronoi, and Voronoi bandwidth were calculated.

2.4.1 Individual Field Results

2.4.1.1 Auckland Volcanic Field (AVF)

The spatial arrangement of AVF vents shows no intersection between the Voronoi cell and random distributions, indicating that the two are indistinguishable and that there is no Voronoi 'cluster' distance to use as a bandwidth (Fig. 2.6a). The Voronoi tessellation of the AVF also shows cells of generally the same area across the field (Fig. 2.7a). Application of Silverman's rule shows that the standard distance (SD) is smaller than the median distance (D_m) and is therefore

used for KDE analysis. The resulting bandwidth (3,344 m) produces KDE contours that show some higher density regions in the south; density values that peak at 0.384 km^{-2} in the western part of the field (Fig 2.7b). Note that the entire field is connected by a continuous contour, except for Rangitoto to the northeast (Fig. 2.7a). Rangitoto is also the largest by volume and the only vent to exhibit potential shield building, which might suggest a change in behavior.

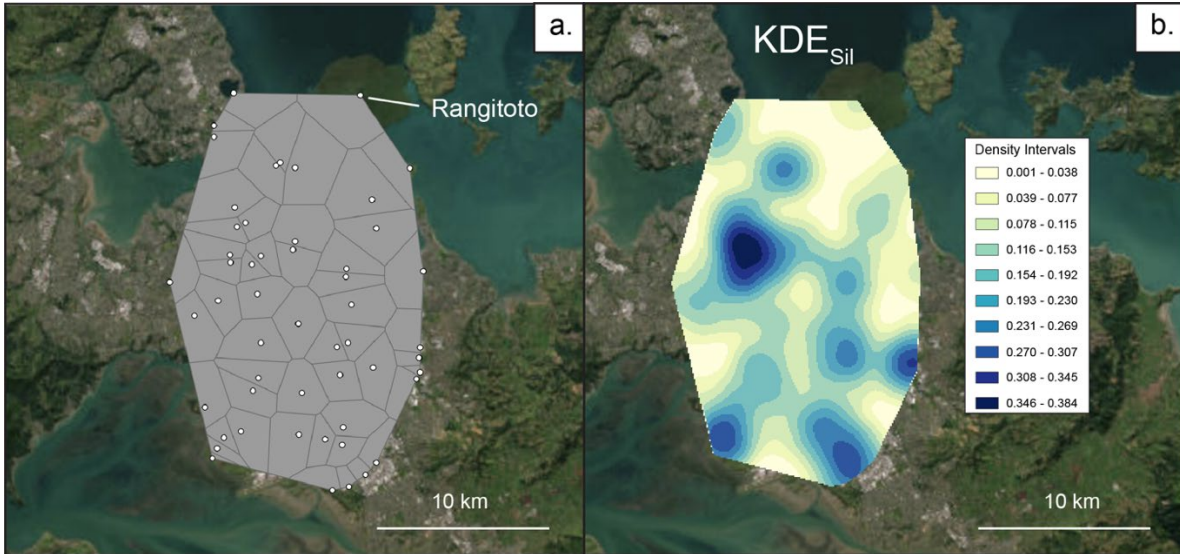
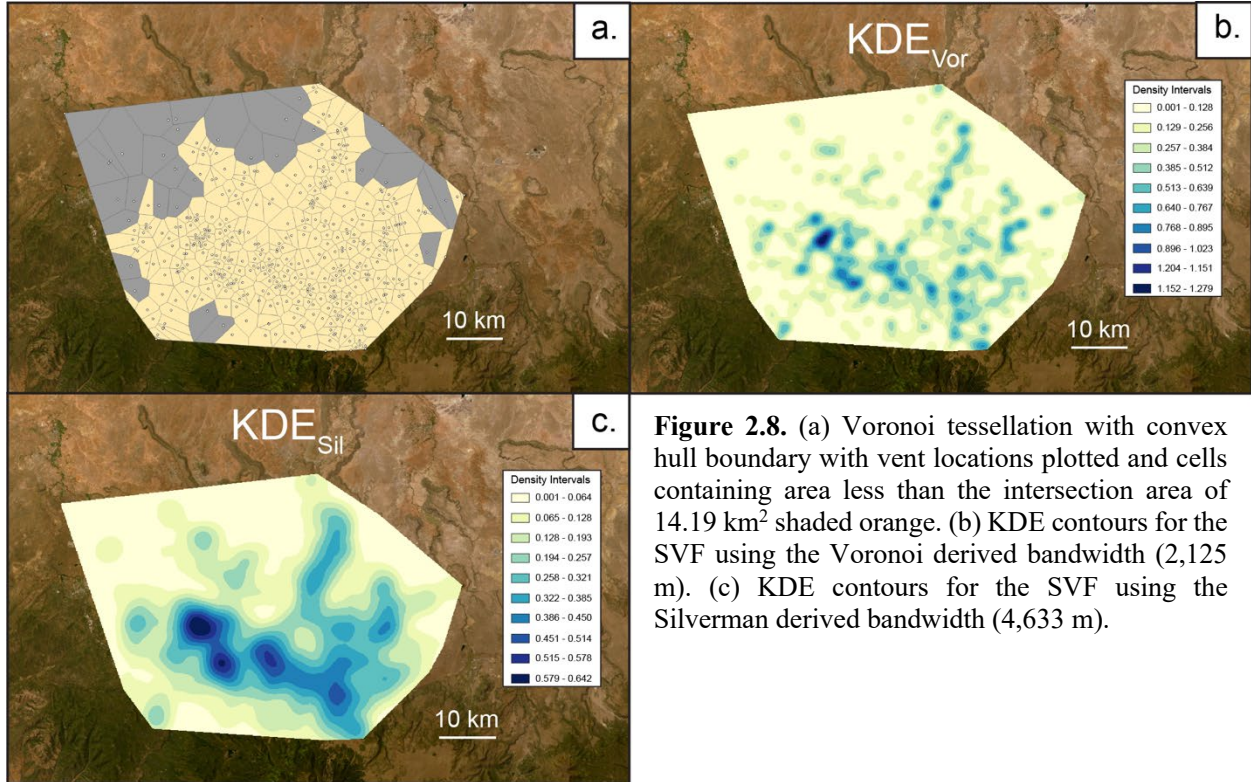


Figure 2.7. (a) Voronoi tessellation with convex hull boundary with vent locations plotted. (b) KDE contours for the AVF using the Silverman bandwidth (3,344 m).

2.4.1.2 Springerville Volcanic Field (SVF)

Most cells in the Springerville Voronoi tessellation are smaller than the critical area found by the PDF intersection (Fig. 2.6b); cells larger than the critical area fall mostly in the northwest of the field while clustering is greater to the south (Fig. 2.8a). The clear PDF intersection (Fig. 2.6b) yields a Voronoi length of 2,125 m (Table 1). The Silverman's bandwidth (calculated using *SD*) of 4,633 m is more than double the Voronoi-derived bandwidth. The highest KDE density value from Silverman's bandwidth (KDE_{Sil}) is 0.642 km^{-2} and is located just west of the center of the field, near two additional high density regions to its east (Fig. 2.8c). Three distinct features on the northern edge of the field radiate outward in the NW, N, and NE directions. While KDE_{Sil} shows a nearly continuous contour across the entirety of the field, the KDE using the smaller

Voronoi bandwidth (KDE_{Vor}) has numerous isolated contours, particularly in the NW (Fig. 2.8b), and shows a more elongated region of peak density values of 1.279 km^{-2} . KDE_{Vor} also highlights the continuity of the N-trending feature.



2.4.1.3 Central Cascades

The Voronoi tessellation for the Central Cascades cinder cones shows strong N-S variation with large cells to both the west and east (off-axis; Fig. 2.9a). The only isolated vent cluster is in the southwest. KDE densities for the Central Cascades cinder cones are highest near the center of the segment (Fig. 2.9b,c). Unlike the AVF and SVF, $D_m < SD$ meant that D_m was used to calculate a Silverman bandwidth of 13,454 m, slightly less than double the Voronoi bandwidth of 7,633 m. KDE_{Sil} forms narrow low density contours on the northern and southern edges of the segment, with higher densities ($> 0.212 \text{ km}^{-2}$) at the center, near the Three Sisters (TS; Fig. 2.9d). This large high density region lies within the transition zone between volcanism along the Cascade Volcanic

Arc and the back-arc Newberry volcanic field (NB; Fig. 2.9). From this we conclude that despite our attempt to remove Newberry centers, the structural effects of Newberry could be influencing the results, as highlighted particularly by KDE_{Vor} . The peak vent density of 0.380 km^{-2} occurs in two high density regions between Mt. Jefferson (MJ) and the Three Sisters. Again the smaller bandwidth means that KDE_{Vor} defines more isolated contours than KDE_{Sil} , such that only the central portion has a continuous contour (Fig. 2.9b).

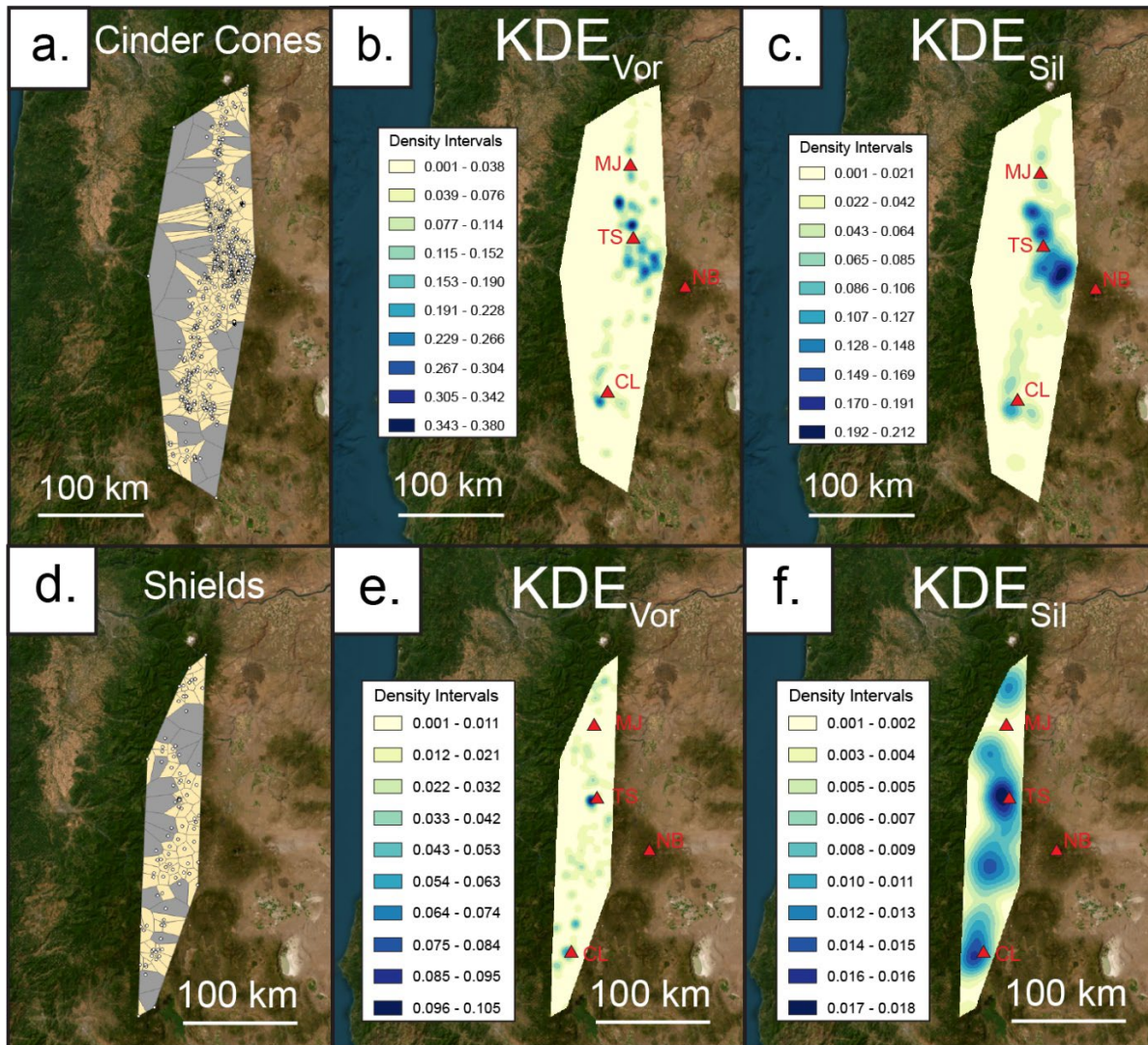


Figure 2.9. Voronoi tessellation for Central Cascades (a) cinder cones and (d) shields using convex hull boundary with vent locations plotted and cells containing area less than the intersection area shaded orange (183.059 km^2 and $.186.364 \text{ km}^2$ respectively). KDE contours using the Voronoi derived bandwidth for (b) cinder cones (7,633 m) and (e) shields (7,702 m) and using the Silverman derived bandwidth for (c) cinder cones (13,454 m) and (f) shields (24,545 m). (MJ – Mt. Jefferson, TS – Three Sisters, CL – Crater Lake, NB - Newberry)

The Voronoi tessellation for the Central Cascades shields shows three main vent clusters; one group lies to the north, one in the center on the eastern side, and one in the southern portion of the field (Fig. 2.9d). While the north and east groups fall where the small cinder cone cells are located, the southern group of small shield cells appears correlative with a line of large area cells in the cinder cone tessellation (Fig. 2.9d). KDEs for the Central Cascades shield volcanoes vary substantially when using the Silverman and Voronoi bandwidths: Silverman's bandwidth is 24,545 m, more than three times the Voronoi bandwidth of 7,702 m. As a result, the peak density for KDE_{Vor} (0.105 km^{-2}) is nearly an order of magnitude higher than for KDE_{Sil} (0.018 km^{-2}), and there are many more isolated density peaks for KDE_{Vor} (Fig. 2.9e,f). Both KDEs show the highest density region falling just west of the Three Sisters and between the two high density areas of the cinder cone vents (Fig. 2.9b,c); there is also less apparent influence from Newberry.

2.4.1.4 Washington Cascades

The Voronoi tessellation for the Washington Cascades cinder cones shows two main clusters (Fig. 2.10a). Corresponding KDEs show high density regions in the south, where most vents are located (Fig. 2.10b,c). Similar to the Central Cascades, D_m was used for Silverman's Rule to produce a bandwidth of 17,359 m, nearly identical to the Voronoi bandwidth of 17,845 m; the similarity is likely a consequence of the large central Voronoi cell (Fig. 2.10a) and shows that the Voronoi bandwidth increases when small clusters of vents are far apart. As the two KDE results are nearly identical, we describe only KDE_{Vor} , which shows two high density regions, the first lying south of the midway point between Mt. St. Helens (MSH) and Mt. Adams (MA) and the second located directly south of Mt. Adams (Fig. 2.10c). The peak density of 0.045 km^{-2} only occurs in the first region. There are also two small regions of higher density values associated with the two small clusters to the north.

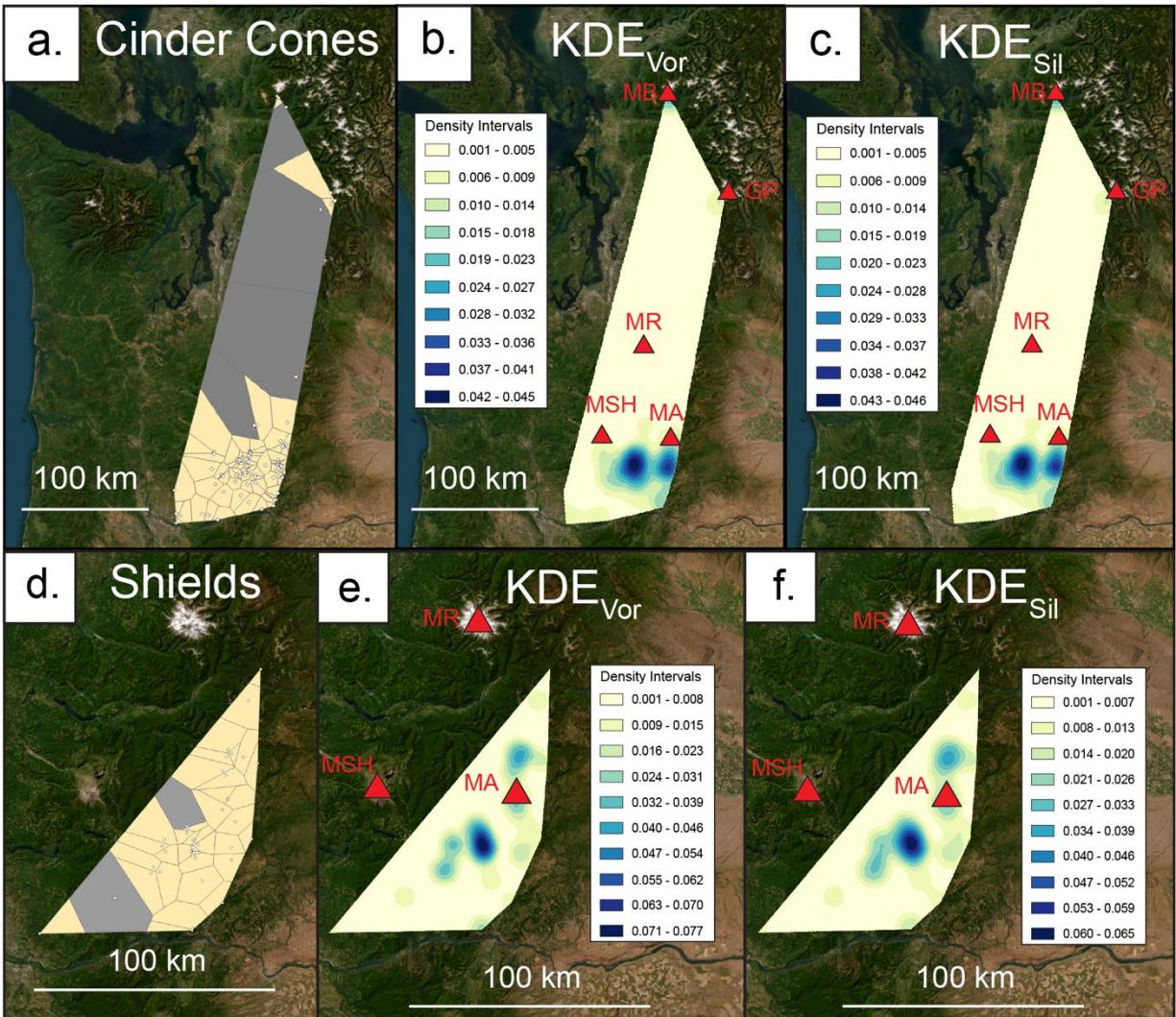


Figure 2.10. Voronoi for Washington Cascades (a) cinder cones and (d) shields using convex hull boundary with vent locations plotted and cells containing area less than the intersection area shaded orange (1000.487 km² and 236.881 km² respectively). KDE contours using the Voronoi derived bandwidth for (b) cinder cones (17,845 m) and (e) shields (8,683 m) and using the Silverman derived bandwidth for (c) cinder cones (17,359 m) and (f) shields (9,964 m). (MB – Mt. Baker, GP – Glacier Peak, MR – Mt. Rainier, MSH – Mt. St. Helens, MA- Mt. Adams)

Shield volcanoes in the Washington Cascades lie only in the southern cluster and most cell areas are smaller than critical (Fig. 2.10d), with the exception of the western portion of the field. Again, Voronoi and Silverman bandwidths are similar, at 8,683 and 9,964 m respectively. The peak densities are also similar (Fig. 2.10e,f) with a location that lies between the two high density regions highlighted in the cinder cone KDEs (Fig. 2.10b,c). In this regard, the Washington and Central Cascades show a similar relationship between the peak density regions for cinder cones

and shields, although the trend of shield volcanoes in the Washington segment narrows to the east and ends before Mt. Rainier (MR).

2.4.2 Comparing Vent KDE Values

We have visualized which vents are associated with clustered Voronoi cells (cells with area less than our length scale where behavior transitions from clustered to random), and we have then produced Kernel Density Estimation (KDE) maps at two different bandwidths to see how density patterns change between a distance-based (Silverman) and area-based (Voronoi) metric. We now (1) normalize both KDE_{Sil} and KDE_{Vor} for each volcanic field, (2) find the normalized density values from both KDE maps at points where vents are located, and (3) produce CDFs of the normalized density distributions (Fig. 2.11). Doing this allows us to compare behavior across fields and view relations between density values and vent characteristics (see discussion for the latter). Unlike our previous CDF curves of Voronoi cell areas where small cell areas were related to clustering (Fig. 2.5), now higher normalized density values are related to clustering.

The normalized KDE_{Sil} density values for Auckland create a linear CDF, with vents neither being located on very low (< 0.1) or very high (> 0.9) density regions (Fig. 2.11a). Meanwhile for Springerville, 60% of KDE_{Sil} normalized density values for vents are ≤ 0.5 , with 5% of values falling between 0.9 and 1. This difference in behavior of a known random field (AVF) and a known clustered field (SVF) is intuitive, as when clustering occurs, the densest cluster will produce high values while vents outside the cluster will have lower values. The Central Cascades and Washington Cascades cinder cones follow a similar initial increase to the SVF (Fig. 2.11a); then after reaching normalized density values of 0.5, the Central Cascades cinder cone CDF becomes approximately linear while the Washington Cascades cinder cone CDF is marked by discrete jumps in value (likely from the discrete clusters). The Washington shields CDF also shows discrete

steps, while having the highest percent of normalized density values ≤ 0.5 (70%). The Central Cascades shields CDF however, follows the AVF's trend closely, except for tail values < 0.2 and > 0.9 .

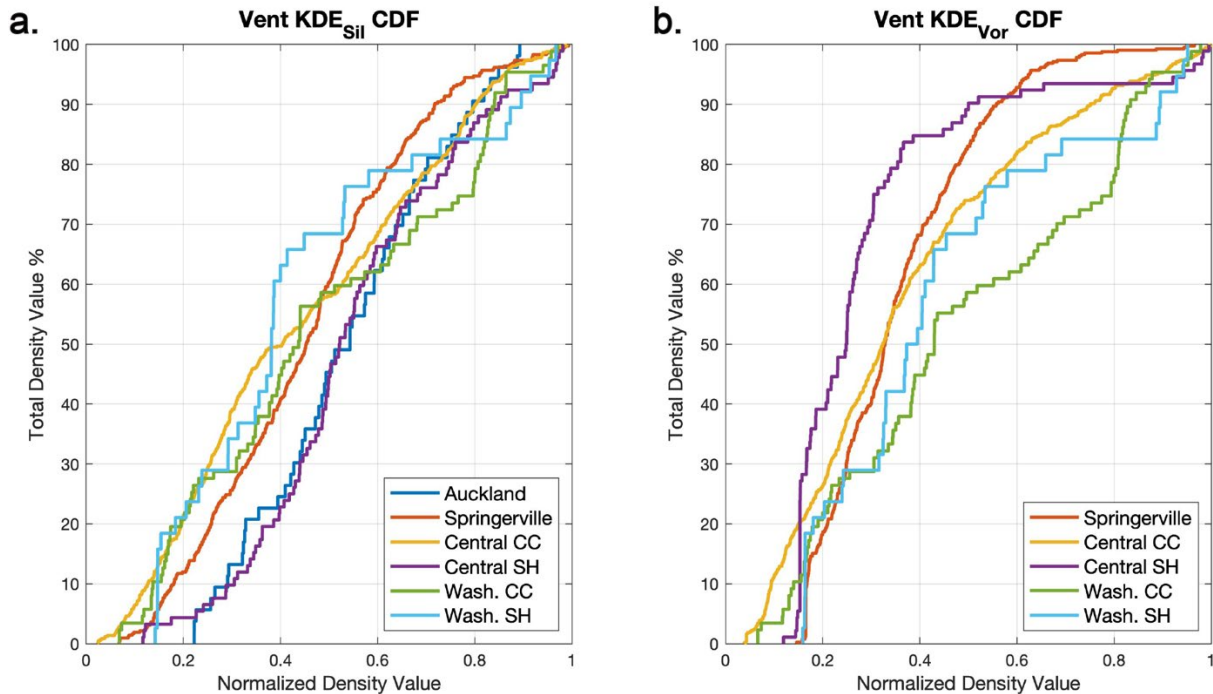


Figure 2.11. CDF plots for normalized density values from (a) KDE_{Sil} and (b) KDE_{Vor} at individual vents across each volcanic field (CC – Cinder Cones, SH – Shields).

While CDFs based on KDE_{Sil} densities can be used to compare behavior between a random field and a clustered field, KDE_{Vor} assumes clustering is present, and differences in CDFs of KDE_{Vor} density values at vents record details of clustering behavior. There is an ever further emphasized predominance of normalized density values ≤ 0.5 at vents for the SVF, Central Cascades cinder cones, and Central Cascades shields (Fig. 2.11b). The Central Cascades shields CDF experiences the most dramatic change (due to the length scales having the greatest difference), with 90% of its density values ≤ 0.5 with very few values ranging 0.5-0.9 and the remainder at high values > 0.9 . CDFs derived from both KDE_{Vor} and KDE_{Sil} are similar for the Washington Cascades cinder cones and shields, a result of the similar bandwidths for these fields.

2.5 Discussion

2.5.1 Comparison with Previous Field Findings

A notable feature of the Auckland Volcanic Field (AVF) is that the PDF does not intersect that of the random distribution (Fig. 2.6a), indicating that there is no length scale where behavior transitions from random to clustered. Poisson (PNN) analysis of the AVF also finds the vent distributions to be consistent with a Poisson process (randomly distributed; Le Corvec et al., 2013b). Additionally, the location of the older vents does not appear to provide a guide to younger vent locations (Bebbington & Cronin, 2011), although the spatial information may provide information on eruption volume, with larger eruptions filling in spatial gaps (Bebbington, 2015). KDE_{Sil} (Fig. 2.7b) highlights the same higher intensity regions found using other isotropic kernel functions (Bebbington, 2013). The slight SW-NE alignment of the KDE_{Sil} contours is further emphasized by KDEs produced with anisotropic kernels, indicating a structural control of vent alignments over the field (Bebbington & Cronin, 2011; Bebbington, 2013; 2015).

All other study regions have intersection points between observed and random PDFs, indicating that they all have a maximum distance of clustering before random behavior initiates. PNN analysis of Springerville (SVF) has also shown clustering behavior (Le Corvec et al., 2013a). For comparison we also performed PNN analysis on our fields of interest that have Voronoi length scales. All except the Central Cascades shields yielded R values less than one, indicating clustering (Table 2.S1). The R values for the Central Cascades and Washington Cascades cinder cones of 0.49 and 0.43, respectively, are substantially less than that of the SVF, indicating a higher degree of whole field clustering. Similarly, CDFs derived from KDE_{Vor} show greater percentages of normalized densities > 0.5 for both the Central and Washington cinder cones than the SVF (Fig. 2.11b). The R value for the Central Cascades shields is 1.005 which aligns with Poisson behavior. The shaded Voronoi diagram, however, shows distinct clusters of small cells separated by larger

area cells (Fig. 2.9d). Returning to the CDF from KDE_{Sil} density values (Fig. 2.11a), the Central Cascades shields behave similarly to the AVF (known to have PNN values also around 1 indicating random behavior; Le Corvec et al., 2013a) except for the two end tails. This highlights an important feature of the Voronoi methodology: it can distinguish between fields with random vent locations (AVF) and fields that appear random with linear distance metrics but show clustering behavior by area (Central Cascades shields). In detail, PNN analysis of cinder cones around Crater Lake (CL – Fig. 2.9), in the southern part of the Central Oregon segment, yields R values of ~0.18-0.5 using 50 ka bins (Karlstrom et al., 2015), which overlaps with an R value of 0.49 for the entire segment.

We also calculated K-Ripley's statistic in ArcGIS for the AVF and SVF as our known random and clustered field (Ripley, 1981). This function calculates the dominance of clustering or dispersion at different length scales. We calculate the statistic in ArcGIS for the AVF and the SVF for length scales ranging 500 to 10,000 m in 500 m increments across our convex hull areas for the fields; the resulting output gives 1) an observed K distance calculated from the field vents, 2) an expected K distance, and 3) upper and lower confidence envelopes of 99.9% (generated by running 999 permutations). If the observed K distance is higher than the expected K and the upper confidence limit, then there is statistically significant clustering, while if the observed K is lower than the expected K and lower confidence limit then there is statistically significant dispersion. At every length from 500 m to 10,000 m in 500 m increments, Auckland showed no significant clustering, while Springerville showed significant clustering at every length (Fig. 2.S3), marking agreement with previous findings as well as ours that Auckland doesn't show clustering while Springerville does (we do note that using different confidence intervals it is possible to find length scales of potential clustering for Auckland; Magill et al., 2005). These methods provide a useful

benchmark for comparing our results, but we can take our spatial description further by evaluating different vent properties (e.g. composition, age) in comparison with our density values.

2.5.2 Exploring Structures with Silverman and Voronoi

To study structures within each of these fields, we combine spatial analysis data with available age and composition data. While the AVF does not show signs of clustering, the field includes pairs of vents that are in spatial (< 3 km) and temporal (< 7 ka) proximity to each other throughout the field (Fig. 2.12a). Most of these pairings are NE-SW aligned, similar to the features highlighted in the AVF KDE_{Sil} (Fig. 2.7b) and occurring throughout the field's eruptive history: Onepoto (ON) and Tank Farm (TF) vents erupted at 187.6 ka and 181.0 ka and Purchas Hill (PH) and Mount Wellington (MW) erupted at 10.9 and 10.0 ka. The NE-SW structural alignment of the paired vents further supports tectonic structural control on the AVF throughout the entire history of the field. In general, it seems that the AVF is random by all metrics with vents produced by magma rising quickly from the mantle (no crustal residence) and being influenced by tectonic structural controls.

Regional tectonics have also influenced the SVF, dominated by NW-trending strike slip faults (Crumpler, 1992). Several NW-trending features appear in the KDE_{Sil} for the SVF (Fig. 2.8c), but in contrast to the AVF, Springerville vents are also clustered. The absence of fissure vents in the SVF (Crumpler, 1992) and the proximity of vents with differing magma compositions (Connor, 1992) suggests that these clusters are not purely tectonic. Comparison of normalized KDE_{Vor} density CDFs for vents of different compositions (Fig. 2.12b,c) shows that the alkali basalt vents CDF contains a higher percentage of high density values than CDFs for hawaiite and transitional basalt. This suggests that the clustering length scale found with the Voronoi methodology could be related to conditions of magma storage, while the absence of a

compositional distinction in normalized density CDFs using the Silverman bandwidth may reflect more regional tectonic influence.

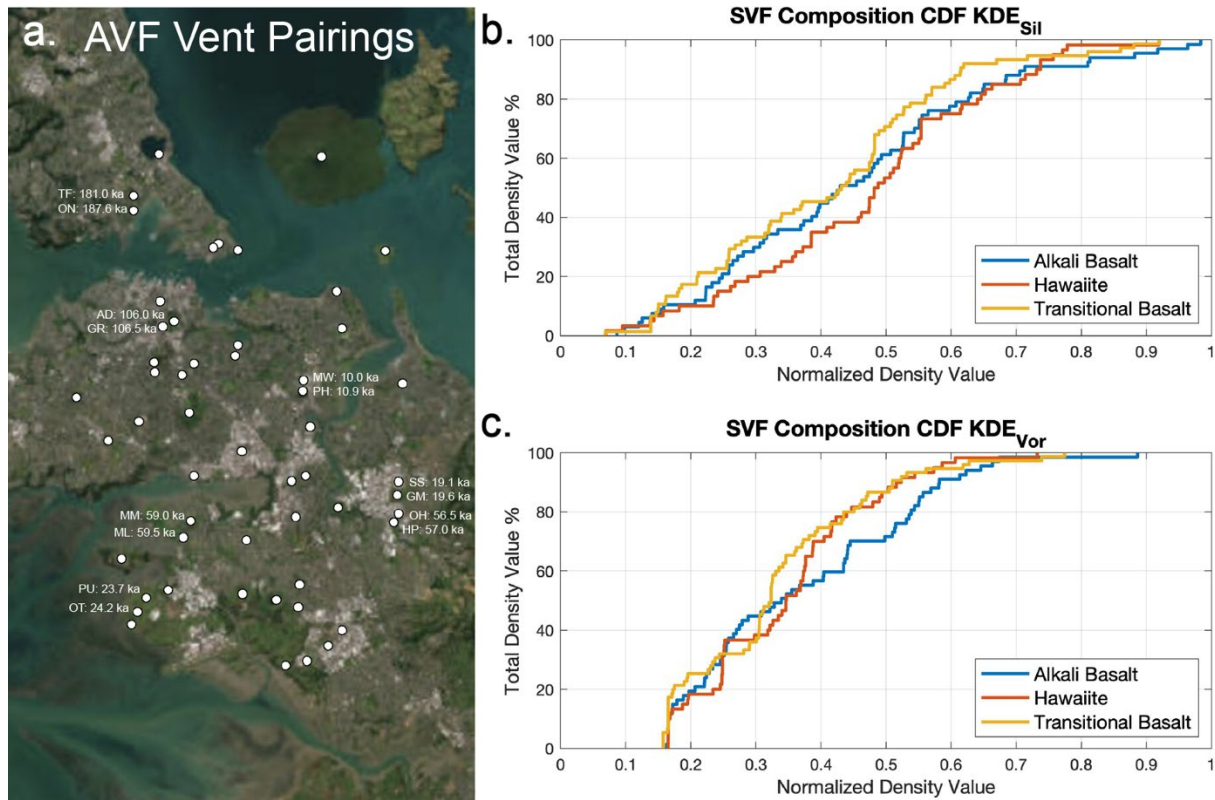


Figure 2.12. (a) Map of AVF with vents that erupted in spatial and temporal proximity notated. CDF plots of SVF normalized density values from (b) KDE_{Sil} and (c) KDE_{Vor} at vents with three compositions (alkali basalt, hawaiite, and transitional basalt). (TF – Tank Farm, ON – Onepoto, AD – Auckland Domain, GR – Grafton, MW – Mt. Wellington, PH – Purchas Hill, MM – Māngere Mt., ML – Mangere Lagoon, PU – Pukeiti, OT – Ōtuataua, HP – Hampton Park, OH – Ōtara Hill, SS – Styaks Swamp, GM – Green Mt.)

In the Cascades, the lower age resolution, complex tectonics, and interplay between distributed and focused volcanism (including the dominant stratovolcanoes) makes the spatial structure of vents more difficult to interpret. We start by separating the normalized density values located at vents for each field by time epoch (Early Pleistocene, Middle Pleistocene, and Late Pleistocene/Holocene combined). Note that these density values are from KDE done on the present state of the fields (Fig 9,10), not individual KDEs for each epoch. For the Central Cascades cinder cones, density values are higher for younger vents, consistent with better preservation (Fig. 13a,b). The Central Cascades shields show the greatest discrepancy between KDE_{Sil} and KDE_{Vor} , a result

of large differences between bandwidths. In contrast, epoch-based CDFs for the Washington Cascades cinder cones and shields are similar for KDE_{Sil} and KDE_{Vor} because the bandwidths are nearly identical (Fig. 2.13e-h).

When viewed by age, the Washington Cascades segments shows some interesting patterns. Here density values for cinder cones are higher in the Early and Late Pleistocene and lower in the Middle Pleistocene. The opposite pattern is seen for the shield volcanoes, with lower density values in the Early and Late Pleistocene and higher values in the Middle Pleistocene. These data suggest that dispersed volcanism (clustered cinder cones) dominated the Early and Late Pleistocene while volcanism was more focused (clustered shields) in the Middle Pleistocene. Interestingly, construction of the current main edifices of Mount Rainier and Mount Adams began in the Middle Pleistocene (Hildreth, 2007). The switch from distributed to focused volcanism in the southern portion of the Washington segment is also suggested by a volume-weighted Gaussian kernel analysis (O'Hara et al., 2020). In the Central Cascades segment, in contrast, the general increase in cinder cone density values with time might suggest a change from focused to distributed volcanism, consistent with evidence for extension across this segment of the arc (Wells & McCaffrey, 2013). Though again, this could also be an artifact of better preservation of later erupted vents.

2.5.3 A Novel Clustering Length Scale

An ongoing challenge with studying distributed volcanism is how to characterize spatial patterns of eruptive behavior. Here we suggest an area-based measure that differs from existing options in two important ways: (1) we choose to use area instead of distance because of the two-dimensional nature of location data, and (2) we measure the observed departure of vents from the random distribution for vents rather than attempting to infer an underlying distribution.

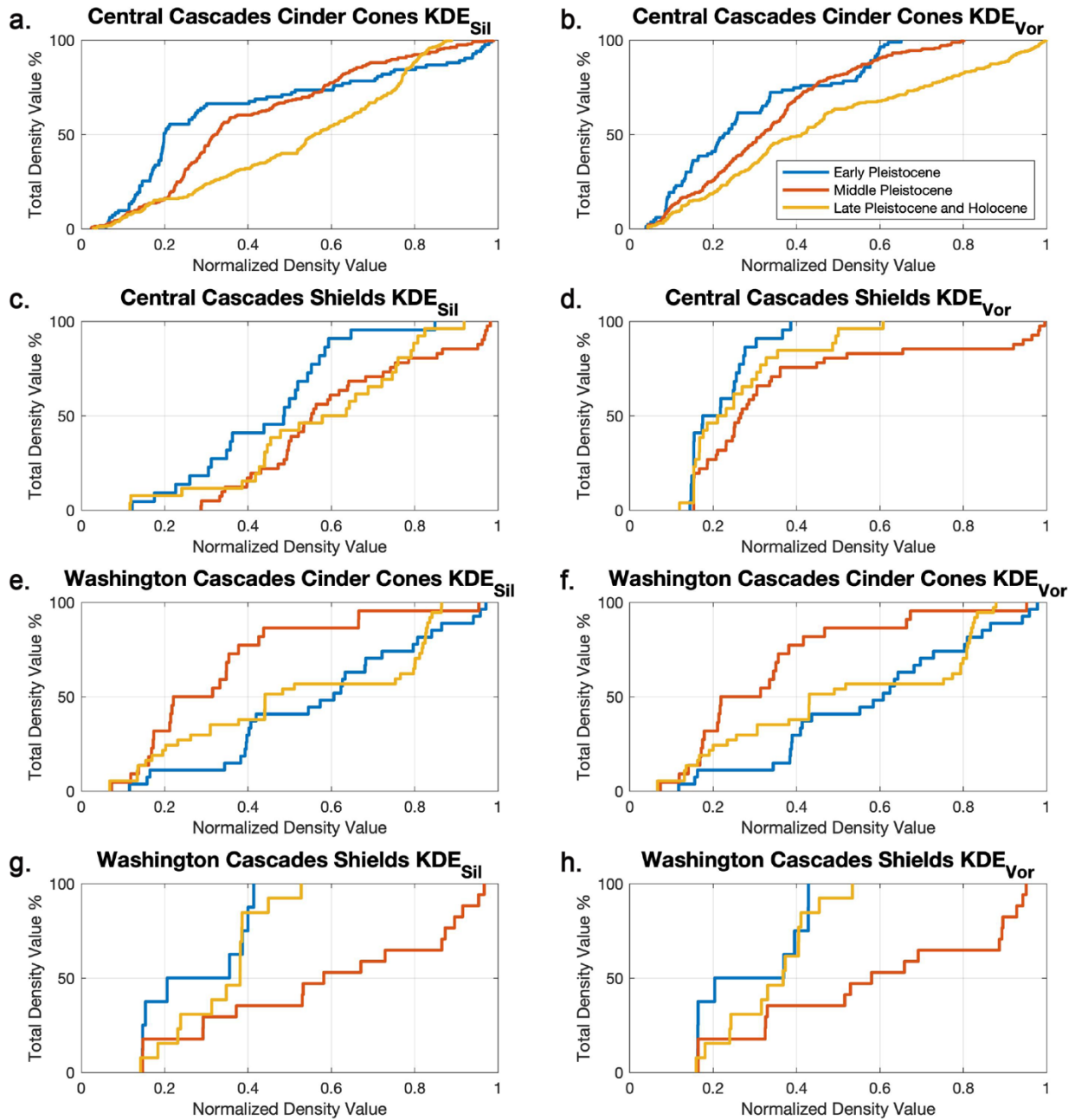


Figure 2.13. CDF plots for normalized density values from KDE_{Sil} (a,c,e,g) and KDE_{Vor} (b,d,f,h) associated with vents for each field of interest in the Cascades.

2.5.3.1 Using Area as a Measure of Departure

Our methodology aligns with the conventional use of a homogeneous Poisson process to describe a random distribution of vents. In nearest neighbor analysis, however, distributions of distances are used to compare to random expectations, which can be determined analytically but

are constrained to a one-dimensional measure of comparison. Voronoi tessellations, in contrast, allow the distribution of areas to be compared with the distribution of Voronoi cells generated by a homogeneous Poisson process (Hinde & Miles, 1980; Tanemura, 2003).

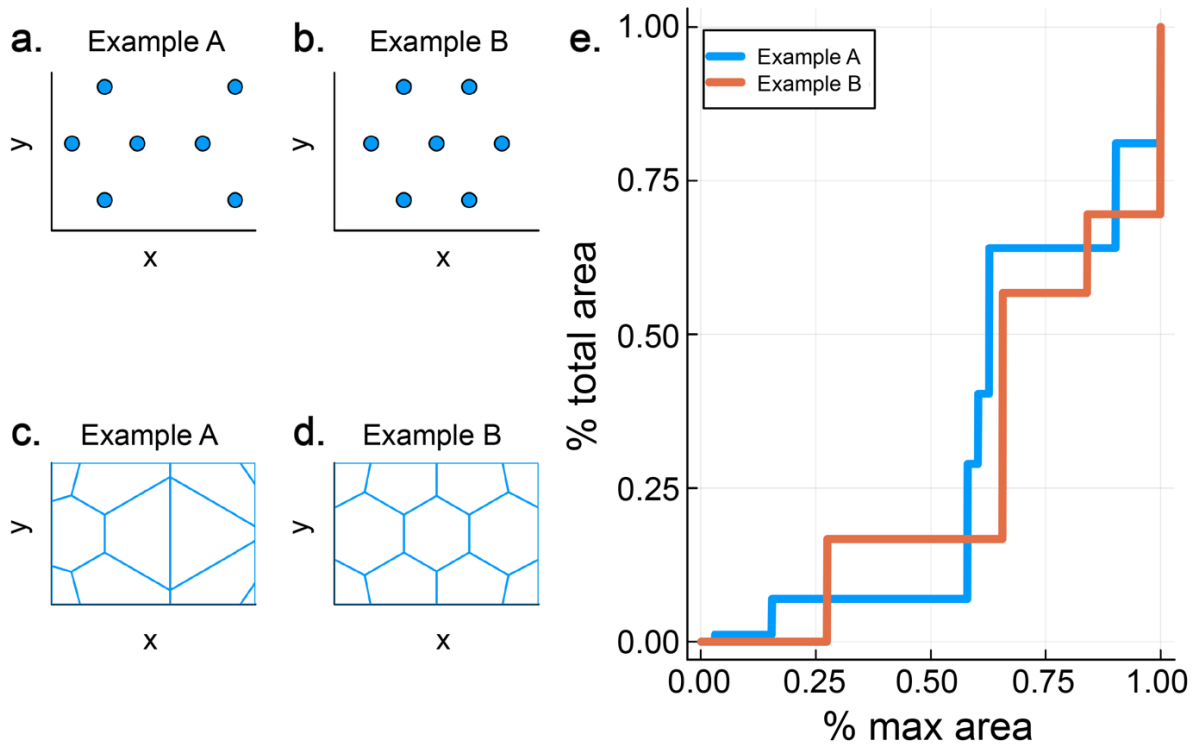


Figure 2.14. Simulated vent locations (a-b) and Voronoi tessellations (c-d) for example A and example B respectively. (e) Areal CDFs produced by examples A and B.

We emphasize the difference between using linear distance and area measures with a simple synthetic experiment (Fig. 2.14). Here examples A and B are constructed such that the nearest-neighbor distance for each point is one unit-length (Fig. 2.14a,b). For example A, this is ensured by putting two equilateral triangles (the diamond) one unit length away from an isosceles triangle. In example B we construct a regular hexagon. Both examples contain seven points with identical nearest neighbor distributions that cannot be distinguished using a measure of distance (e.g. Poisson nearest neighbors). Visually, however, they represent different spatial structures (not just rotations or reflections), and produce different Voronoi cell configurations (Fig. 2.14c,d). A

comparison of areal CDFs for the two examples shows differences between resulting curves, even with only seven points (Fig. 2.14e). Derived PDFs would also produce two different clustering length scales. A strength of our methodology is the ability to distinguish between these alternate vent placements and produce measures that describe each.

2.5.3.2 Avoiding Inferring an Underlying Distribution

A KDE is an approximate representation of an underlying probability density function (PDF) that depends on the bandwidth used. Bandwidth is usually selected based on its ability to minimize some error function between a trial PDF and the KDE. Even when assuming the same form, however, different selection methods can yield different results (Canon Tapia, 2022). Our approach side-steps this problem by using as reference the known underlying PDF for randomly scattered vents. This allows us to identify where an observed distribution departs from random in a way that signifies clustering, as in nearest neighbor analysis. The added value of our approach is that the resulting length scale determines when the behavior stops and which vents are associated with that length scale, allowing us to view changes in clustering across fields rather than describing the field as a whole. While this methodology does not attempt to recover the actual PDF and produces one length scale to describe behavior change when others might exist, it allows us to identify the length scale that identifies clustering. Furthermore, since this approach does not rely on assumptions about a potential underlying PDF it is easy to compare results between volcanic fields. To summarize, we define an easy-to-identify bandwidth that always means the same thing, which is the length scale for a volcanic field at which the areal clustering becomes less than expected when compared to a random process.

2.5.4 Future Considerations

2.5.4.1 Understanding Length Scales and Artifacts

Many of the PDFs for the volcanic fields (Figure 2.6) show multiple peaks in the observed results, as well as multiple intersection points with the simulated random PDF. The nature of these peaks is an interesting point of study for future work, as they could characterize length scales that are more and less affected by the formation of clusters. One issue is the conservation of total area, such that an increase in the total area contributed by smaller cells must come at the expense of cells at some other length scale. This compensation does not have to be evenly distributed over the remaining cells, yielding peaks and troughs such as those present in the PDFs of the Central Cascades cinder cones and shields.

This tradeoff in distribution of areas must be balanced against the presence of artifacts in large cells. Over multiple simulations, peaks occur at different places on the x-axis, creating spikes in the observed data (Fig. 2.15a). Sequential generation of a synthetic vent field from a normal distribution shows that the proportion of total mass in the first third of the curve remains fairly constant, while the mass in the tails is more erratic. This variability produces a thin tail when averaged over many simulations, (Fig. 2.15b). The second intersection point for the Springerville PDF (Fig. 6b), for example, is likely an artifact; an even clearer example can be found in the PDF of the Washington Cascade cinder cones (Fig. 2.6e). Here the spike at the right side of the PDF reflects the large distance between the cinder cones near Mt. Adams and the small groups of cinder cones near Glacier Peak and Mount Baker. We elected to keep these cones in our analysis to view how they would affect the distributions and clustering length scale for a segment spanning the northern reaches of Washington, but future analysis could remove these clusters to determine a clustering length scale for the cones around Mount Adams and Mount St. Helens.

2.5.4.2 Additional Statistical Analysis

Additional methods used to apply KDE to volcanic fields include bandwidths found using a cross validation method (Duong et al., 2007) or methods such as Least Squares Cross Validation (LSCV) or Sum of Asymptotic Mean Squared Error (SAMSE; Duong & Hazelton, 2003). Often these methods are used when producing spatio-temporal or spatio-volumetric models of volcanic fields with the intent to forecast future vent locations or hazards (Bebbington, 2013; Kiyosugi et al., 2010). Comparison between our length scale and these methods, as well as deeper exploration between distance-based methods such as Poisson Nearest Neighbor and K-Ripley's statistic, could provide additional insight into ways in which our length scale compares to other metrics. Our goal for this work, however, was to find a length scale based on the area between vents that would represent the same characteristic across multiple volcanic fields. This characteristic is the maximum length at which clustering occurs before transitioning to random behavior. We compared our Voronoi derived bandwidths with Silverman's bandwidth because, while simplistic, the latter is a measure based on distance between vents that provided a useful comparator for our area-based measure. Importantly, our focus is describing clustering behavior of vents in existing fields without reference to future activity.

2.5.4.3 Limitations of Current Data

While data on the clustering and alignment of volcanic vents is important for understanding the structure of volcanic fields, there are limits to analysis based on the data available. First is the question of how to define a vent, as illustrated by our datasets. In the AVF, vents are allocated by edifice, even where those edifices may have been constructed by more than one eruption, and may include more than one vent (Bebbington and Cronin, 2011). In the SVF, the question of 'vents or events' has been posed, given that multiple vents can be assigned to the same eruptive product (e.g., a lava flow) and vice versa, with multiple distinct products associated with one vent (Condit

et al., 1996). If the same classification were used for the AVF, then Rangitoto, for example, would have multiple vents, one associated with each new lava flow and the highest density region of the resulting KDE would skew toward the shield (Linnell et al., 2016). The Central and Washington segments of the Cascades have both numerous shields and composite centers with associated basaltic vents (i.e., Three Sisters, Mount Adams). Here the question is whether cinder cones represent single events or are part of a composite eruption; answering this question requires a combination of location, age, and composition data that does not exist for most fields. Particularly important are age data that allow analysis of temporal, in addition to spatial, clustering behaviors. Where such data are unavailable, the analysis of topography (e.g., O’Hara et al., 2020) may help answer the question of whether edifices represent single or composite events.

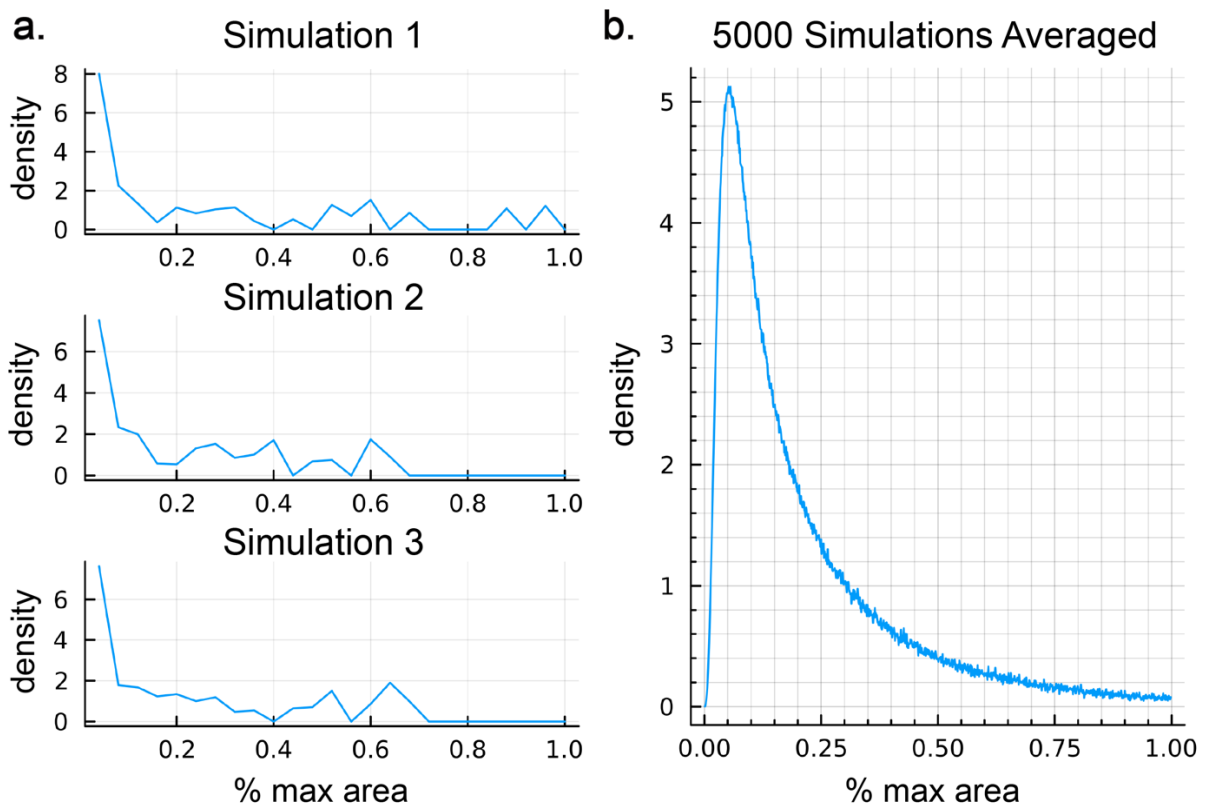


Figure 2.15. (a) Three PDFs for simulated normally distributed scattered vents. While there is a relatively constant mass for x-values less than 0.4, we see a large variance in how the mass manifests in the tails of the simulations. (b) The averaged PDF of 5,000 simulations.

Another limitation relates to the larger question of how to designate volcanic fields (Canon-Tapia, 2016; Deligne et al., 2016). Discrete fields can be defined using a convex hull connecting the outermost vents (Le Corvec et al., 2013b; Fig. 2.2), the widest isocontour of a KDE (Germa et al., 2013), or a geometric shape. An example of the latter is the AVF, which has a well-defined boundary that has been approximated as an ellipse (Bebington, 2015). The Cascade volcanic arc and its segments, in contrast, contain cinder cones that are dispersed among not only shield volcanoes, but also domes and stratovolcanoes; the result is a near continuous field that shifts between focused and distributed volcanism across various segments (Hildreth, 2007; O’Hara et al., 2020). Including all vent types in our analysis would allow us to further explore relations between focused and distributed volcanism in space and time. Ultimately, these data could be extended to assess the nature of the underlying magmatic system.

2.6 Conclusions

We have explored some of the current statistical methods used to characterize volcanic fields and developed a methodology for identifying volcanic fields that have an intrinsic length scale that signifies the transition from clustering to random behavior. We do this by comparing the distribution of area between vents, as depicted in Voronoi diagrams for each volcanic field, with the distribution of areas generated by a random Poisson process. All but one examined field, the Auckland Volcanic Field, have clustering length scales which vary in size. We also use Silverman’s rule to calculate a simple distance-based length scale for each field. For the Springerville Volcanic Field and cinder cones of the Central Cascades, the Voronoi (area-based) length scale is half the value of the Silverman’s (distance based) length scale. The shields of the Central Cascades, however, have a Silverman’s length scale more than three times the Voronoi

length scale, while both the cinder cones and shields of the Washington Cascades have similar Silverman and Voronoi length scales.

Both length scales provide bandwidths for Kernel Density Estimation (KDE) to produce maps that visualize patterns of vent density. For Auckland and Springerville volcanic fields, KDE_{Sil} highlights linear features that reflect regional tectonic forces. The smaller KDE_{Vor} for Springerville, in contrast, shows smaller clusters that could reflect locations of magma storage. Contrasting clustering behavior of cinder cones and shield volcanoes through time, particularly in the Washington Cascades, suggests an increase in magma focusing in the Middle Pleistocene that appears consistent with growth of stratovolcanoes. In the central Cascades, in contrast, temporally persistent volcanism, both cinder cones and shield volcanoes, at Three Sisters and Crater Lake may indicate places along the subduction zone that promote magma ascent; indeed, these are both locations where major fault systems intersect the Cascades.

Future extensions of this work include further statistical analysis, addition of more data, and physics-based modeling of clustering. Our work focuses on where and at what length scales in volcanic fields the pattern of vents departs from random behavior and begins to address causes for such departures. Comparison of bandwidth selection methods could help to identify key comparator distributions other than Poisson. Additional data could better distinguish between vents and events and identify the relative importance of tectonic and magmatic drivers. Variations in edifice volume, and by extension magma supply rate, could extend Voronoi and KDE analysis if properly weighted. Improving spatial coverage of geochemistry and age data would allow analysis of the role of crustal storage on distributed volcanism in arc settings like the Cascades. Finally, modeling crustal processes, including both magma storage dynamics and tectonic faulting, could help to constrain controls of temporal changes in vent location and magma composition. As

an initial step, this work shows that it is possible to derive intrinsic length scales at which clustering occurs and what these length scales mean across each field, which should lead to general tools for assessing structure in distributed volcanic fields.

2.7 Acknowledgements

We would like to thank Chuck Connor as well as two anonymous reviewers for their feedback on our original submission. We thank Chris Condit and Marissa Mnich for providing us with the vent location, age, cluster, and composition data for the Springerville Volcanic Field and for providing suggestions and feedback during the project, and Dan O’Hara for sharing the updated Cascade Volcanic Arc vent dataset.

2.8 Data and Code Availability

The original datasets used for this analysis, as well as Kernel Density raster images are available at the following Github (https://github.com/rcbussard/Length_Scale_Data). Codes used for calculating Voronoi mesh and diagrams as well as volcanic field CDFs and PDFs can be found at the following Github (https://github.com/charperflow/voronoi_clipped). Figures were made with MATLAB 2020, ArcGIS, and Julia, and then compiled with Adobe Illustrator.

2.9 Bridge

This chapter has focused on mapping distributed volcanic fields with statistical methods that are able to characterize clustering in these fields to begin addressing questions of magma storage and ascent in these areas. The methods presented in this chapter can be used to compare volcanic fields and address questions of magma storage and field evolution when other methods of individual sampling or monitoring might not be as affective. The next two chapters focus on using a different technique of monitoring on focused volcanic systems to show how monitoring can be affected. The next chapter will focus on how monitoring efforts can be affected by a

volcano's environment and the extent of change between sensors in monitoring. Chapter IV will then focus on monitoring at a different focused center in the Cascades, Medicine Lake, and how subsurface processes can be explored with monitoring data.

2.10 Supporting Information

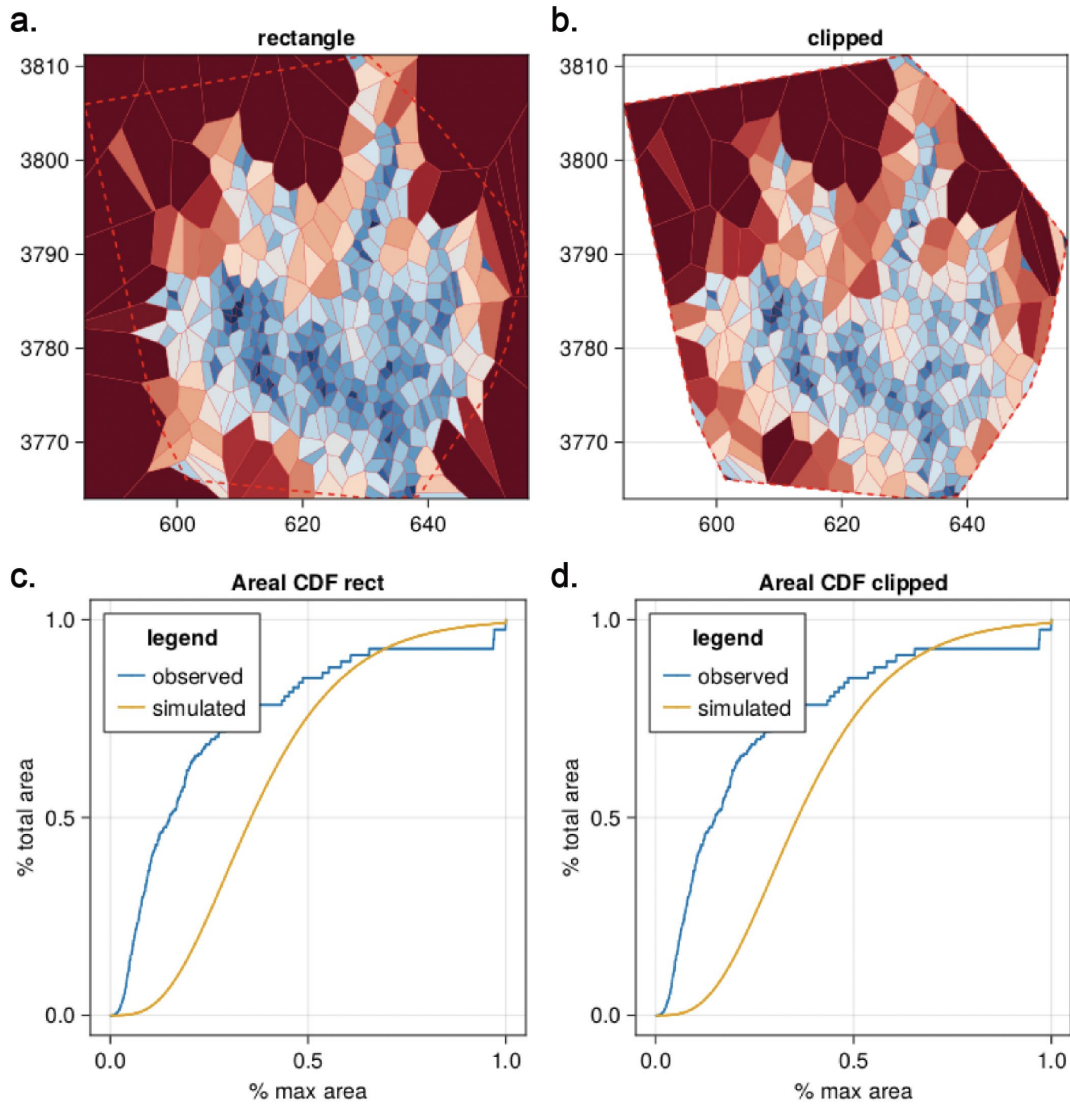


Figure 2.S1. Voronoi diagrams for Springerville Volcanic Field colored by residuals for the (a) rectangular and (b) convex hull boundaries. CDF plots for the SVF cell areas for the (c) rectangular and (d) convex hull boundaries.

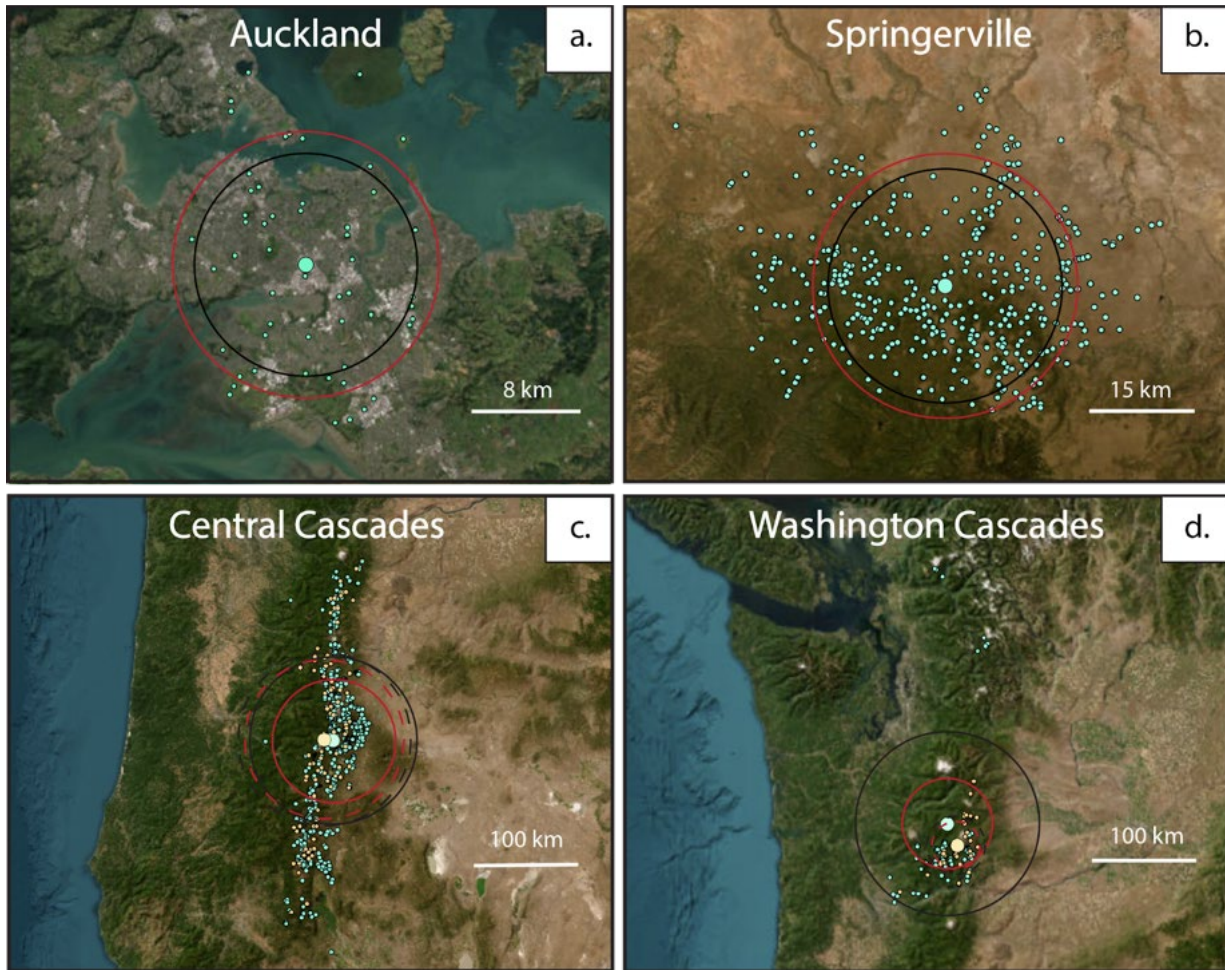


Figure 2.S2. Mean center (large blue/orange circle), standard distance (red) and median distance (black) for the (a) AVF, (b) SVF, (c) Central Cascades segment, and (d) Washington Cascades segment.

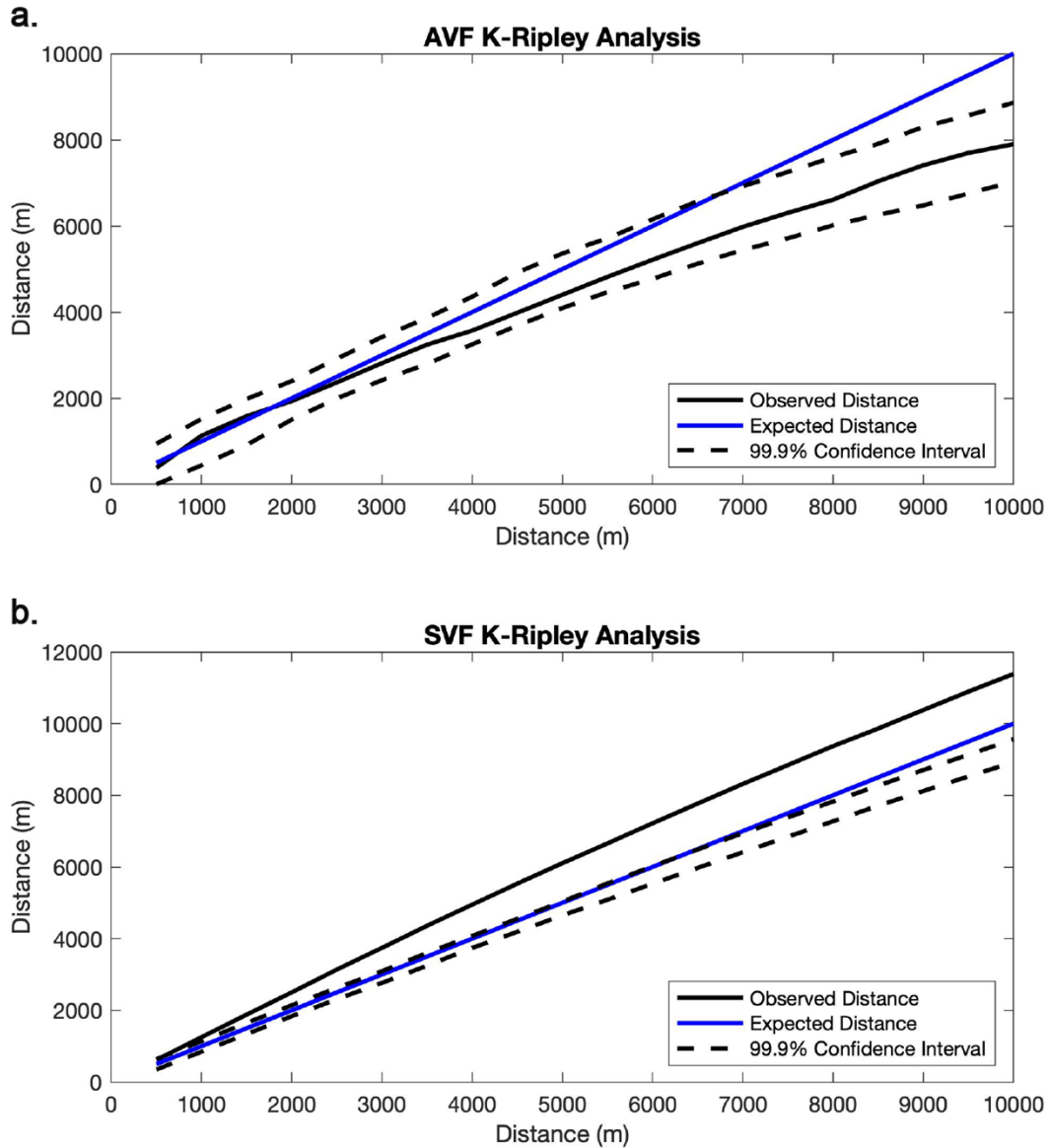


Figure 2.S3. Plots showing the expected value, observed value, and 99.9% confidence interval for the (a) AVF and (b) SVF.

Volcanic Field of Interest	R Value
Springerville Volcanic Field	0.9460
Central Cascades Cinder Cones	0.4921
Central Cascades Shields	1.0005
Washington Cascades Cinder Cones	0.4338
Washington Cascades Shields	0.939

Table 2.S1. Table listing calculated R-values for Poisson Nearest Neighbor (PNN) analysis for each of the clustered fields.

CHAPTER III

QUANTIFYING THE EFFECTS OF VOLCANO SNOW COVER ON INSAR COHERENCE USING A COMPUTATIONALLY INEXPENSIVE NEURAL NETWORK

This chapter contains co-authored material and is in preparation to be submitted for publication. The writing of this chapter was done solely by me with co-authors Josef Dufek, Christelle Wauthier, and Meredith Townsend providing editorial assistance. I conceptualized the work presented in this chapter and performed all analyses.

3.1 Introduction

Over the last half century, remote sensing has become a vital tool for monitoring volcanoes because it improves our ability to detect unrest, monitor active volcanic hazards, and track decadal processes at volcanic systems (e.g., Poland & de Zeeuw-van Dalssen, 2021). One remote sensing method that is often used for tracking ground deformation in response to processes such as dike propagation, magma chamber volume change, and flank instability is Interferometric Synthetic Aperture Radar (InSAR) (Anderson et al., 2019; Dzurisin et al., 2006; Gonzalez-Santana et al., 2022). SAR satellites, both airborne and spaceborne, emit radar waves that travel through the Earth's atmosphere, reflect off of the ground surface, and return back carrying both amplitude and phase information (Rosen et al., 2000; Bürgmann et al., 2000; Massonnet et al., 1993). When a SAR satellite images the same area multiple times, the phase information from one acquisition date can be differenced from the phase information from another date to create an interferogram (the process of interferometry) to show movement of the Earth's surface. While the use of radar

waves allows SAR satellites to image the Earth's surface regardless of time of day or cloud cover, the coherence (quality of signal) between two SAR images can still be impacted by a variety of factors: atmospheric effects (Williams et al., 1998; Lohman & Simons, 2005; Stephens et al., 2020), high magnitude ground deformation happening within a short period of time, or land cover changes such as vegetation and snow. While some radar bands can penetrate vegetation cover to retrieve signal, snow cover impacts coherence for all radar bands because the placement, melting, and refreezing of snow changes radar wave scattering properties of the ground between satellite acquisitions (Zebker & Villasenor, 1992; Zebker et al., 2007). Given the number of volcanoes that are high enough to experience persistent partial or total snow cover, coherence loss from snow can present challenges to volcano monitoring (Kumar & Venkataraman, 2011). A tool that efficiently and systematically identifies snow cover across volcanic systems and tracks the spatial extent of snow cover through time would enable quantification of seasonal signal decorrelation and where across the region decorrelation would be expected. Knowing this would provide guidance to network construction for interferogram stacking and help determine if InSAR is an applicable tool for the area of interest.

Machine Learning (ML) has emerged as an efficient means of image classification in a number of disciplines including process of identifying and categorizing pixels in an image based on certain identifying information (Lary et al., 2016). Classification can either be supervised, where classes for grouping pixels are known and defined, or unsupervised, where pixels are grouped into clusters based on statistical properties (Maxwell et al., 2018; Duda & Canty, 2010). One type of supervised ML used for image classification is a neural network which is designed to mimic the connection networks in brains and is therefore composed of layers of neurons that are all connected to each other (Lary et al., 2016; Maxwell et al., 2018). These connections are

assigned weights, random at first, but change with repeated iterations; weight combinations that improve the classification ability of the network are used for successive classifications (Sun et al., 2020; Zhou, 2020; Taye, 2023).

In this work we develop a neural network trained on Landsat-8 imagery and test if the network can accurately detect snow cover, and quantify the effects of snow cover on InSAR signal coherence across Mount St. Helens using snow cover prediction outputs from the neural network. We test the accuracy of our computationally inexpensive neural network trained to classify snow cover by comparing its output predictions to Normalized Differenced Snow Index (NDSI) images of the same area, to assess whether pixels with higher NDSI values correspond to higher snow prediction values. We quantify snow cover through time over three chosen areas in the region surrounding Mount St. Helens that have different land cover characteristics, and then measure changes in InSAR coherence of these areas across different seasons. Finally, we simulate ground inflation due to a point source at depth and mask the deformation with snow cover from dates with high and low snow cover to understand how much ground deformation signal is potentially lost to incoherence from snow cover at Mt. St. Helens throughout the year.

3.2 Geologic Setting

Mount St. Helens is a composite stratovolcano located in southwestern Washington along the northern stretch of the U.S. Cascade Volcanic Arc. The volcano's flank collapse and subsequent explosive eruption in 1980, as well as renewed activity from 2004-2008, have encouraged both remote and in situ observation to prepare for future hazards (Criswell, 1987; Christiansen et al., 1981; Sherrod et al., 2008). InSAR is one remote method that was used to study ground deformation occurring prior to and during the 2004-2008 renewed activity, finding volcano-wide co-eruptive deflation centered on Mt. St. Helens' summit crater (Poland & Lu,

2008). In addition to this deflation, InSAR spanning pre-eruptive and co-eruptive periods of the 2004-2008 activity located several regions of subsidence within the pumice plain emplaced in 1980 to the north of the volcano. However it can be difficult to retrieve deformation signal at Mt. St. Helens, because forested land surrounds the volcano, the region experiences heavy precipitation for much of the year (Dzurisin et al., 2008; Poland & Lu, 2008), and the volcano plus its surrounding area are often partially or fully snow covered.

3.3 Methods

For this work, we use an InSAR dataset composed of 151 descending Sentinel-1 SAR scenes (Track 115) processed using the topsStack workflow from the ISCE2 software to create 730 interferograms spanning 2014-2020 (Rosen et al., 2012) (Fig. 3.S1a). The interferograms as well as their companion coherence maps were loaded into MintPy (Yunjun et al., 2019) and geocoded using a 30 m SRTM DEM (Farr & Kobrik 2000). The optical dataset consists of 30 Landsat 8 (Path 46 Row 28) images (30 m resolution) with less than 5% of cloud cover (Fig. 3.1a) spanning 2014-2021. These images were downloaded using Google Earth Engine in addition to the 2016 National Land Cover Database (NLCD), a product developed by the U.S. Geologic Survey and the Multi-Resolution Land Characteristics (MRLC) Consortium that classifies the entire contiguous U.S., Alaska, and Hawaii into various land cover types at 30 m resolution using a combination of satellite and field data (Jin et al., 2019). Once downloaded, the NLCD product is cropped to cover the same area as the Landsat 8 images and then used to create a label file for the neural network by assigning a value of one to whole pixels labeled as perennial ice/snow and by assigning a value of zero to pixels with all other labels.

In addition to the label file from the NLCD, the neural network needs training data. Of the 30 available Landsat scenes, the scene from September 13th 2016 was chosen as the training dataset

because of the lack of cloud cover and the availability of an image from the same year as the NLCD, which reduced variability between the data and the label file. Pixel values from bands 2-7 (spanning optical, near infrared, and short wave infrared wavelengths) for the training image are randomly split into training (60%), validation (20%), and testing (20%) subsets. The training dataset is used to help the model learn patterns in the dataset, the validation data are used to evaluate model performance during the training, and the testing data are used after the model is trained to provide an unbiased performance evaluation of the model. The 60-20-20 split used for this neural network has been used in previous studies (e.g., Wu et al., 2013). For this dataset the split produces enough data to both train and test the model without overfitting.

The architecture of the neural network is kept simple to optimize computational time, consisting of an input layer, a hidden layer, and an output layer. The input layer contains six nodes; one node for each of the six bands being read into the neural network. For the hidden layer, the number of nodes can be set by the user but should be placed at a value to minimize model loss (error of the model). For this neural network setup, a hidden layer with twenty nodes results in the least amount of loss (Fig. 3.S2a). In addition to node amount, the hidden layer needs an activation function; activation functions help train the neural network by producing outputs that describe the complex relationships in the data. The ReLU activation function is a piecewise linear function that outputs the value from a node if the value is greater than zero, and outputs zero if the value is less than zero. ReLU was selected because it promotes computational efficiency (Ide & Kurita, 2017). We chose the softmax activation function to transform the raw output from the hidden layer into vectors of probabilities (in this case probability of snow presence) for the output layer of the neural network (Dunne & Campbell, 1997). Two nodes were needed for the output layer: the first node

outputs a value per pixel representing the probability of snow being present, and the second outputs a value per pixel stating the probability of snow not being present.

Three epochs (training cycles) were selected for the neural network, as this allowed the loss to be repeatedly minimized without overtraining (Fig. 3.S2b) (Maxwell et al., 2018). When the trained neural network was run on the testing data, it produced an accuracy of 99%, a P-score of 0.943, and an R-score of 0.199 (Fig. 3.S3). For neural networks, the P-score represents the precision of the model while the R-score represents model sensitivity. While it is preferable to have high values for both P and R scores to minimize the number of Type I errors (false positives) and Type II errors (false negatives), the low amount of snow pixels resulting from a label file describing land cover over Mt. St. Helens in September makes it difficult to achieve a high R-score during training. Therefore each snow prediction image was compared with a Normalized Difference Snow Index (NDSI) image produced with the Landsat 8 images (Fig. 3.1b). NDSI images are calculated using the following ratio:

$$NDSI = \frac{(Band\ 3 - Band\ 6)}{(Band\ 3 + Band\ 6)}$$

In this ratio, values greater than zero typically indicate presence of snow cover. There is no singular value for NDSI that determines the presence of snow, as values ranging from 0.3-0.8 have been used as the threshold for identifying glaciers with accuracies of 75-96% (Singh et al., 2021, Zhang et al., 2019). There are also methods such as the Difference Snow Index (DSI) and Ratio Snow Index (RSI) that have similar success with classifying snow (Lin et al., 2012). For the purposes of this work, comparing NDSI and snow prediction values from the neural network provides one option of an external metric beyond the confusion matrix to test how the neural network performs.

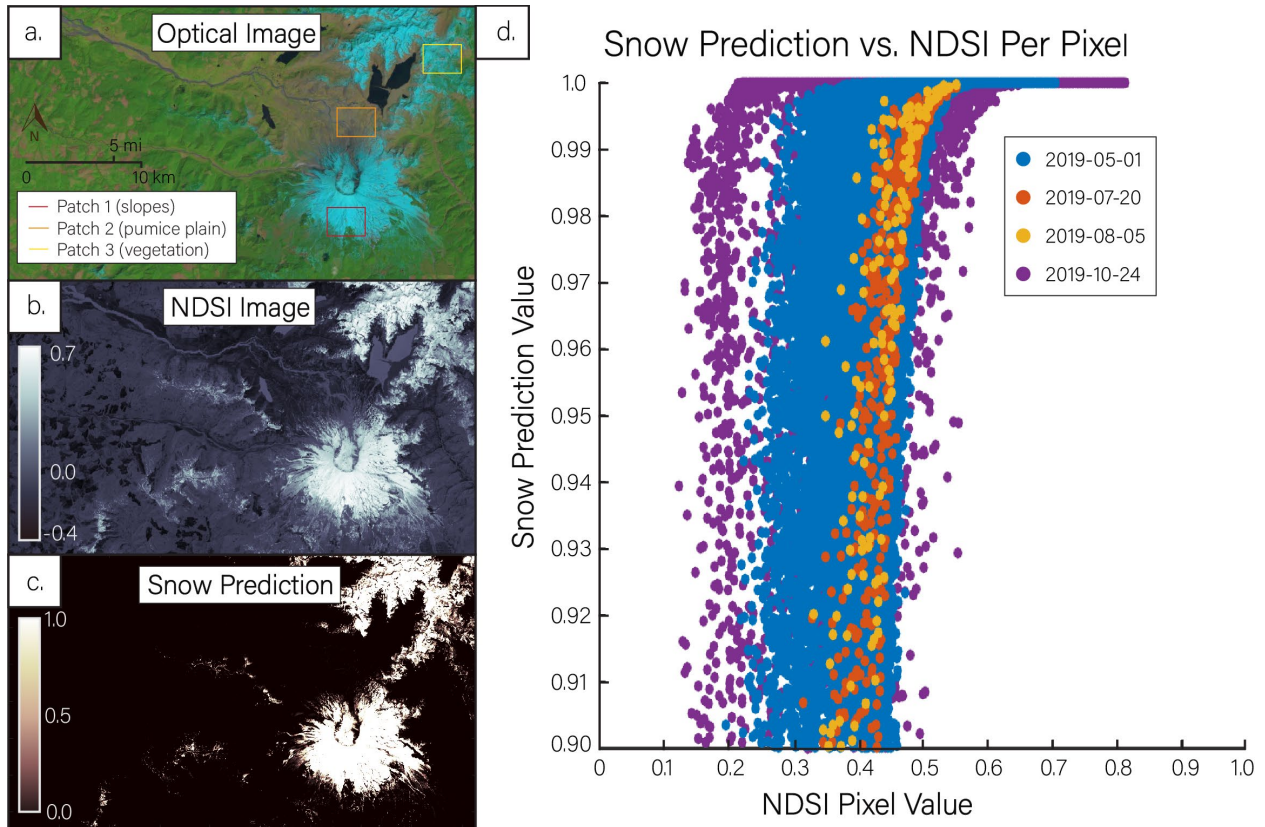


Figure 3.1. Optical image with natural color band combination (a), Normalized Differenced Snow Index (NDSI) image (b), and snow prediction image output (c) for the Landsat 8 scene collected May 1st, 2019. (d) Scatter plot of NDSI and Snow Prediction % values > 0.9 for corresponding pixels for four dates across 2019, including 2019-05-01. Patches used for yearly snow cover tracking are annotated with colored boxes in (a).

3.4 Results

The snow prediction images produce regions of high snow prediction values (> 0.9) with pixels of lower prediction values along the edges of these regions (Fig. 3.1c). When comparing the NDSI value against the snow prediction value for each pixel across the 29 dates, we find that generally as NDSI values increase, snow prediction values increase (Fig. 3.S4). Dates from 2019, which span a range of months and seasons, all have high prediction values that correspond with positive NDSI (Fig. 3.1d). One way in which the neural network outperforms NDSI is through a clearer distinction between Spirit Lake and the surrounding snow. While the NDSI image for May 1st 2019 (Fig. 3.1b) shows positive values for the surface of the lake, the snow prediction data for

the same date shows a prediction of zero for the lake and a value near one for nearby snow (Fig 3.1c). Instances of high snow prediction values at negative NDSI values are due to isolated clouds in the images. As these clouds did not cover the study areas focused on in this work (Fig. 3.1a), these dates were retained for subsequent analysis. To produce snow masks for each image, we use pixels with snow prediction values > 0.9 because this will produce a confident conservative estimate for snow cover in each image.

With the generated snow masks, we calculate the percent of pixels with snow cover for three areas of interest across the twenty-nine dates spanning 2014-2021 (Fig. 3.2a-c). The first area of interest, referenced hereafter as patch 1, covers the southern slopes of Mt. St. Helens, and the second area, patch 2, contains pixels across the pumice plain (Fig. 3.1a). The third area, patch 3, covers an area of vegetated ridgeline to the northeast of Mt. St. Helens. This patch was chosen to see how snow cover over vegetated areas impacts coherence; patch 1 and 2 are bare rock when there is no snow. For Patch 1, there is almost always a non-zero amount of snow cover, which is to be expected given the high elevation. During the winter season, snow cover of Patch 1 stays consistently over 80%, while the spring and fall months show snow cover ranging anywhere from 20-60%. Even during the summer months snow cover stays above zero, in contrast to the pumice plain that usually fluctuates between $> 80\%$ snow cover from December through March and $< 20\%$ snow cover for the rest of the year (Fig. 3.2a; Fig. 3.2b). Patch 3 typically shows snow cover values between the two end members of patches 1 and 2. Similar to patch 1, patch 3 retains non-zero snow cover into the spring months, but at a lower percent.

The temporal resolution of the Sentinel-1 data is twelve days, while for the Landsat data it is sixteen days, so the satellites do not image the same area on the same day most of the time. Therefore to directly compare the InSAR and optical datasets, we chose dates that are close enough

together in time (imaged 1-3 days apart) to ensure that snow cover doesn't change dramatically and that the snow prediction images are still accurate. InSAR coherence maps are associated with both a reference and secondary date; for this work we chose coherence maps whose reference dates were close in time to the optical dates as having even one date with snow cover impacts coherence.

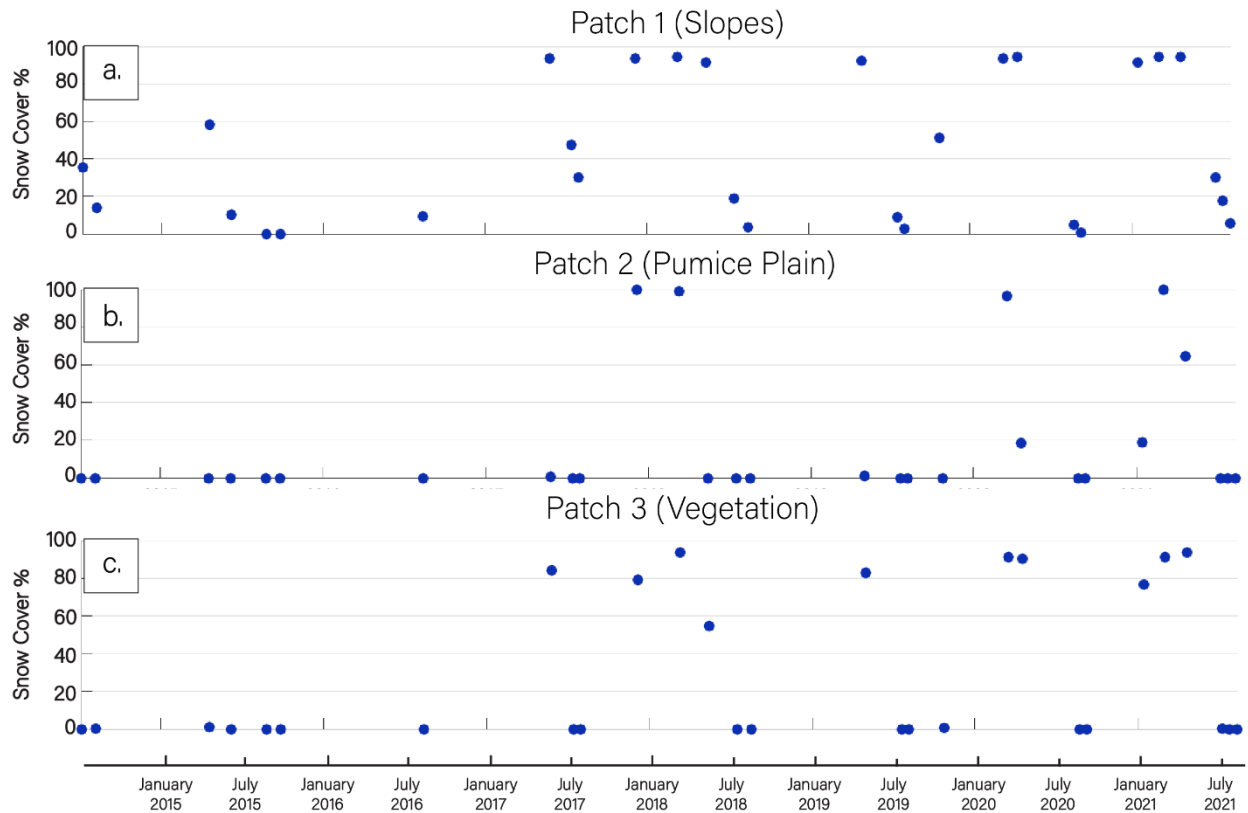


Figure 3.2. Time series spanning 2014-2020 showing the percent of pixels covered with snow for the three designated patches on (a) the southern slopes of Mt. St. Helens, (b) the pumice plain, and (c) a vegetated region to the east of Spirit Lake.

Figure 3.3 shows four date pairs that fit within this range and are also from four different seasons of the year. These provide a representative view of snow cover and coherence over time at Mt. St. Helens. The December 5th 2017 snow mask shows snow cover across Mt. St. Helens, the pumice plain, and the ridges to the north (Fig. 3.3a). Coherence for the interferogram with the December 2nd 2017 reference date is high across the Toutle River deposits, in addition to some areas to the west. Snow cover stays widespread for the March 11th 2018 snow mask, with the coherence image for the March 8th 2018 InSAR reference date showing similar high value patches

to the west and North Fork Toutle River but no areas of high coherence across the snow-covered regions (Fig. 3.3b). The May 1st 2019 snow mask and coherence image with the May 2nd 2019 reference date clearly highlight the effect snow cover has on coherence; the high coherence across the pumice plain terminates right where snow cover on the northern edge of the volcano begins (Fig. 3.3c). The last pair from August 2020 shows only a small amount of snow cover close to the summit of Mt. St. Helens with high coherence across the slopes and pumice plain (Fig. 3.3d).

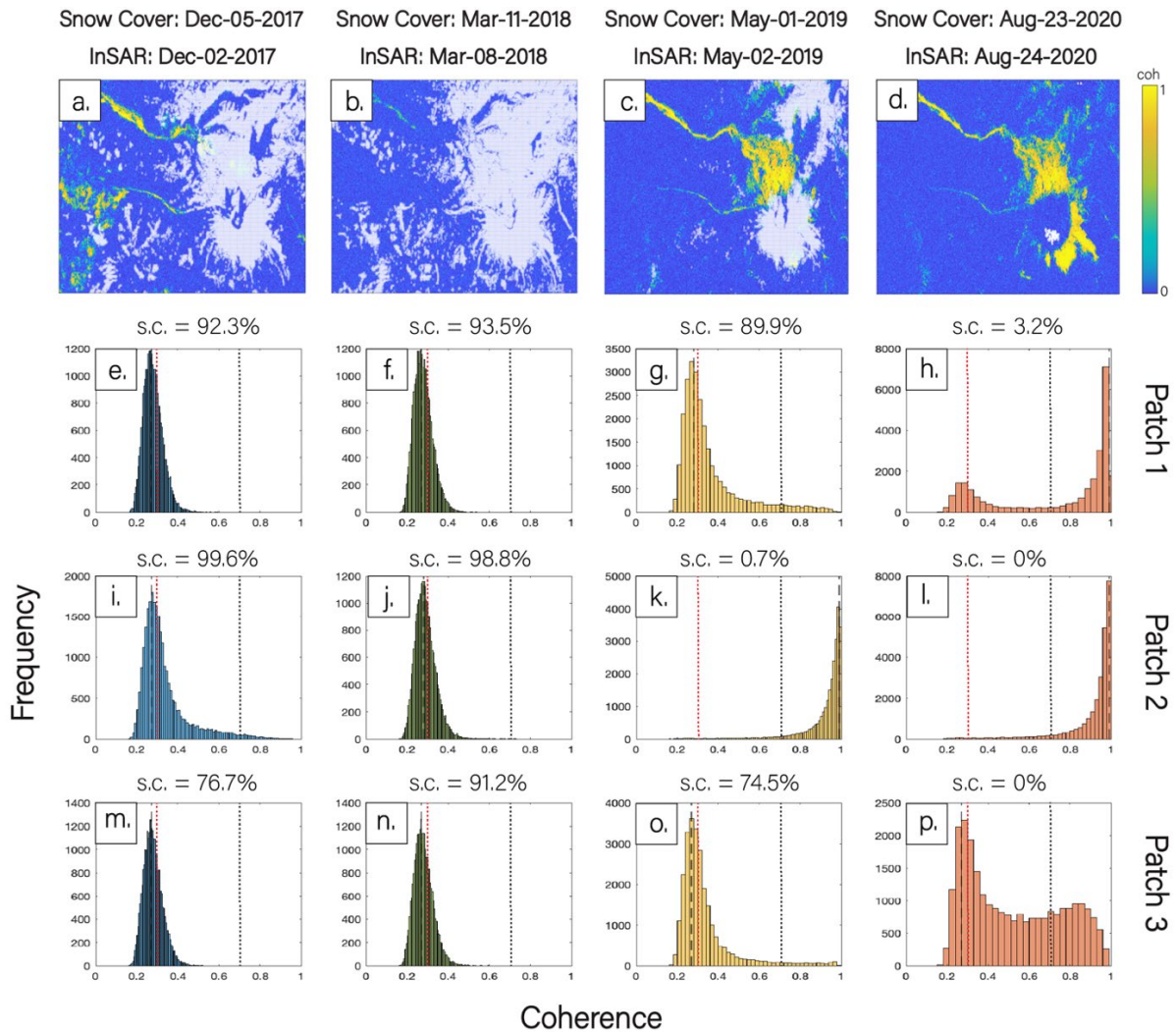


Figure 3.3. Snow cover masks paired with corresponding InSAR coherence maps (a-d). Frequency of coherence values for Patch 1 (e-h), Patch 2 (i-l), and Patch 3 (m-p) for five InSAR coherence maps with the chosen reference dates. Red and black dashed lines in each histogram represent coherence values of 0.3 and 0.7 respectively.

To measure the effect of snow on coherence, we plot the frequency of coherence values from five coherence maps associated with the four chosen InSAR reference dates (December 2nd 2017, March 8th, 2018, May 2nd, 2019, and August 24th, 2020) across the three patches of interest (Fig. 3.3e-p). Each coherence map are is generated from pairs with temporal baselines of twelve, twenty-four, thirty-six, forty-eight, and sixty-four days to minimize coherence loss from surface change across long time periods. These histograms show that coherence values significantly increase when there is no snow cover. Patch 2 specifically highlights this, with the peak frequency of its coherence values jumping from 0.28 to 0.99 when snow cover is not present (both the May and August dates; Fig. 3.3k-l). A similar trend can be seen in patch 1 for the August date (Fig. 3.3h), although there are still pixels with low coherence values, likely from a small amount of snow still present toward the summit of the volcano. As expected, Patch 3 does not experience a swing to high coherence values when snow is not present, because vegetation cover alone can degrade coherence. It is worth noting, however, that Patch 3 does have more high coherence pixels when it is isn't snow-covered (Fig. 3.3p). Patch 1 also shows an increase in variation of coherence for the May date as values on the tail of the frequency distribution reach values approaching one (Fig. 3.3g).

3.5 Discussion

The efficacy of InSAR for measuring volcano deformation relies on the ability to maintain coherence between the reference and secondary date. This analysis has shown that snow-cover has a significant impact on coherence. For this reason, selecting dates from June through September, when snow cover is zero or close to zero across most of the region, is likely to produce the most coherent pairs (barring significant artifacts from weather or other significant surface change). There is no certainty, however, that future magmatic activity and unrest at Mount St. Helens will

be confined to the months June-September; the 2004-2008 eruption included large ash and steam plumes in October, March, and December when there is usually snow cover across the volcano's slopes (Fig. 3.2a).

To explore how much deformation signal from an inflation event could be lost from coherence degradation in interferograms, we model a point source in a homogeneous elastic half-space (Mogi, 1958) centered beneath Mt. St. Helens at a depth of 10 km with a volume increase of 30 million m³ (Anderson & Segall, 2013). We then mask the vertical deformation from the inflation source with snow masks from March 11th 2018 and August 23rd 2020, as these dates represent two end members of snow cover at Mt. St. Helens. This allows us to replicate signal loss from coherence degradation (Fig. 3.4a-b). We focus on vertical deformation, as the typical Line of Sight (LOS) deformation retrieved by InSAR is often converted to vertical for geophysical analysis, and only one direction of horizontal motion (E-W) is easily retrievable from InSAR data (Bürgmann et al., 2000; Varugu & Amelung, 2021; Wicks et al., 2002). While snow cover doesn't always correspond to a total loss of phase signal, as seen in the high coherence areas located within the snow covered pumice plain in December 2017 (Fig. 3.3a), the stark boundary between snow cover and the high coherence pumice plain in May (Fig. 3.3c), as well as the general shifts in coherence values from close to or at 1.0 to ≤ 0.3 indicates that these snow masks could represent regions where the InSAR phase signal could not be retrieved due to snow cover. The March snow cover masks a large portion of the deformation and reduces the pattern to a ring of uplift around the volcano (Fig. 3.4a). Meanwhile, the August snow cover allows for almost the entire deformation pattern to be viewed (Fig. 3.4b).

We then test a range of source depths (5-15 km) and volume increases (10-60 million m³) to see how widespread snow cover similar in pattern to the March snow cover mask would affect

the visibility of these different scenarios. After modeling the deformation from each source, we count the number of pixels with centimeter scale ($> 1\text{cm}$) of deformation, if present, before and after applying the March 11th, 2018 snow mask. While there are cases where millimeter scale deformation indicate magmatic processes, deformation on a centimeter and greater threshold is often measured with InSAR during magmatic activity and is therefore used as the threshold in this work (Dzurisin et al., 2009; Sigmundsson et al., 2024; Varugu & Amelung, 2021). Across all combinations, the amount of viewable cm-scale deformation for the point source is reduced to less than 60% (Fig. 3.4c). At higher volume increases (30-60 million m^3), shallower sources show a greater reduction in cm-scale pixels, due to higher magnitude deformation being concentrated toward the center where snow cover is heaviest. At a volume increase of 25 million m^3 , sources of all depths have the same percentage of viewable cm-scale deformation at below 50%. For volume increases less than 25 million m^3 , greater depth sources have lower viewable pixel percentages, with some sources between 13-15 km depth having less than a third of cm-scale pixels viewable for the lowest modeled volume increase (10 million m^3 ; Fig. 3.4c). This substantial decrease in the amount of viewable cm-scale deformation during periods of widespread snow cover (as seen in December and March) indicates the potential difficulties for InSAR satellites to retrieve enough signal to detect, let alone characterize, magmatic activity at Mt. St. Helens during these periods.

These percent values are also likely high estimates as there are other causes of coherence loss at Mt. St. Helens such as atmospheric artifacts, topography, and vegetation. To characterize the effects of these causes on coherence in the future, this neural network framework could be adapted to include additional optical datasets such as Sentinel-2 to both increase the amount of images available for viewing snow cover at Mt. St. Helens and for increasing the amount of training data for the neural network. Additional adaptations to the neural network framework could

produce outputs that give the likelihood of multiple different land cover types (e.g. snow, clouds, deciduous vegetation, coniferous vegetation, etc.) simultaneously and compare coherence changes in response to each type throughout the year for an even more detailed understanding of viewing conditions for InSAR at Mt. St. Helens or other potential volcanoes of interest.

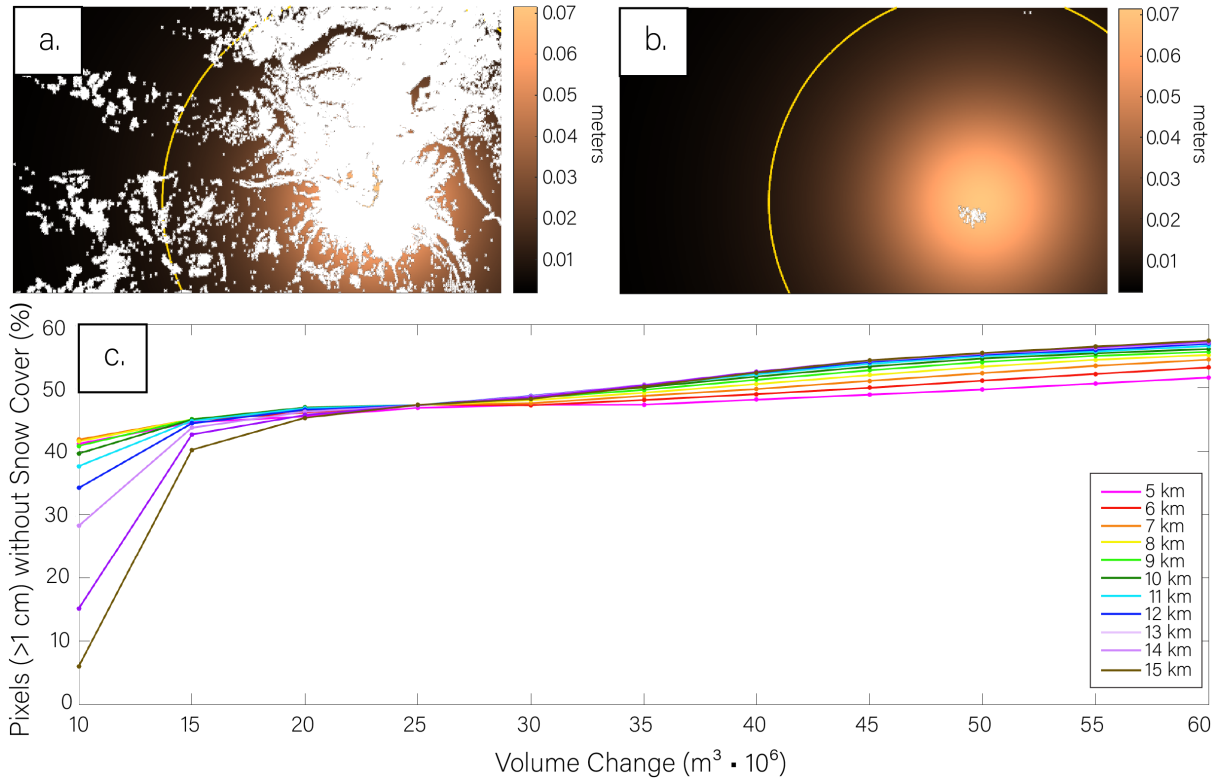


Figure 3.4. Maps of deformation from a Mogi point source at 10 km depth with a volume increase of 30 million m^3 masked with snow cover from 20180311 (a) and 20200823 (b). The yellow line in each map indicates the limit of centimeter scale deformation for this combination of source parameters. (c) Line plot shows the relation between inflation source depth and volume change with amount of centimeter scale deformation viewable when masked with snow cover from 20180311.

3.6 Conclusion

In this work we successfully classify snow cover with a computationally inexpensive neural network framework using Landsat 8 optical satellite imagery. We then compare snow cover at different patches across Mount St. Helens with InSAR coherence data and find that coherence over regions of bare rock (the slopes of Mount St. Helens and the pumice plain) can be reduced as drastically as 70%. Even in vegetated areas that already suffer from degraded coherence, snow

cover significantly decreases the amount of high coherence pixels available. Forward modeling an inflation event from a point source indicates that during periods of high snow cover at Mount St. Helens, the amount of centimeter scale deformation that could be viewed without significant coherence degradation is below 60% for magma reservoirs at a range of depths and volume increases, while deeper and lower volume inflation might be nearly completely hidden to InSAR by snow cover. The potential inability of InSAR to detect enough signal to discern deformation associated with processes that could lead to an eruptive event, or to have enough signal to accurately characterize the parameters associated with these processes, has significant monitoring implications for Mount St. Helens and other volcanic systems that experience persistent snow cover. While InSAR can be a useful tool for volcano monitoring on large spatial scales and detecting ground movement over time, additional remote (e.g. GNSS, thermal remote sensing) and ground based monitoring tools are recommended for volcanoes that lose regions of coherence to snow cover.

3.7 Acknowledgements

The research reported in this publication is supported by the University of Oregon (UO) and by NSF Grant EAR-1940994. Sentinel-1 data is provided by ESA/Copernicus and Landsat-8 data is provided through NASA. We would also like to thank Mike Poland, Tyler Paladino, and Sarah Cooley for useful discussions.

3.8 Data and Code Availability

Data from Landsat-8, the National Land Cover Database, and Sentinel-1 were used in the work described by this manuscript. Landsat-8 and NLCD data were downloaded through Google Earth Engine, and Sentinel-1 Single Look Complex (SLC) data was downloaded through the Alaska Satellite Facility Vertex Platform (<https://search.asf.alaska.edu/#/>). These SLC's were then

processed using the ISCE2 software developed by NASA (<https://github.com/isce-framework/isce2>). Figures were made with MATLAB 2020 and compiled with Adobe Illustrator. The neural network Python notebooks, snow cover prediction images (in GeoTIFF format), and MATLAB scripts are published on GitHub (<https://github.com/rcbussard/neuralnet-proj>).

3.9 Bridge

This chapter focused on using a neural network to better understand the challenge of coherence loss for InSAR data due to snow cover across Mt. St. Helens. Work done in this chapter can be used to help decide which seasons of the year radar acquisitions should be used to construct interferograms over volcanoes in environments like the Cascade Volcanic Arc. In addition, this chapter showed how snow cover can obscure potential indicators of magmatic activity. The final chapter utilizes InSAR data to update existing knowledge on ground deformation at Medicine Lake volcano as well as different modeling tools to determine causes of this deformation. Constraining the cause of deformation at Medicine Lake can help determine if there is any local hazard present and can better explore different processes at volcanic caldera complexes.

3.10 Supporting Information

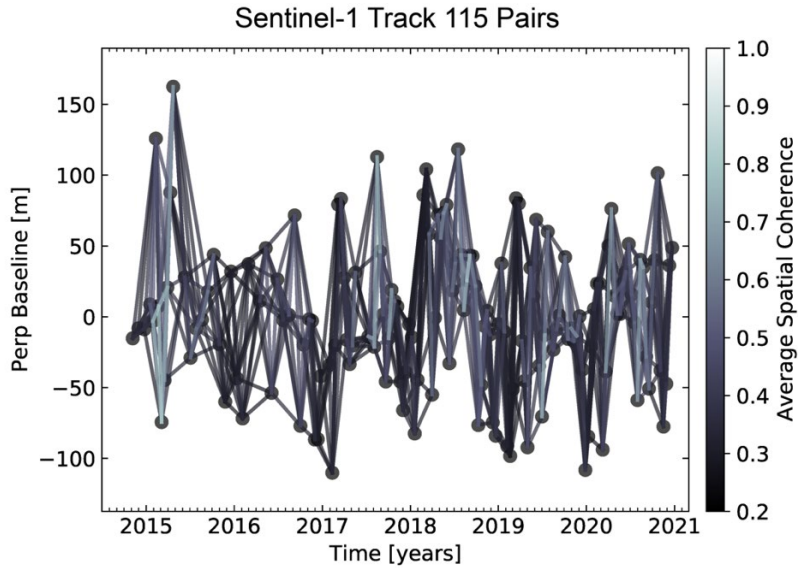


Figure 3.S1. Perpendicular baseline plot for Sentinel-1 Track 115 acquisition dates.

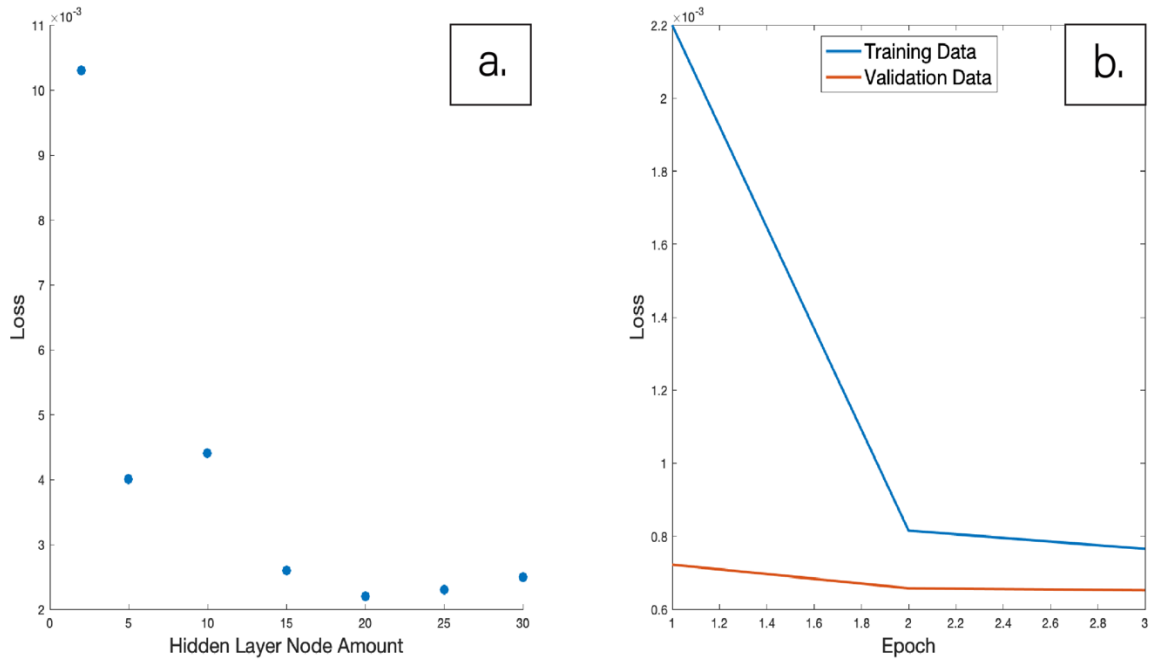


Figure 3.S2. (a) Loss as a function of node amount for the hidden layer of the neural network. While loss stays at the same magnitude for various node amounts, 20 nodes produces the lowest loss and was selected for usage with classifying data. (b) Loss as a function of epochs, with the most notable decrease in loss occurring at the second epoch and leveling out at the third epoch.

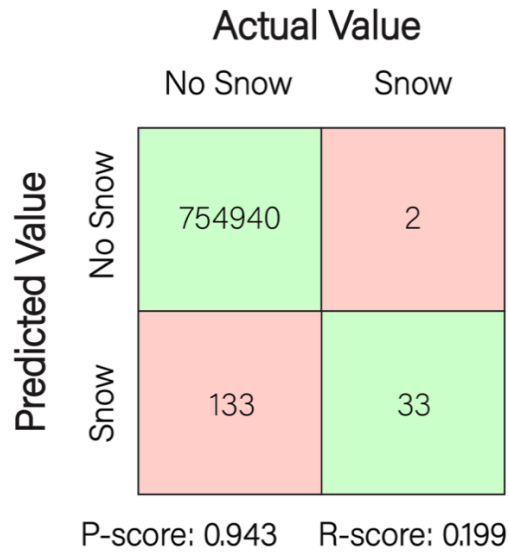


Figure 3.S3. Confusion matrix for test dataset snow prediction accuracy with P-score and R-scores listed.

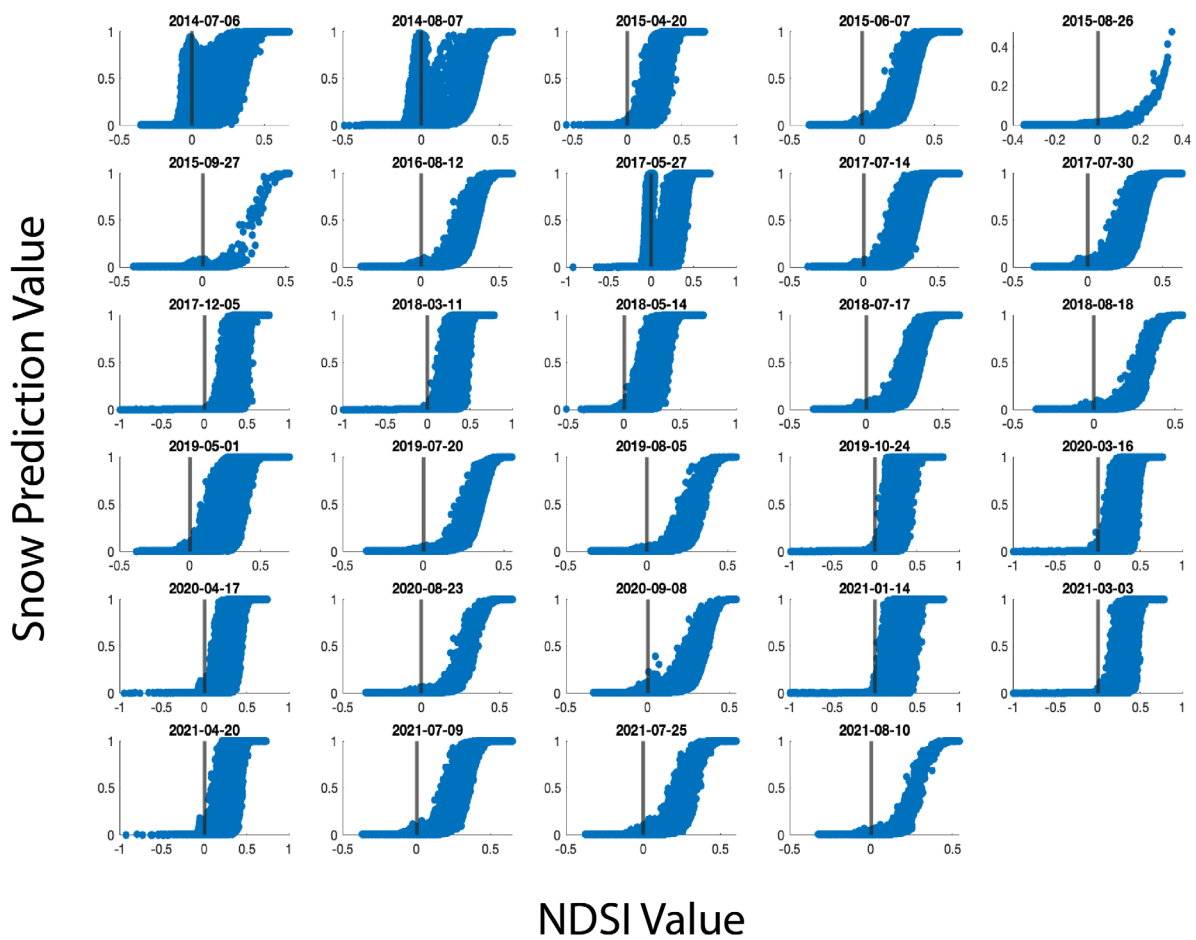


Figure 3.S4. NDSI values compared with snow prediction values for each pixel in the twenty-nine Landsat 8 acquisitions. A vertical line denoting the NDSI value of zero has been displayed for each image.

CHAPTER IV

INVESTIGATING SUBSIDENCE AT MEDICINE LAKE VOLCANO USING INSAR, GNSS, and MCMC MODELING

This chapter contains co-authored material and is in preparation to be submitted for publication. The writing of this chapter was done solely by me with co-authors Josef Dufek, Christelle Wauthier, and Meredith Townsend providing editorial assistance and helping conceptualize the work presented in this chapter. Codes for the MCMC model were provided by Meredith Townsend. I performed the analysis presented in this chapter.

4.1 Introduction

The ability to monitor volcanic systems is crucial for discerning magma storage region characteristics and their change over time, as well as measuring potential unrest that could precede an eruption. One type of volcanic unrest is ground deformation, the movement of the Earth's surface in response to a variety of processes occurring at or beneath the surface. At volcanoes, common types of deformation include broad uplift or subsidence reflecting an influx or outflux respectively of magma to/from a central chamber (Wicks et al., 2002; Henderson et al., 2017; Rodríguez-Molina et al., 2021), or coincident regions of uplift and subsidence indicating dikes transporting magma (Lungren et al., 2013; Varugu & Amelung, 2021). In some cases such as the 2018 Kilauea eruption, ground deformation was used to see change at both a central caldera and along the eastern flank (known as the East Rift Zone) where a conduit was also depressurizing (Roman & Lundgren, 2023).

Interferometric Synthetic Aperture Radar (InSAR) is one type of method for measuring ground deformation. Airborne and spaceborne SAR satellites image the Earth's surface using radar waves, which travel through the atmosphere, scatter off the Earth's surface, and return to the satellites; the phase and amplitude of the returning waves carry information about the surface (Rosen et al., 2000; Bürgmann et al., 2000; Massonnet et al., 1993). For InSAR, the phase of radar waves scattered off the same region of the surface on two different days (also referred to as acquisitions) is differenced to create an interferogram, and in ideal cases the interferogram describes how the ground has moved between those two dates. Realistically, there are often several corrections that need to be applied to interferograms that remove phase changes associated with the Earth's atmosphere and the topography of the region imaged. The strength of the InSAR signal can also be degraded by surface change such as vegetation and snow cover that scatters the radar waves before they reach the ground (Williams et al., 1998; Lohman & Simons, 2005). Even with these challenges however, InSAR is still a useful tool for monitoring volcanic systems, as it can map an entire region's deformation between acquisitions, as opposed to other deformation measuring methods such as Global Navigation Satellite System (GNSS) and tiltmeter stations that monitor ground change continuously at a single point (Anderson & Johanson, 2022; Wicks et al., 2002). Interferograms spanning January 2018-May 2018 and December 2017-June 2018 from the ALOS-2 satellite were used to track the aforementioned ground deformation during the Kilauea 2018 eruption, continuously covering a distance of hundreds of kilometers (Roman & Lundgren, 2023).

At volcanic caldera systems in general however, the link between deformation and eruption is still relatively unclear, as there have been numerous instances of deformation occurring at caldera systems without a following eruption (Biggs et al., 2014). This is partially due to the fact

that ground deformation shows net change of the surface, which could be from one or multiple interacting causes (some of which might not even be volcanic in origin; tectonic forces, groundwater, etc.). There are also volcanic surface processes, such as cooling and compaction of lava flows (Wittmann et al., 2017; Ebmeier et al., 2012; Purcell et al., 2022) as well as volcanic flank creep (Gonzalez-Santana et al., 2022; González et al., 2010). This can lead to a volcanic caldera system with a complex deformation signal that is difficult to assign one cause.

Such is the case for Medicine Lake volcano, located in northern California, U.S., at the southern extent and eastern edge of the Cascade Volcanic Arc (Fig. 4.1). While Medicine Lake's last eruption occurred $\sim 1\text{ka}$, the central caldera and broad edifice that make up Medicine Lake have experienced apparent constant subsidence since 1954, with peak subsidence rates occurring within the central caldera. Multiple previous works have mapped this subsidence with a variety of techniques (leveling, GNSS, InSAR) that each have their own coverage across Medicine Lake's broad edifice (Dzurisin et al., 2002; Poland et al., 2006; Parker et al., 2014). This work seeks to add to the geodetic record over Medicine Lake by processing Sentinel-1 InSAR data spanning 2017-2021 to produce time series and average velocity maps that span the caldera and edifice. We utilize techniques for maintaining InSAR signal strength and correcting for phase artifacts for data over the Medicine Lake region that experiences seasonal snow cover, widespread vegetation, and atmospheric changes. We then further explore causes of the subsidence at Medicine Lake by inverting for three volume loss sources using Markov Chain Monte Carlo (MCMC) modeling; a point source, a sill with constrained length and width (1 x 1 km), and a sill with unconstrained length and width. The best fitting (most likely) point source has a depth of 7.7 km and volume change of $-0.0013 \text{ km}^3/\text{yr}$, while the best fitting constrained and unconstrained sill sources have depths of 12.1 and 10.1 km and volume changes of $-0.0014 \text{ km}^3/\text{yr}$ and $-0.0016 \text{ km}^3/\text{yr}$

respectively. When loading is also considered as a contributing factor to the edifice-wide subsidence up to 1.5 mm/yr, the best fitting models for each volume loss source become shallower in depth and have lower volume changes.

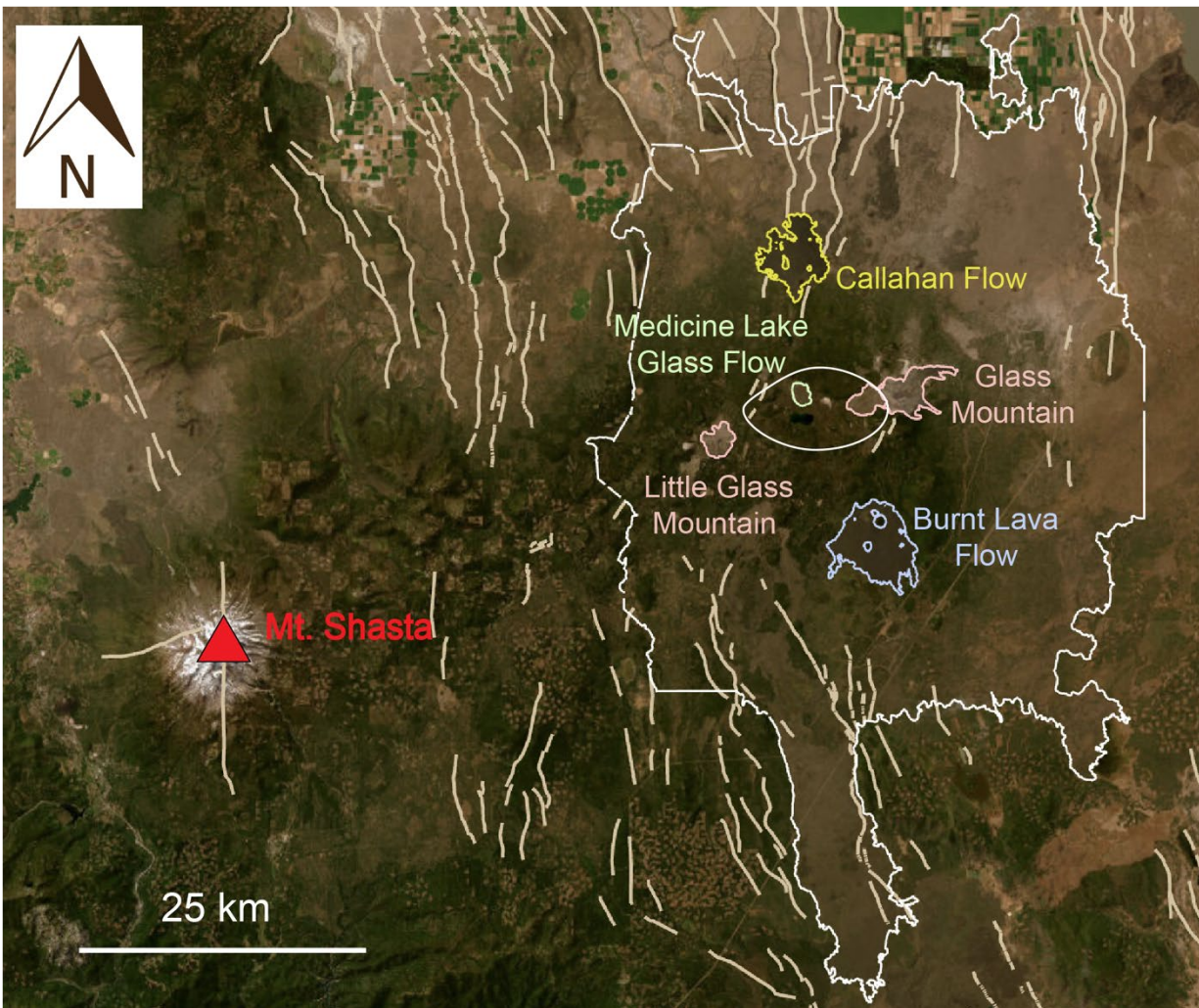


Figure 4.1. Map of region surrounding Medicine Lake. The extent of the broad edifice is highlighted in white, as well as the central caldera. Regional faults (tan) trend N-S and NW-SE and mostly curve around the edifice. Major Holocene erupted products (all younger than 5 ka) are highlighted by composition: basaltic andesite (yellow), andesite (blue), dacite (green), rhyolite (red).

4.2 Geologic Setting

Medicine Lake is a complex volcanic system covering an area of 2200 km² with broad shield-like slopes that steepen to a 7 x 12 km central caldera (Donnelly-Nolan et al., 2008). Its eruptive history spans the past 500 ka, erupting primarily basaltic and basaltic andesite magmas

on the far reaches of the edifice with more evolved dacitic and rhyolitic products typically occurring around or within the central caldera (Fig. 4.1; Anderson, 1941; Donnelly-Nolan & Lanphere, 2005; Donnelly-Nolan et al., 1991; Champion & Donnelly-Nolan, 1994). The last eruption at Medicine Lake was ~ 1 ka and produced the rhyolitic Glass Mountain flow on the eastern edge of the caldera that runs down the eastern slopes. While Medicine Lake lies east of the main axis of the Cascade Volcanic Arc at the intersection of the Klamath Graben and Walker Lane fault zone (Grose et al., 1989; Hildreth, 2007), the volcano has erupted subduction-related magmas (Donnelly-Nolan et al., 2008; Magna et al., 2006; Kinzler et al., 2000), indicating its connection to the volcanic arc. There is also evidence of extensional tectonics from the neighboring Basin and Range province in the form of N-S trending open ground cracks around the edifice (Fig. 4.1). There was little recorded seismic activity at Medicine Lake until August 1st 1978 when a M 4.6 earthquake was located midway between Mt. Shasta and Medicine Lake, followed by hundreds of shallow $M \geq 2$ earthquakes over the next 24 hours (Cramer, 1978; Bennet et al., 1979). Another seismic swarm began on September 29, 1988, consisting of shallow (within 2 km of the surface), primarily $M \leq 3$ earthquakes located beneath the caldera (Dzurisin et al., 1991; Walter & Dzurisin, 1989). This seismicity carried into the following year, retaining the same characteristics except for a small cluster in April 1989 at depths 3-4 km and a long period M 2.7 earthquake that occurred 15 km beneath the western edge of the caldera on December 1st, 1989. Since that swarm, seismicity has remained primarily beneath the caldera with most events occurring at depths shallower than 10 km. Geothermal drilling revealed a high temperature geothermal system (~ 300 °C) (Hulen & Lutz, 1999; Bargar, 2001) and an intrusive body > 6 km in diameter beneath the caldera (Donnelly-Nolan, 2006; Lowenstern et al., 2003) that is also evident in gravity (Finn & Williams, 1982), seismic refraction (Zucca et al., 1986; Fuis et al., 1987), magnetotelluric (Stanley et al., 1990), and

tomography (Evans & Zucca, 1988; Chiarabba et al., 1995; Ritter & Evans, 1997) data. Seismic tomography studies have also identified a small silicic magma body beneath the eastern part of the caldera, located at 3-7 km depths with a volume of $\sim 10 \text{ km}^3$.

4.2.1 Edifice Deformation

Several studies across Medicine Lake that have revealed past and ongoing deformation across the edifice and within the central caldera. Initial leveling surveys in 1954, 1988, and 1989, spanning a 193 km path around Medicine Lake and Mt. Shasta, revealed that the summit had subsided as much as $302 \pm 30 \text{ mm}$ over that time period, marking a steady subsidence rate of $8.6 \pm 0.9 \text{ mm/yr}$ in the center of the caldera and broad radially decreasing subsidence across the rest of the edifice (Fig. 4.2; Dzurisin et al., 1991; Dzurisin et al., 2002). Interferometric Synthetic Aperture Radar (InSAR) data collected by ERS-1/2 satellites that spanned 1993-2000 also measured radially symmetric subsidence across the caldera with a line of sight rate of 10 mm/yr (Poland et al., 2006). Campaign GPS vertical velocity data from a station located in the center of the caldera in 1996, 1999, 2003, and 2004 matched this rate at 11 mm/yr (Fig. 4.2). Additional InSAR data from Envisat and ALOS satellites spanning 2004-2011 also measured subsidence rates of $\sim 10 \text{ mm/yr}$ in the central caldera (Parker et al., 2014).

While there is general agreement between datasets on the central caldera subsidence rate, other aspects of the signal make modeling and therefore constraining the process causing the subsidence challenging. When the elevation data alone was initially inverted to find the parameters of a potential source of the subsidence (termed volume loss source for the remainder of this work to match previous terminology; Dzurisin et al., 2002, Poland et al., 2006, Parker et al., 2014), a best fit point source (Mogi, 1958) of depth 10 km and volume change $-0.0031 \text{ km}^3/\text{yr}$ and a best

fit sill (Okada, 1985) of depth 11 km and volume change $-0.002 \text{ km}^3/\text{yr}$ were found with both located under the southern part of the caldera (Dzurisin et al., 2002).

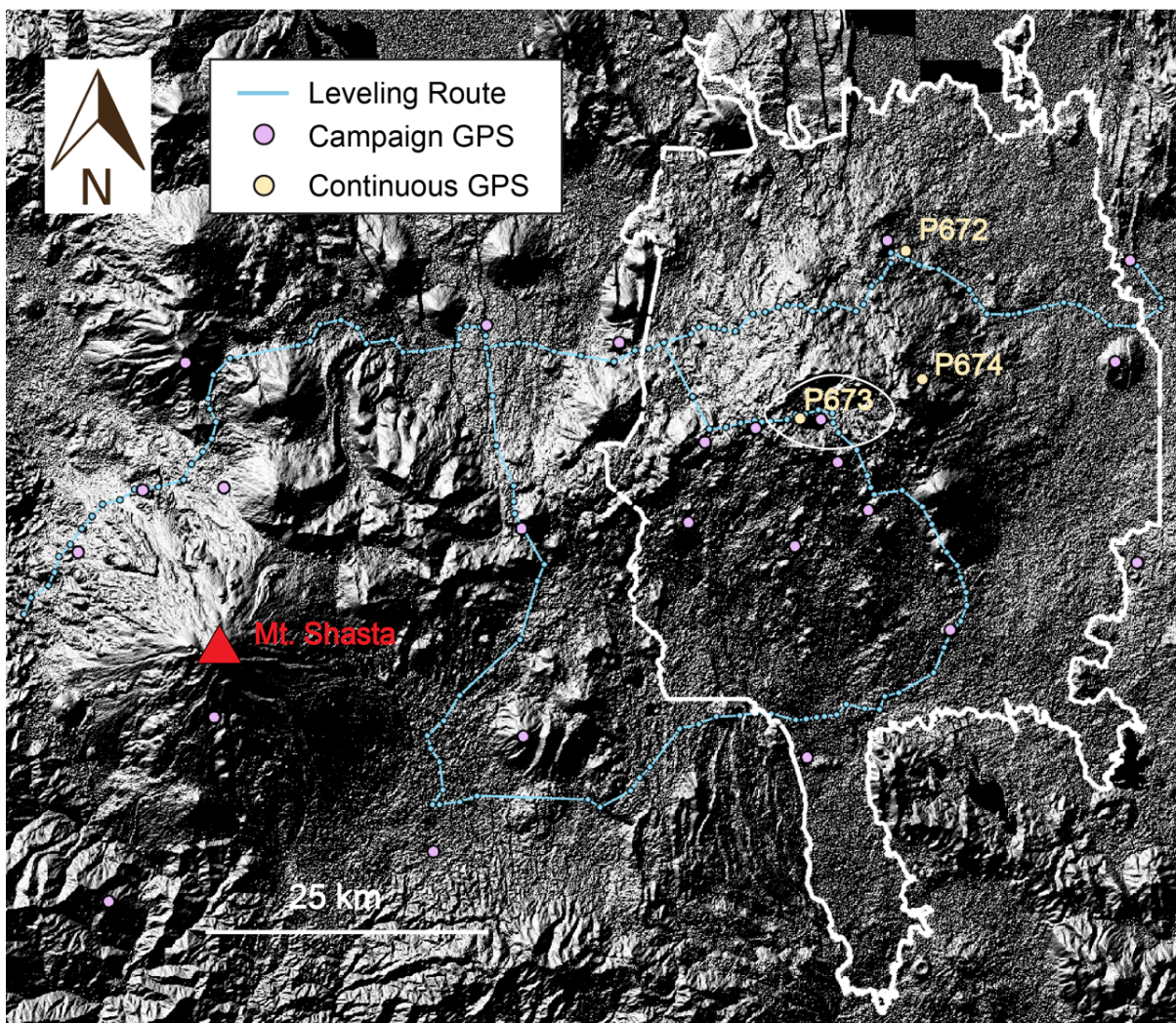


Figure 4.2. Hillshade map of region surrounding Medicine Lake. The extent of the broad edifice is highlighted in white, as well as the central caldera. Mt Shasta to the southwest labeled with red triangle. Leveling route from Dzurisin et al., 2002 (blue), campaign GPS from Poland et al., 2006 (purple), and present continuous GPS stations labeled.

However, volume loss was believed to play a minor role in producing the deformation; the subsidence was thought to be a combination of gravitational loading of the 600 km^3 edifice (Donnelly-Nolan et al., 2008) and intrusive rocks on the crust below and thinning of locally weakened crust by Basin and Range extension. Inverse modeling of just the campaign GPS data put potential volume loss sources at 6 and 5 km for point and sill sources respectively, both of

which poorly replicate the 1954-1989 leveling data (Poland et al., 2006). In addition, the GPS horizontal velocity data showed radial inward deformation was only present at stations within 10 km of the caldera instead of broadly across the edifice, further disfavoring the major influence of a local volume loss source on the deformation.

Subsidence due to thermal contraction of a larger scale cooling body was investigated by modeling thermal contraction of a hot (800 °C) cylindrical volume that runs vertically from 4 km below the volcano to the base of the crust (Poland et al., 2006). Cooling of this hot cylindrical volume alone can match vertical deformation rate and pattern, but overestimates horizontal deformation rates. A surface load model of a point source on a thin weak shell representing Medicine Lake on a thermally weakened crust matches the pattern of vertical deformation but is not expected to produce the magnitude measured (Poland et al., 2006; Brothie & Silvester, 1969; Brothie 1971; Dzurisin et al., 1991). The improved coverage of the Envisat and ALOS InSAR data was used to further reinvestigate volume loss sources, with a best fit point source at 6.2 km depth with a volume change of $-0.0012 \text{ km}^3/\text{yr}$ and a best fit sill source at depth 9.2 km with a volume change of $-0.0012 \text{ km}^3/\text{yr}$ (Parker et al., 2014).

4.3 Methods

To create the InSAR timeseries over Medicine Lake, 131 ascending (Track 137) and 139 descending (Track 115) acquisitions were downloaded, along with a 30 meter Digital Elevation Model covering the region from the Shuttle Radar Topography Mission (SRTM) (Farr & Kobrik, 2000). The acquisitions were processed with the InSAR Scientific Computing Environment (ISCE2) stackSentinel workflow to produce wrapped and unwrapped interferograms for each acquisition pair as well as coherence maps (Rosen et al., 2012). These outputs were then loaded

into the Miami InSAR Time-series software in Python (MintPy) for post processing (Yunjun et al., 2019).

4.3.1 Network Modification and Post-Processing

Medicine Lake poses several challenges for obtaining strong InSAR signal. While the region to the north is bare rock, which is ideal for maintaining coherence, the caldera, slopes, and southern extent are covered by vegetation (Fig. 4.1). This vegetation can be difficult for the C-band radar waves used by Sentinel-1 to penetrate, causing random scattering and resulting in coherence loss (Chen et al., 2021). The only non-vegetated patches near the caldera are the flows from different eruptions, which produce small areas of higher coherence. These patches, however, experience prolonged snow cover due to their higher elevation relative to surrounding ground. The Medicine Lake region also experiences long periods of rainfall and cloud cover through the fall into spring, producing atmospheric phase delays that impact InSAR signal.

Due to these factors, we implemented Small Baseline Subset (SBAS) with a perpendicular baseline limit of 300 meters and a temporal baseline limit of 180 days. The network of interferograms is not altered in any other way (Fig. 4.3a-b). We inverted for the timeseries, correcting for topography and removing a linear phase ramp to isolate the subsidence signal (Fattahi & Amelung, 2013). We then manually inspected the interferograms for any significant noise or artifacts and excluded these interferograms; we then reran the inversion with the same baseline limits. After the new inversion, we compared the Root Mean Square (RMS) of residual phase for each date in the first and second inversion. Residual phase includes noise due to residual tropospheric effects, ionospheric turbulence, and remaining decorrelation. If the excluded interferograms reduced the RMS residual phase associated with their acquisition date by > 1 mm, then the interferograms remained excluded; otherwise they were returned to the network. Dates

that had RMS residual phase > 1 cm for both inversions were removed from the network entirely. The resulting networks (Fig. 4.3c-d) contain fewer interferograms than the original networks but the average RMS residual phase is reduced in both cases. These final networks were used for a third inversion; in addition to deramping and correcting for topography, tropospheric corrections were also performed using an empirical height model and ERA5 weather model implemented through PyAPS (Doin et al., 2009; Jolivet et al., 2011). These tropospheric corrections vary in utility between regions and in some cases introduce more noise (Stephens et al., 2021), which is why both methods were tested in addition to no tropospheric correction. The resulting geocoded average velocity maps for 2017-2021 with each tropospheric correction are shown in Figure 4.S1, with low coherence pixels masked out. There are no dramatic differences between the velocity maps, so we compare the time-series data with data from continuous GPS stations to determine which correction method to choose (Fig. 4.4).

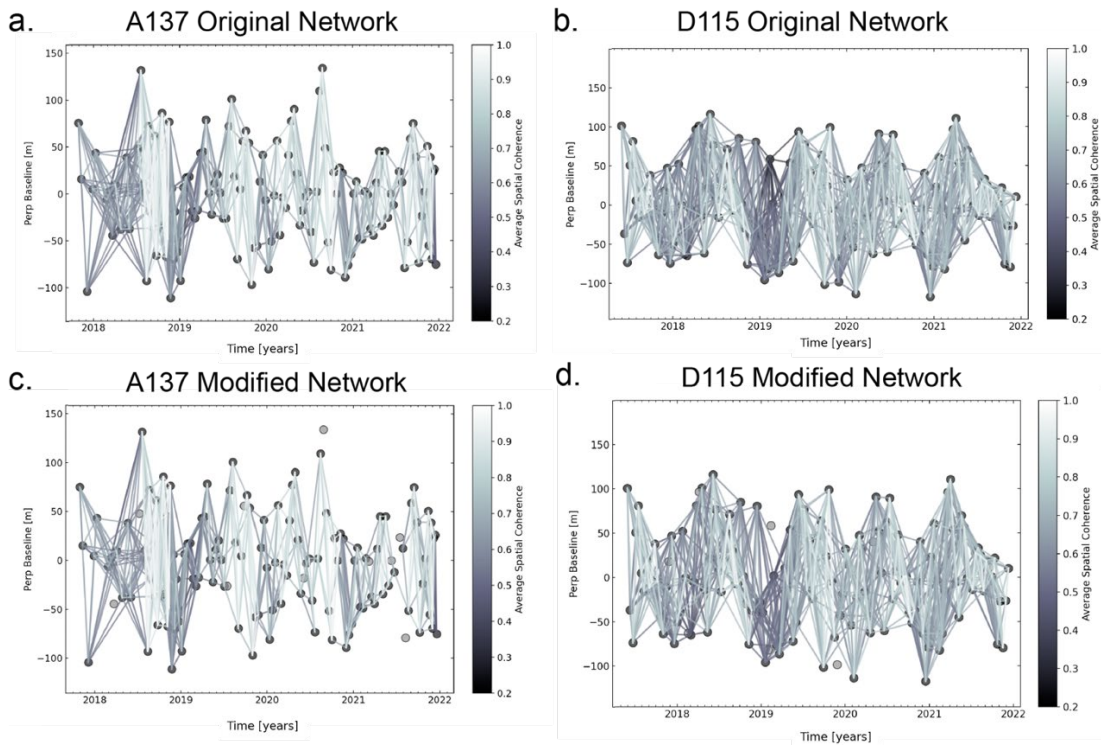


Figure 4.3. Perpendicular baseline plots for Track 137 Ascending original (a) and modified (c) networks as well as Track 115 Descending original (b) and modified (d) networks. Each point represents an acquisition date and each connection between points represents one interferogram (colored by average spatial coherence).

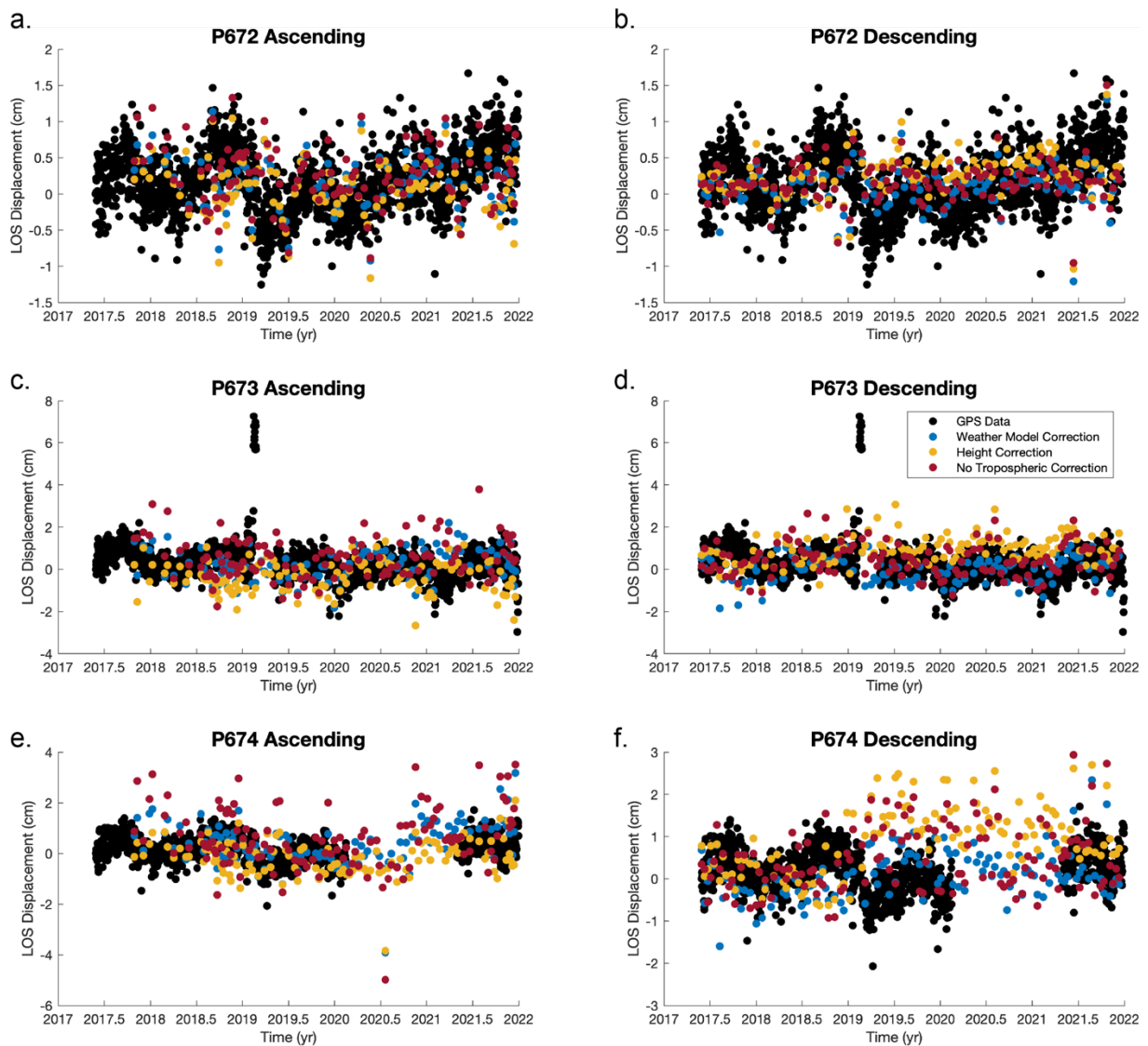


Figure 4.4. Timeseries data for ascending (a,c,e) and descending (b,d,f) InSAR data at continuous GPS stations at Medicine Lake.

There are three continuous GPS stations located within the edifice of Medicine Lake (Fig. 4.2); data from each of these sites was downloaded and projected into line of sight displacement to compare with the timeseries from different tropospheric corrections (Fig. 4.4). All three time series fit far field site P672 well with little variation. There is also little variation between corrections at P673 (located in the center of the caldera) for both the ascending and descending data. However, P674 sees the most noise in the InSAR timeseries and greatest difference in

correction methods; the station is located on the eastern slope of Medicine Lake where coherence is degraded due to a combination of snow cover in winter months, steep topography, and vegetation cover and the station has data missing from early 2020 into 2021. Generally, it appears the weather model correction timeseries provides the best fit across all stations for both ascending and descending data and is selected as the dataset to use for further analysis.

The corrected timeseries has a few acquisitions per station that do not match the GPS data regardless of correction used. There are two main instances of this: for the descending data at GPS station P672, the timeseries data in June 2021 are considerably offset from the GPS data (Fig. 4.4b), while the second instance occurs for the ascending data at date July 2020 for P674 (Fig. 4.4e). However, these dates do not have deformation data that diverge from GPS data at all stations, so we keep these in the timeseries inversion. Beyond these instances, the InSAR timeseries data and error for the weather model data fits well with the GPS data (Fig. 4.S2).

4.4 Results

4.4.1 Velocity Data

The ascending and descending datasets corrected with the weather model are then subset with MintPy to an area viewed by both modes and combined into one vertical velocity map (Fig. 4.5a). While MintPy provides E-W velocity maps, only vertical velocity is used as the horizontal data is noisier. Across the northern and eastern portions of the edifice, where coherence is stronger, there is broad subsidence on the order of 1-7 mm/yr. Velocity transects across the edifice show that the subsidence rate increases linearly from the edge of the caldera towards the center; the peak value of the subsidence sits at ~ 1.4 cm/yr (Fig. 4.5b-d). The E-W velocity transect (Fig. 4.4b) also shows small rates of uplift on each side of the caldera before returning to subsidence on the outer extent of the transect. On the edifice's eastern side, there is a region of subsidence that has been

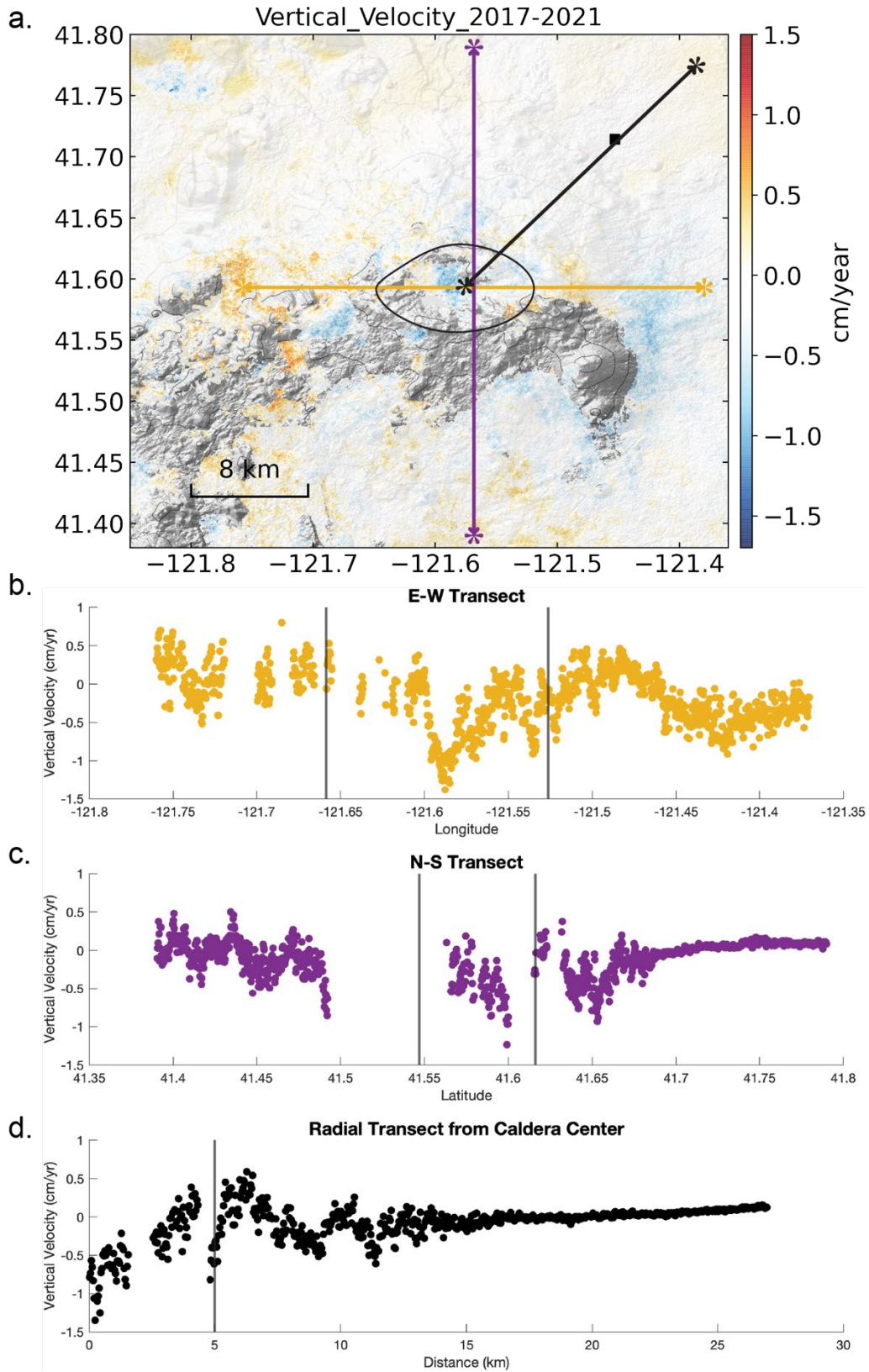


Figure 4.5. (a) Vertical velocity map over Medicine Lake, with east-west transect (b), north-south transect (c) and radial transect (d) extents marked.

previously measured with InSAR (Parker et al., 2014). It is difficult to constrain how long this subsidence has existed, as the original leveling route did not cover this region nor did any of the campaign GPS stations (Dzurisin et al., 2002; Poland et al., 2006). The N-S velocity transect (Fig. 4.4c) has most of its southern portion removed due to low coherence but still shows subsidence increasing closer to and within the caldera. The radial transect (Fig. 4.5d) shows the subsidence extending out to the northeast approximately 25 km from the caldera center.

4.4.2 MCMC Model Setup

To model potential sources of the deformation, the vertical velocity data is downsampled by a factor of ~ 10 as the data covers a large region, removing pixel columns on the west edge of the velocity map to exclude agricultural fields with high subsidence readings. This downsampled velocity data is then used to solve for a volume loss source using a Markov Chain Monte Carlo (MCMC) model in a Bayesian framework, as described in Townsend & Huang (2022).

We use two analytic source models - a point source in a homogenous elastic half space (Mogi, 1958) and a sill-like intrusion (Okada, 1985) - as both have been used in previous studies. For the point source model, we vary the depth, volume change, center latitude and center longitude of the source and assume a Poisson's ratio of 0.25. We model deformation from the point source using the following equation:

$$z = \frac{(1 - \nu)\Delta V}{\pi} \frac{d}{(r^2 + d^2)^{3/2}} \quad (1)$$

In this setup, ν is Poisson's ratio, ΔV is volume change, d is depth, and r is radial distance. For the sill-like intrusion, we model two different scenarios based on past results. The first scenario retains the length and width of the sill-like intrusion at 1000 meters (Parker et al., 2014), which allows the model to vary the depth, strike, opening, center latitude, and center longitude of the sill. The second

scenario allows the length and width of the sill to vary (Dzurisin et al., 2002; Poland et al., 2006) in addition to the previous parameters of scenario one. We use the rectangular sill code package from dMODELS to model the deformation (Battaglia et al., 2013), with bounds reported in Table 4.1 below; each run has 50,000 iterations split into five chains of 10,000 iterations.

Point Source Bounds		
	Lower Bound	Upper Bound
Depth (m)	3,000	15,000
Volume Change (km ³ /yr)	-0.01	0.00001
Center Latitude	41.50	41.625
Center Longitude	-121.65	-121.4
Sill Source Scenario 1 Bounds (length = 1km, width = 1km)		
	Lower Bound	Upper Bound
Depth (m)	3,000	15,000
Strike	180	360
Opening (m/yr)	-1.5	-.01
Center Latitude	41.50	41.625
Center Longitude	-121.65	-121.4
Sill Source Scenario 2 Bounds		
	Lower Bound	Upper Bound
Depth (m)	3,000	15,000
Strike	180	360
Opening (m/yr)	-1.5	-.01
Center Latitude	41.50	41.625
Center Longitude	-121.65	-121.4
Length (m)	9,000	20,000
Width (m)	4,000	10,000

Table 4.1. Upper and lower bounds for each variable parameter in point and sill source scenario 1 and 2 inversions.

4.4.3 MCMC Model Results

The results for the point source inversion show a primary relationship between source depth and volume change, with no visible trends in location and depth or volume change (Fig. 4.S3). The mean depth ($7.9 \pm .8$ km) sits between the depths found for modeled point sources in previous studies (shallower than the source modeled for leveling data and deeper than the source for GNSS and InSAR data), while the mean rate of volume change ($-0.0013 \pm .0001$ km³/yr) matches previous estimates from GNSS and InSAR (Parker et al., 2014). The model that produces the best fit (minimizes the residual vector and produces the greatest likelihood) is a point source at 7.7 km

depth and $-0.0013 \text{ km}^3/\text{yr}$ volume change centered at 41.5366° , -121.4421° (Fig. 4.6). These coordinates center the volume loss source to the east of the caldera, notably where the southeast subsidence patch sits. When running the MCMC inversion, after a short burn-in period, each of the chains converge quickly, with chains 1 and 5 converging slightly before chains 2,3, and 4 (Fig. 4.6e).

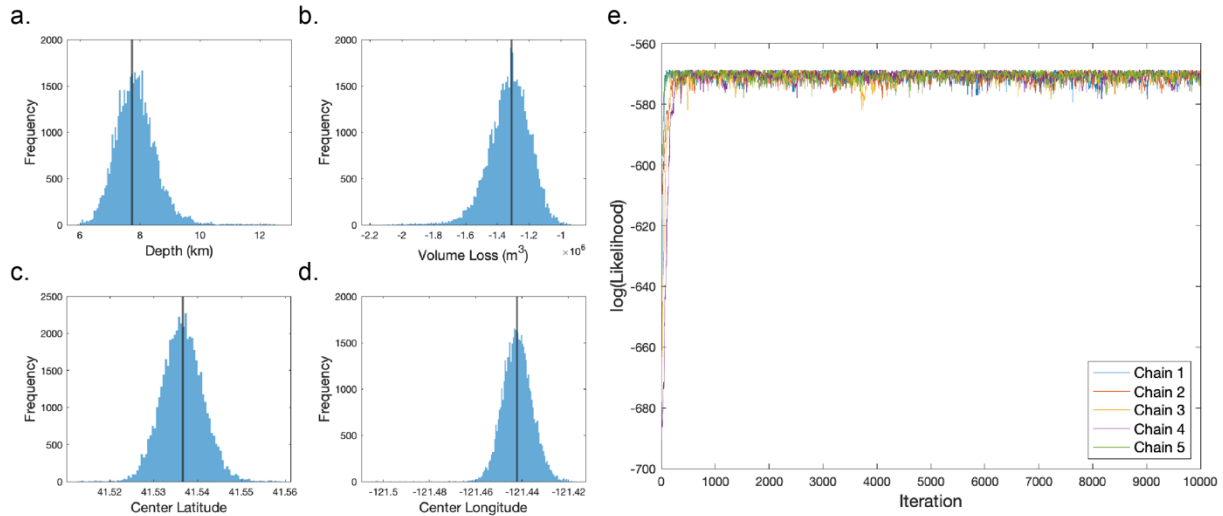


Figure 4.6. Distribution of depths (a), volume loss (b), center latitude (c), and center longitude (d) accepted guesses for MCMC point source model. Note that the burn in values (first 100 iterations of each chain) have been removed from the distributions for easier visualization of distribution shape. Black vertical line on each plot indicates the value of the best fit point source for each parameter. (e) Likelihood plot of each chain over 10,000 iterations.

For the scenario 1 sill inversion, where length and width are kept constant at 1 km, the source is deeper than the point source estimates but centered at a similar location. There is no greatly favored value of strike, and no distinct trends between the different varied parameters (Fig. 4.S4). The mean values of depth ($11.8 \pm .7 \text{ km}$), latitude ($41.5375^\circ \pm 0.0051^\circ$), and longitude ($-121.4447^\circ \pm 0.0081^\circ$) all contain the best fit depth of 12.1 km, latitude of 41.5374, and longitude of -121.4452 (Fig. 4.7a-d). For strike, the best fit value of 337 sits barely inside the mean range of (282 ± 55). The best fitting opening rate is -1.4 m/yr , and the distribution of opening rates for this sill scenario one reaches the upper bound of -1.5 m/yr repeatedly (Fig. 4.7e). This is due to the model wanting a larger volume to fit the widespread subsidence and using a larger opening rate as

the length and width are constrained to smaller values of 1 km each. Each chain in the inversion reaches convergence fairly quickly, within the first few hundred iterations of the model (Fig. 4.S5).

For the scenario 2 sill inversion, there are no obvious trends between any of the parameters varied, likely because the length and width results cover the full parameter space with no obvious peaks (Fig. 4.S6). While the mean length is 14.9 ± 2.8 km and width is 7.2 ± 1.6 km, the best fit sill favors a long, narrow sill of 19×4 km (76 km^2). There is better agreement between the mean values of depth (10.6 ± 1.3 km), strike (254 ± 22), center latitude ($41.5403^\circ \pm 0.0074^\circ$), and center longitude ($-121.4578^\circ \pm 0.0274^\circ$), with the best fit sill 10.1 km deep with a strike of 272, 41.5414 for latitude, and -121.4713 for longitude (Fig. 4.8a-f). Since the length and width of the sill are larger, the opening rate is several magnitudes smaller, with the best fitting opening rate at -0.02 m/yr (note that this is the same magnitude as the subsidence rate; Fig. 4.8g). Conversion takes longer than for the point source, approximately 1000 iterations for chains 1, 2, 4 and 5 and 1500 iterations for chain 3 (Fig. 4.S7).

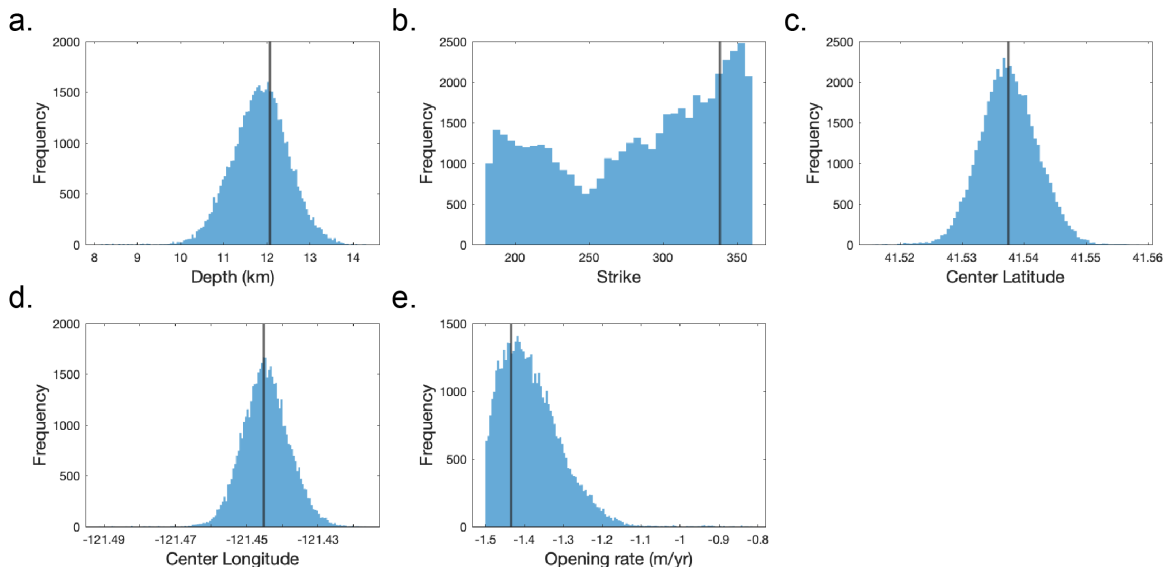


Figure 4.7. Distribution of depths (a), strike (b), center latitude (c), center longitude (d), and opening rate (e) accepted guesses for MCMC sill source model (scenario 1). Note that the burn in values (first 100 iterations of each chain) have been removed from the distributions for easier visualization of distribution shape. Black vertical line on each plot indicates the value of the best fit sill source (scenario 1) for each parameter.

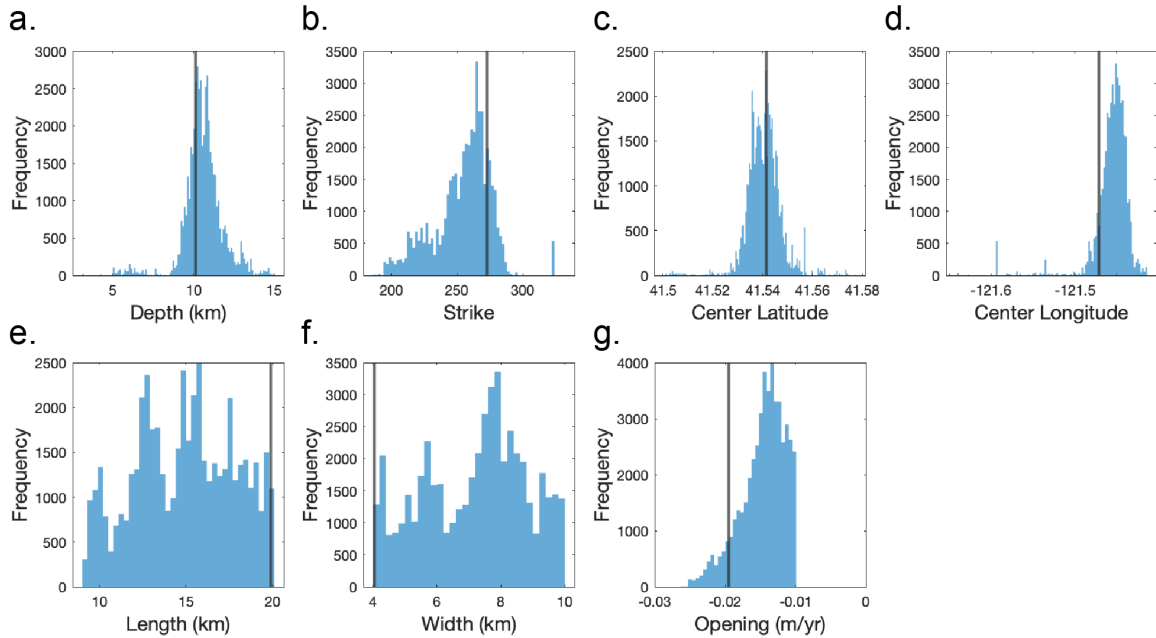


Figure 4.8. Distribution of depths (a), strike (b), center latitude (c), center longitude (d), length (e), width (f) and opening rate (g) accepted guesses for MCMC sill source model (scenario 2). Note that the burn in values (first 100 iterations of each chain) have been removed from the distributions for easier visualization of distribution shape. Black vertical line on each plot indicates the value of the best fit sill source (scenario 2) for each parameter.

When the two sill source scenarios are compared, the best fit constant length and width sill yields center coordinates to the east, similar to the best fit coordinates for the point source (Fig. 4.9a). These values are noticeably different from center locations from previous modeling (Dzurisin et al., 2002; Poland et al., 2006; Parker et al., 2014), but as previously stated, this study considers the broader edifice deformation including the subsidence patch to the southeast. Inclusion of the broader subsidence is also likely the cause of the deeper mean and best fit depths for the sill sources than previous studies (5 km for GNSS, 9.5 km for InSAR; Parker et al., 2014). When volume is calculated for the two sill model distributions, the mean volume change for scenario 1 sill is $-0.0014 \pm 0.0001 \text{ km}^3/\text{yr}$, which closely matches the mean volume change of point source estimates, both from this study as well as volume change estimates from modeling of previous InSAR data ($-0.0012 \text{ km}^3/\text{yr}$; Parker et al., 2014). For the scenario 2 sill, the mean volume change is $-0.0026 \pm 0.0087 \text{ km}^3/\text{yr}$. While the mean volume matches previous estimates of sill

volume change from leveling ($-0.002 \text{ km}^3/\text{yr}$; Dzurisin et al., 2002) and GNSS ($-0.0025 \text{ km}^3/\text{yr}$; Poland et al., 2006), standard deviation is higher when the length and width are not well constrained.

4.5 Discussion

Multiple causes of volume loss at depth have been discussed in previous models of Medicine Lake (Dzurisin et al., 2002; Poland et al., 2006; Parker et al., 2014). As the last eruption was $\sim 1\text{ka}$, the volume loss is likely not due to deflation of a source from that event. There is also volume loss due to cooling and crystallization of magma at depth, which was explored in each work, with Poland et al. (2006) also modeling the thermoelastic contraction of a hot cylindrical volume beneath Medicine Lake although they found that it did not fully explain the deformation. Parker et al. (2014) emphasize the contribution of volume loss, stating that the most likely cause of volume loss is either drainage from a reservoir deeper beneath Medicine Lake or cooling and crystallization of material within the intrusive complex imaged beneath the volcano. The best fitting sill model for scenario 2 suggests a long, narrow sill that spans nearly 20 km. This could also reflect a larger intrusive complex that is cooling and crystallizing over time, however if the subsidence is due to volume loss of such a large complex, then other large scale processes, such as loading from the edifice, should be taken into consideration.

4.5.1 *Effects of Edifice Loading*

In addition to volume loss at depth, surface loading from Medicine Lake's large edifice over a thermally weakened crust may explain subsidence. There is evidence to suggest thermal weakening occurs in the crust beneath Medicine Lake (Dzurisin et al., 1991; Blakely et al., 1997), reducing Young's modulus to lower values (10^9) that have still been observed at volcanic systems (Rubin & Pollard, 1987; Schultz, 1993). We use an axisymmetric solution for a point source load

on the surface of a spherical, liquid filled shell from Brotchie & Silvester (1969) and Brotchie (1971) that was modeled for Medicine Lake by Poland et al. (2006). Vertical deformation due to loading can be described by this model as:

$$z = \frac{Pl^2}{2\pi D} kei(x) \quad (2)$$

$$D = \frac{E * T^3}{12 * (1 - \nu^2)} \quad (3)$$

$$l = \left[\frac{D}{\left(\frac{E * T}{R^2} \right) + \rho} \right]^{1/4} \quad (4)$$

In equation 2, P is the load on the surface (kg), l is the radius of relative stiffness (m), D is the flexural stiffness of the shell cross section (N • m), x is the distance on the surface from the center of the load, and kei is a zero order Bessel-Kelvin function (Brotchie & Silvester, 1969). In equation 3, E is Young's modulus (N/m²), T is shell thickness (m), ν is Poisson's ratio (set to 0.25); in equation 4 R is the radius of the middle surface (m) and ρ is the mean relative density (kg/m³). To model deformation using the “thin, weak shell” scenario presented in Poland et al. (2006), T is set to 10,000 m and E is set to 10⁹ Pa. While a velocity rate cannot be constrained with an elastic model, an alternative approach assumes that the peak yearly deformation due to loading is 1.4 mm/yr, 10% of the maximum caldera subsidence rate of 1.4 cm/yr. We then vary the load and model the pattern of subsidence produced by a point source over a thin weak shell with 1.4 mm/yr at the center of the pattern (assumed beneath the center of the caldera). It is important to note that this choice is meant as an exploration of how inversion results will change if any of the deformation is attributed to loading; constraining the actual ratio of deformation from edifice loading to volume loss at depth requires additional modeling and data outside the scope of this work. The deformation from loading is then subtracted from the velocity data produced with InSAR, and the updated

deformation map is used in the same Bayesian MCMC modeling framework for one chain of 10,000 iterations for each source.

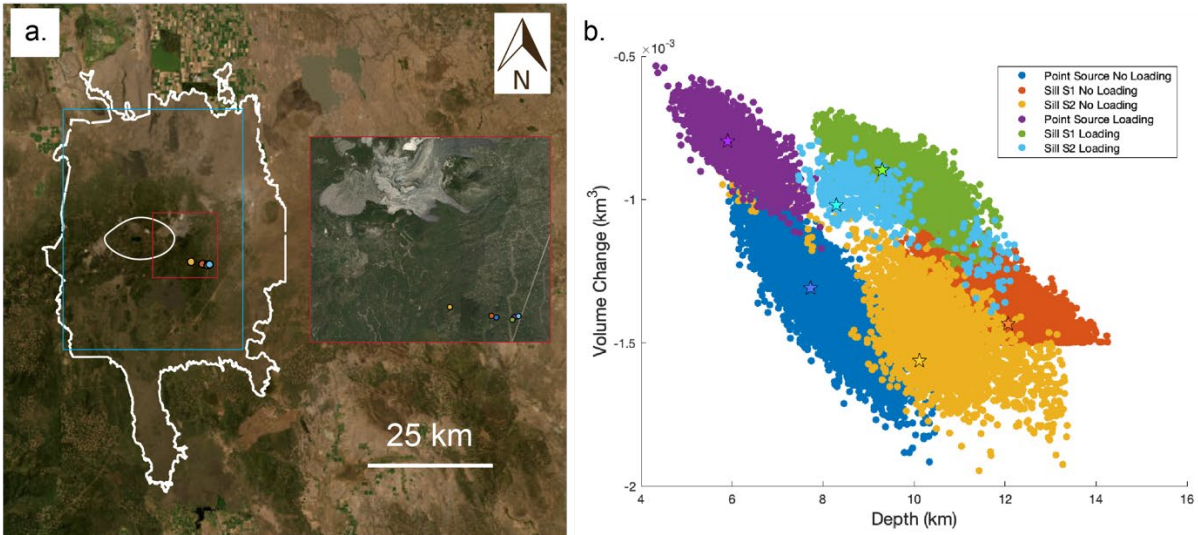


Figure 4.9. (a) Map of Medicine Lake edifice and caldera with best fitting source locations identified. Red box indicates inset image to the right zoomed in on center source locations. Light blue box indicates span of the edifice mapped by InSAR velocity and extent of Fig. 4.10. (b) Scatter plot comparing depth and volume change of accepted guesses for point and sill scenarios 1 and 2. (S1 – Scenario 1, S2 – Scenario 2, NL – No Loading, L – Loading). Best fitting sources are denoted by stars.

The inclusion of the loading deformation produces shallower best fit depths for each of the sources: 5.9 km for point source, 9.3 km for sill scenario 1, and 8.3 km for sill scenario 2 (Fig. 4.9b). While the center coordinates for the point source do not change considerably, the best fit sill source for scenario 1 is centered even more to the east ($41.5355^{\circ}, -121.4320^{\circ}$) than without loading ($41.5374^{\circ}, -121.4452^{\circ}$), and the best fit scenario 2 sill moves further south and further east ($41.5372^{\circ}, -121.4282^{\circ}$) (Fig. 4.9). There is still no agreement between the best fit scenario 2 sill source and the mean values for length and width, although the addition of deformation due to loading does broaden the dimensions of the best fitting sill. For the point source best fit, in addition to a shallower depth, there is a lower best fit volume change of $-0.0008 \text{ km}^3/\text{yr}$, consistent with the trend we see between the variables in the inversion without loading deformation where shallower depths are associated with smaller volume changes (Fig. 4.S3). The volume changes for both best

fit sill scenarios are also reduced to $-0.0009 \text{ km}^3/\text{yr}$ for scenario 1, and $-0.001 \text{ km}^3/\text{yr}$ for scenario 2 (Fig. 4.9b).

4.5.2 Comparing Model Residuals

For each best fit source, the likelihood increases when loading is taken into consideration. The most likely volume loss source is the scenario 2 volume loss sill of depth 8.2 km and volume loss of $0.001 \text{ km}^3/\text{yr}$, although the residuals from each best fitting source do not show noticeable differences (Fig. 4.10). The highest negative residuals occur within the caldera because the eastern subsidence caused most estimates to be centered between the two patches. The highest positive residuals are on the eastern flank, where uplift is indicated by vertical velocity results (Fig. 4.5a). While it is somewhat difficult to match velocity data when a significant portion is masked out due to incoherence, and there are several distinct patterns of deformation, the volume loss model for a larger sill with loading assumed having the highest likelihood opens the door for potential further study into the dynamics between edifice loading and localized volcanic signals.

4.6 Conclusion

Using ascending and descending Sentinel-1 InSAR, we constrain deformation across Medicine Lake's edifice from 2017-2021. We minimize residual phase across ascending and descending networks of interferograms to reduce noise and correct for tropospheric artifacts using the ERA5 weather model.

We find a similar pattern of radial subsidence peaking in the center of the caldera at 1.4 cm/yr and then decreasing outward from the caldera to similar previous studies (Dzurisin et al., 2002; Poland et al., 2006; Parker et al., 2014). Our vertical velocity data also reveals a patch of subsidence to the east of the caldera extending southward, in an area not covered by leveling or GNSS data. This signal was previously imaged by InSAR spanning 2004-2011 (Parker et al.,

2014). We then model the deformation using a MCMC model in a Bayesian framework for three different volume loss sources; a point source in an elastic half space, a sill with its length and width constrained to one kilometer, and a sill with variable length and width. The variable length and width sill has the best fit for volume loss, potentially suggesting that a larger mass, such as the sub-solidus intrusive complex beneath Medicine Lake, could be experiencing volume loss due to cooling and contraction.

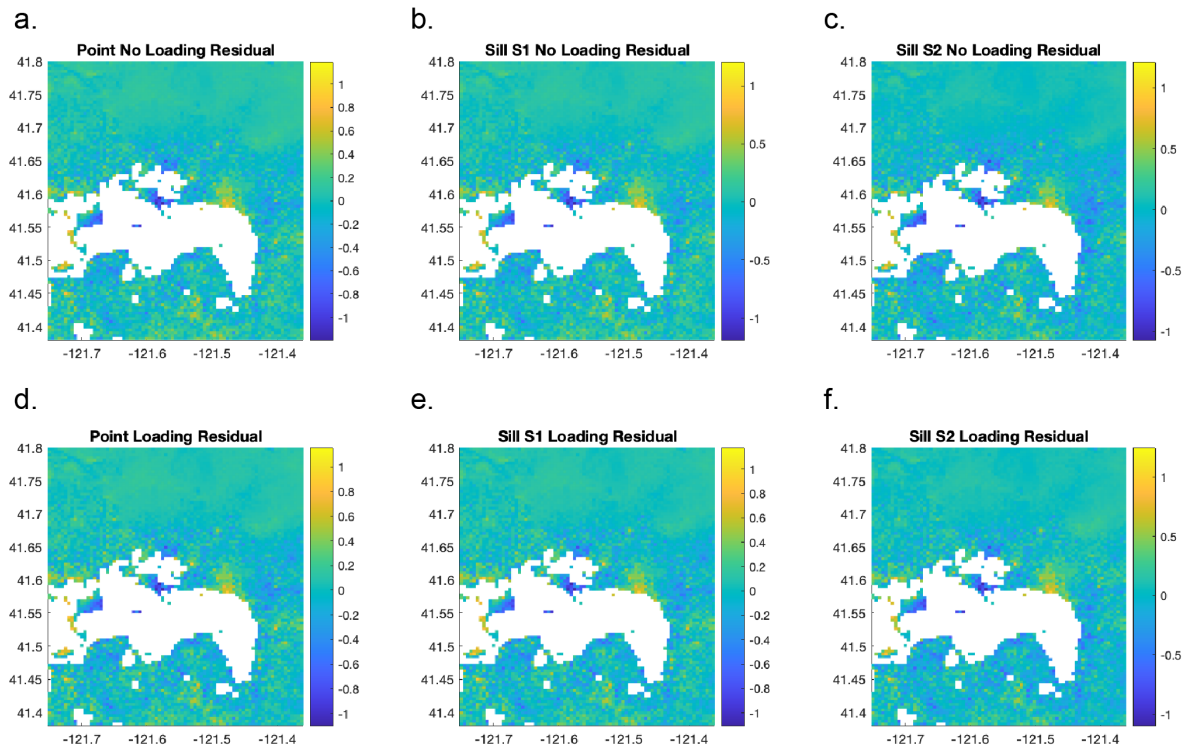


Figure 4.10. Maps of residuals for each best fitting source modeled including modeling without loading (a-c) and modeling with loading (d-f). Residual values are reported in centimeters on the color bars (S1 – scenario 1, S2 – scenario 2).

When edifice loading contributes to 10% of the peak subsidence within the caldera, we produce models that better fit the data, though the best fitting source is still the sill with larger length and width. This best fitting source sits at 8.3 km depth and has a volume loss of 0.001 km³/yr. The potential interplay between loading and volume loss could be further explored by either (1) assuming a variety of ratios of loading to volume loss deformation or (2) creating a more

complex model (finite element or finite volume) that considers both processes. There is also the opportunity to further explore the dynamic between the eastern subsidence patch and the caldera subsidence and how these two have interacted throughout time. While only one source was modeled for volume loss in this work, potentially combining multiple sources of volume loss with deformation due to loading could address the complex deformation signal at Medicine Lake. Understanding how these different signals interact at a system such as Medicine Lake that has not experienced an eruption for ~1ka could be useful for isolating signal related to magma activity from larger scale longer term signals at active caldera systems.

4.7 Acknowledgements

The research reported in this publication is supported by the University of Oregon (UO) and by NSF Grant EAR-1940994. Sentinel-1 data is provided by ESA/Copernicus and Landsat-8 data is provided through NASA. GNSS downloaded through the University of Nevada Reno. We would also like to thank Mike Poland and Emily Montgomery-Brown for useful discussions.

4.8 Data and Code Availability

Sentinel-1 Single Look Complex (SLC) data was downloaded through the Alaska Satellite Facility Vertex Platform (<https://search.asf.alaska.edu/#/>). These SLC's were then processed using the ISCE2 software developed by NASA (<https://github.com/isce-framework/isce2>). Figures were made with MATLAB 2020 and compiled with Adobe Illustrator. The output deformation files and MCMC code will be available here (<https://github.com/rcbussard>).

4.9 Supporting Information

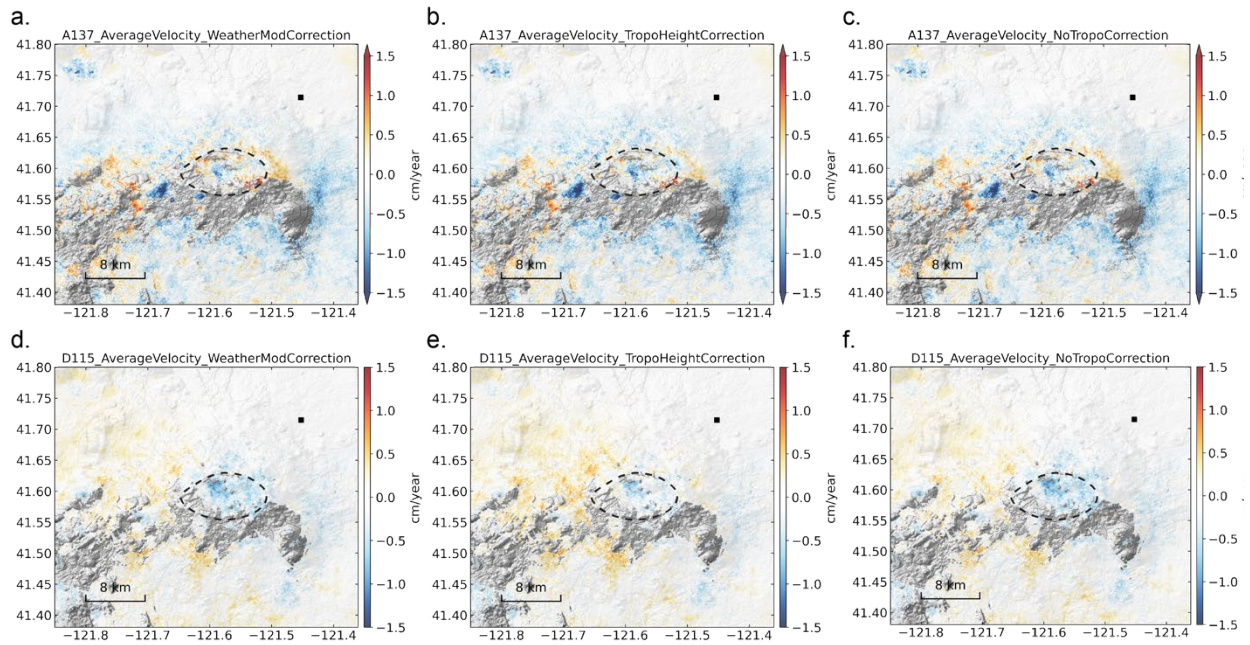


Figure 4.S1. InSAR ascending (a-c) and descending (d-f) line of sight velocity maps for a weather model (ERA5) tropospheric correction (a,d), an empirical height correction (b,e) and no tropospheric correction (c,f).

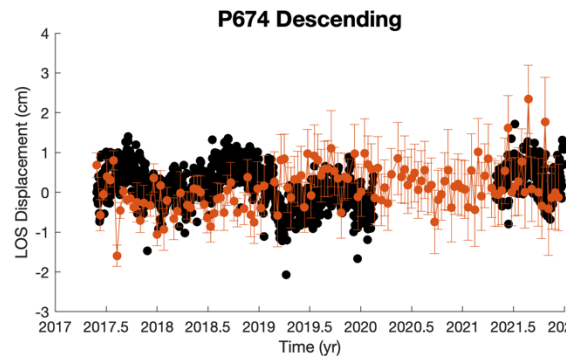
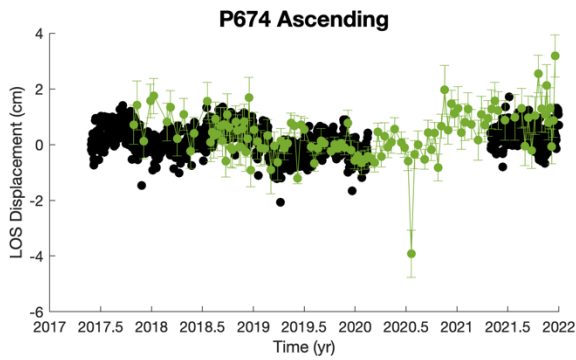
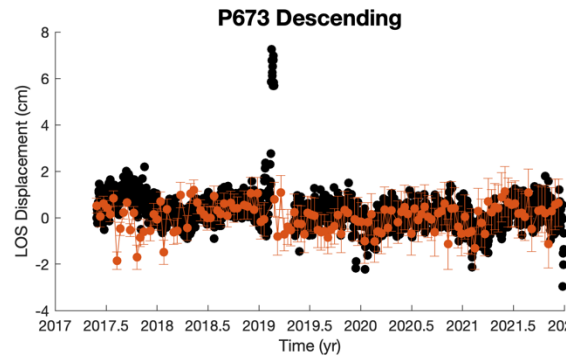
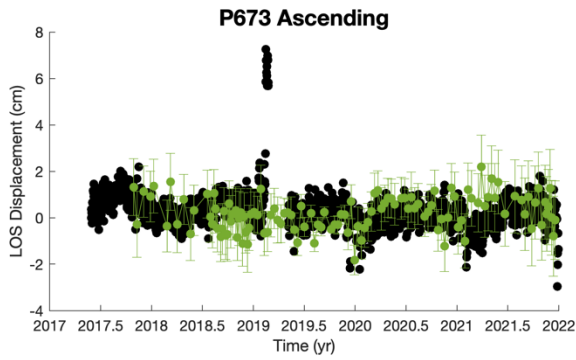
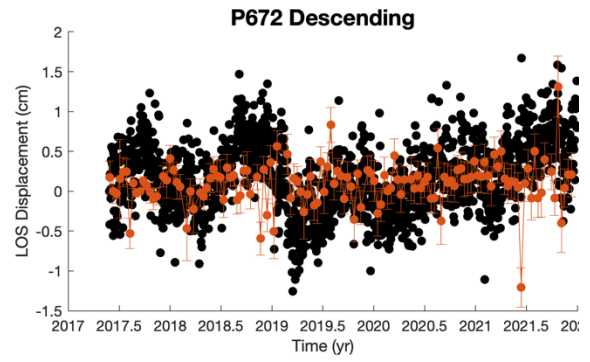
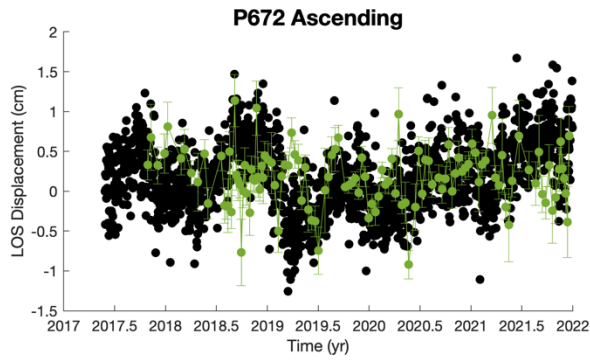


Figure 4.S2. InSAR ascending (a, c, e) and descending (b, d, f) timeseries compared with GNSS data from P672 (a, b), P673 (c, d) and P674 (e, f) stations. Error bars calculated from variance of surrounding pixels to pixel corresponding to GNSS location.

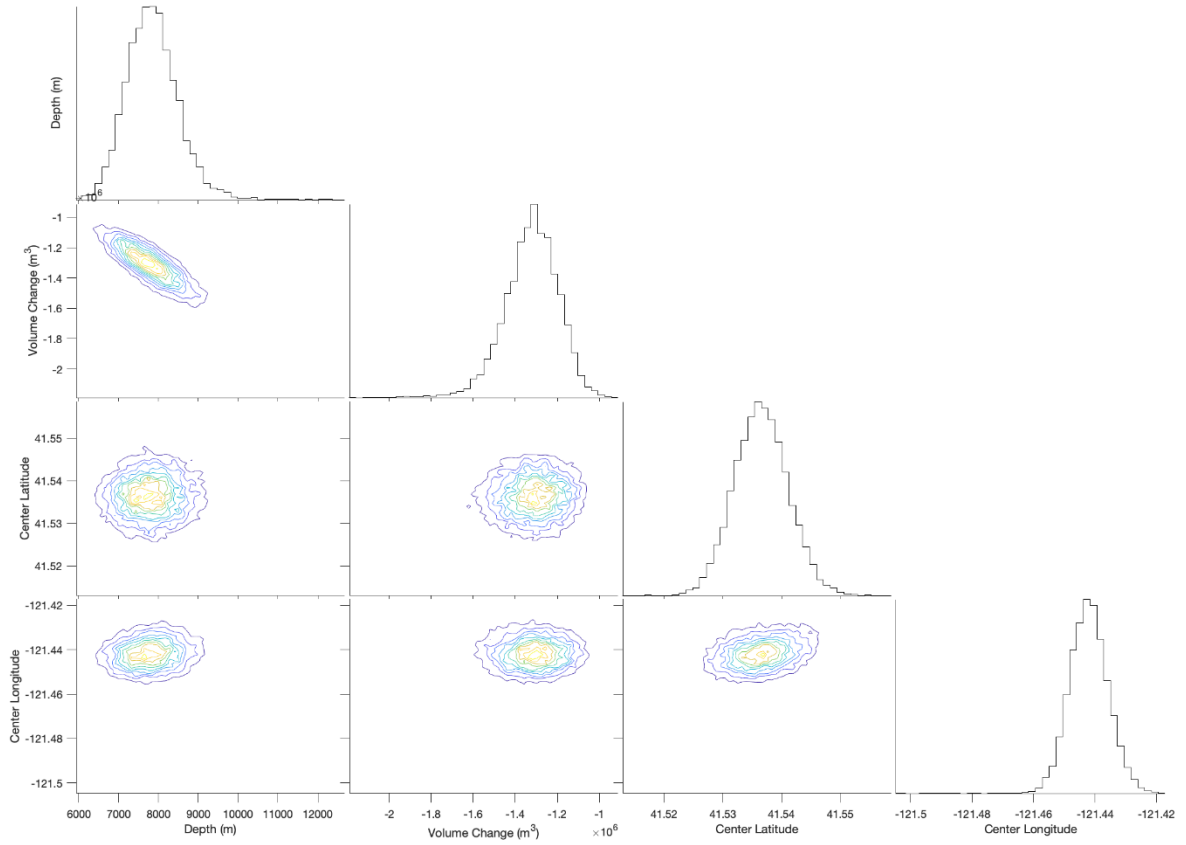


Figure 4.S3. Histogram plots showing distribution of accepted guess values for point source inversion parameters (depth, volume change, center latitude, and center longitude) as well as corresponding Kernel Density Estimation plots showing trends between the values. Note that the burn in values (first 100 iterations of each chain) have been removed from the distributions for easier visualization of distribution shape.

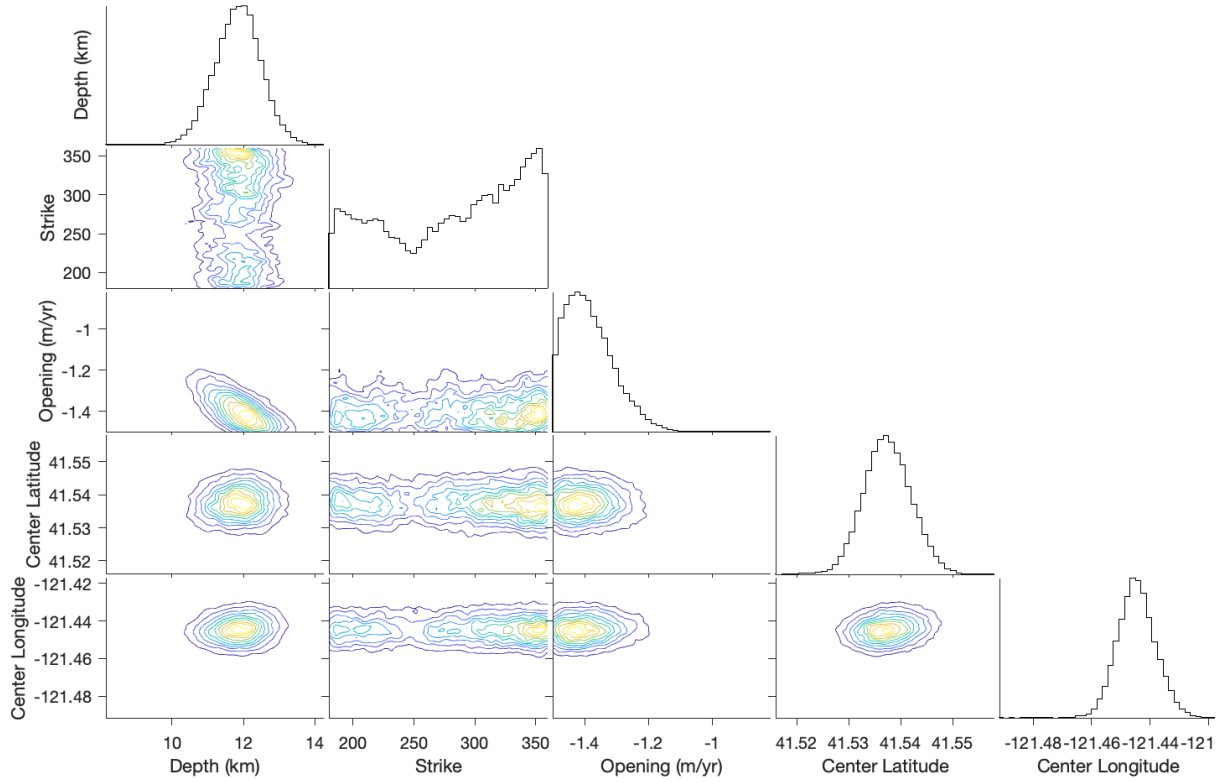


Figure 4.S4. Histogram plots showing distribution of accepted guess values for sill source inversion scenario 1 parameters (depth, strike, opening, center latitude, and center longitude) as well as corresponding Kernel Density Estimation plots showing trends between the values. Note that the burn in values (first 100 iterations of each chain) have been removed from the distributions for easier visualization of distribution shape.

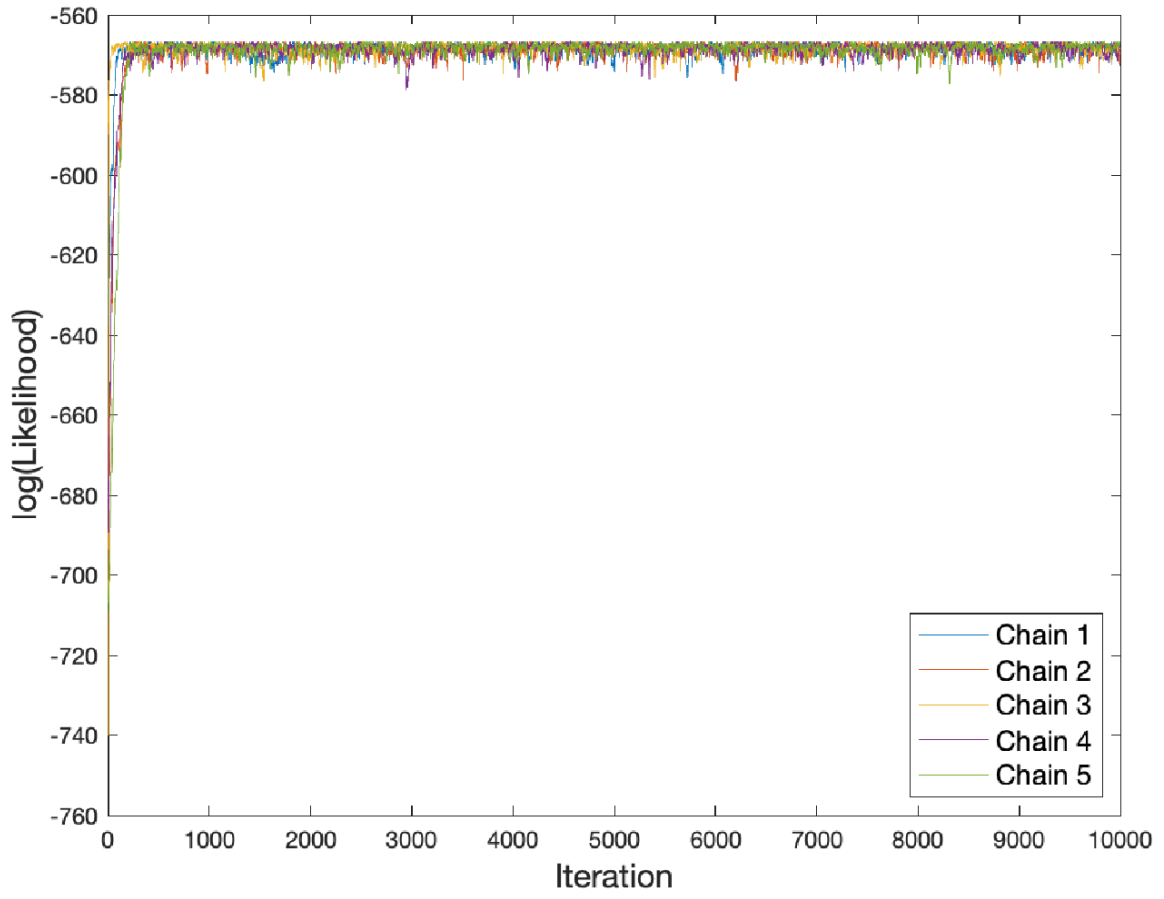


Figure 4.S5. Likelihood plot for each of the five chains in the MCMC sill scenario 1 inversion.

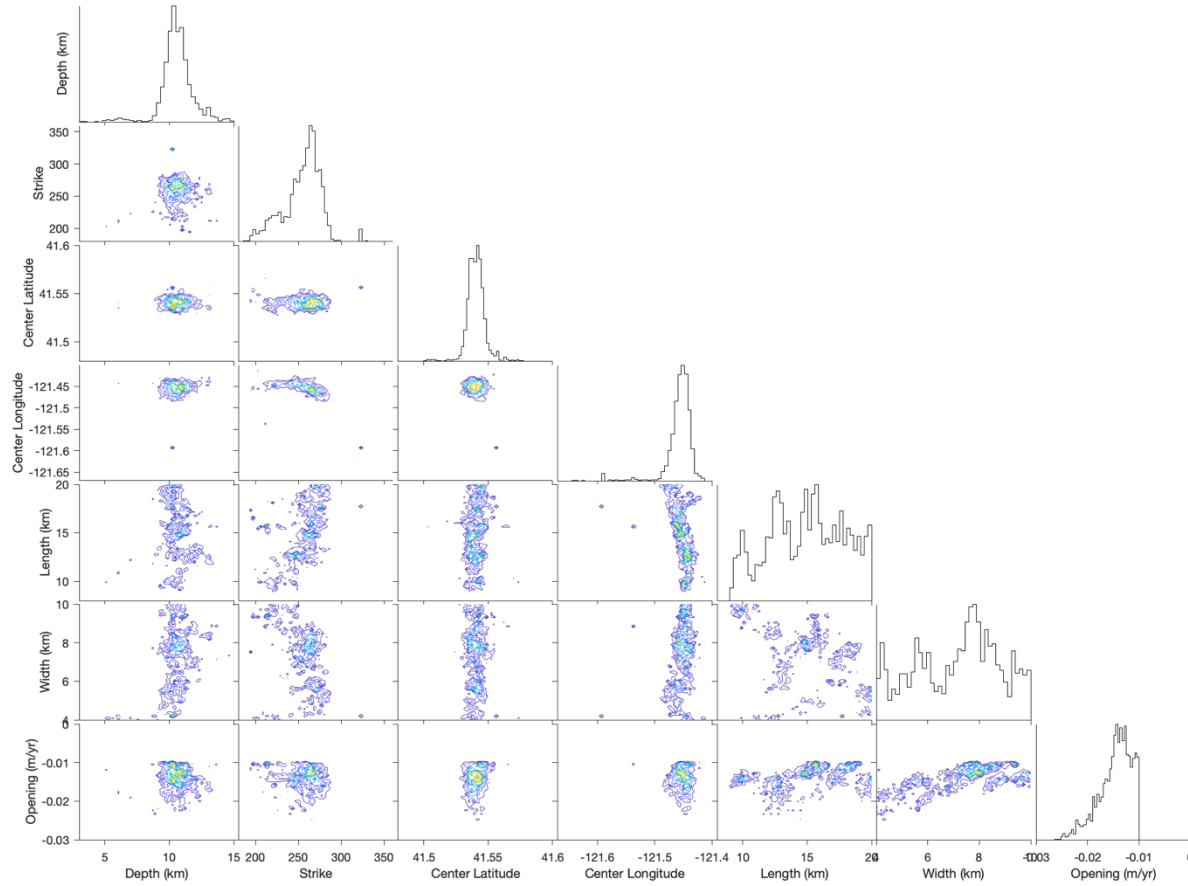


Figure 4.S6. Histogram plots showing distribution of accepted guess values for sill source inversion scenario 2 parameters (depth, strike, center latitude, center longitude, length, width, and opening) as well as corresponding Kernel Density Estimation plots showing trends between the values. Note that the burn in values (first 100 iterations of each chain) have been removed from the distributions for easier visualization of distribution shape.

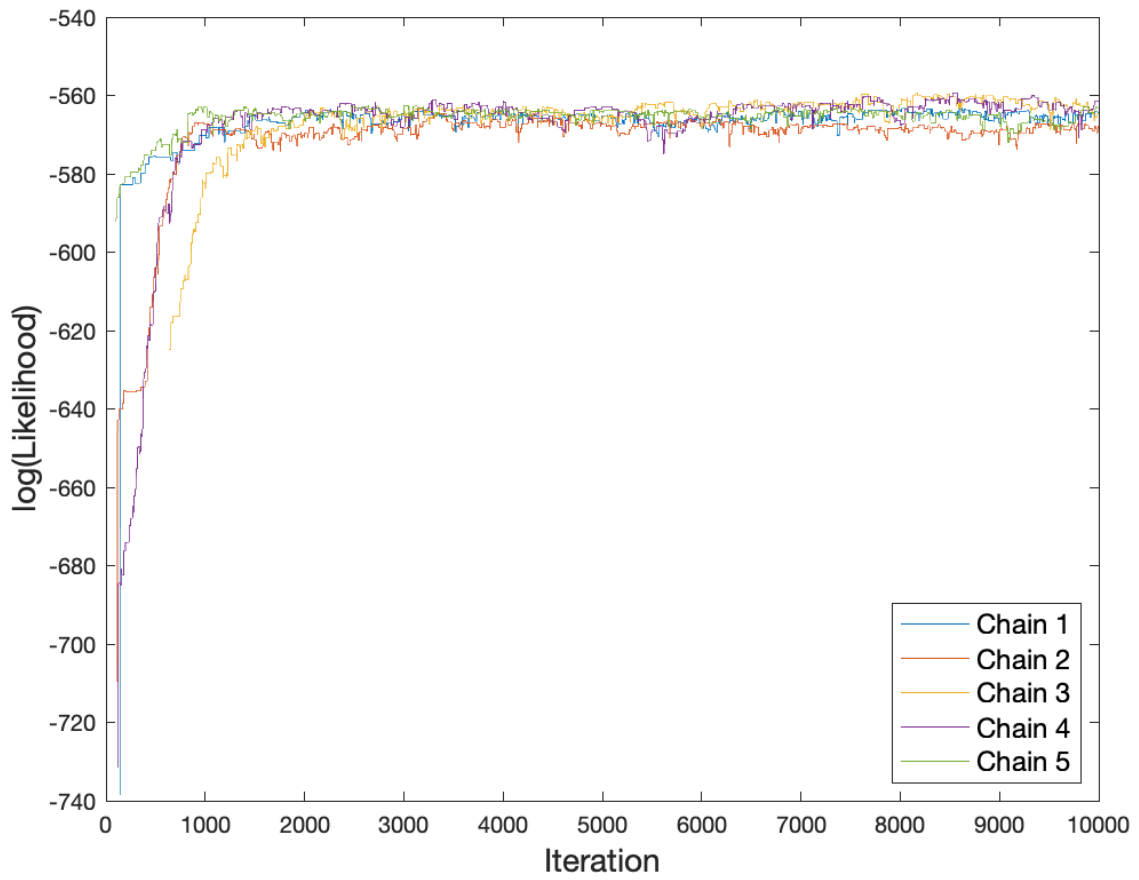


Figure 4.S7. Likelihood plot for each of the five chains in the MCMC sill scenario 2 inversion.

CHAPTER V

CONCLUSIONS AND FUTURE DIRECTIONS

The central theme of each chapter in this dissertation is using mapping techniques that suit different volcanic systems to understand surface and sub-surface processes occurring at these systems. Determining the magmatic evolution of volcanoes through time and quantifying how well we are able to observe this evolution into present day is crucial for preparing for future changes to these systems and what local and global volcanic hazards might occur as a result.

Chapter II used statistical analysis methods on a variety of distributed volcanic fields to determine if vent clustering occurred in the fields, where it occurred, and potential clustering mechanisms. By using the area between vents mapped with Voronoi tessellations, we found that the Springerville Volcanic Field, the cinder cones and shield volcanoes of the Central Cascades, and the cinder cones and shields of the Washington Cascades all experienced clustering. When the length scale from the Voronoi analysis was compared with a distance based metric through Kernel Density Estimation, we found that in fields where the two length scales differ (Springerville, Central Cascade cinder cones, Central Cascade shields), the area-based clustering length scale tends to pick up clustering as a result of magma storage in the crust, while the distance based length scale emphasizes alignments in fields produced by regional tectonic controls. In regions where length scales did not substantially differ, Washington cinder cones and Washington shields, this indicated that changes in density reflected changes in eruption type and subsequently vent type (cinder cone vs. shield) through time. This work was a useful comparative study of clustering between different volcanic fields and explored the use of a new area based metric for defining clustering length scales, offering several avenues of further study.

The results of Chapter II focus only on the six fields of interest, with Auckland and Springerville being the only fields of the study where no focused stratovolcanoes are present. While the dynamics between distributed and focused volcanism are relatively unexplored in the Cascades, which informed our decision to study them, performing the same analysis as detailed in this work on other intraplate volcanic fields could lead to more direct comparisons with Auckland and Springerville. Potential options for other fields to compare with include the distributed volcanic fields across the southwestern U.S. that neighbor Springerville, as they all have dozens to hundreds of vents and share the same tectonic region, albeit to different degrees based on the field location (Valentine et al., 2021). Comparing the clustering length scales at these fields could show how different regions across the Colorado Plateau and Basin and Range are influenced by the extensional tectonics present.

In addition to analyzing other volcanic fields, the length scales produced with our Voronoi methodology could be compared with other bandwidth selection methods besides Silverman's. These include methods such as cross validation (Duong et al., 2007) or Asymptotic Mean Squared Error (Duong & Hazelton, 2003). Comparison between our metric and these could determine if there are any systematic differences and what these differences might represent in terms of physical processes. We could also explore the use of asymptotic kernels for the Kernel Density Estimation, and adjust the bounding region shape (e.g. use our convex hull bounding region and add a buffer of constant distance). These additional comparisons and statistical tests would provide further context for how our methodology compares with existing methods and how these methods can complement each other during analysis.

While the use of spatial analysis allows us to draw observations for distributed fields based solely on vent locations, to get at mechanisms affecting the fields, additional data such as age,

composition, and eruption type are required. In the future this would require additional field campaigns to either augment existing datasets that cover some field vents (e.g. composition data at Springerville) or sampling all of the vents to get data. Having these data available would help characterize clustering in fields over time, and could answer questions of how long magma stays in the crust when ascending; does it rise fairly quickly as in Auckland or stall and assimilate (producing more evolved compositions) as in Springerville?

Chapter III focuses on the ability of the remote sensing method InSAR to capture ground deformation measurements at Mt. St. Helens volcano located in southwestern Washington. Ground deformation has identified as a precursor of potential magmatic activity, and even when eruptions don't occur, ground deformation measurements at a volcano can be useful for constraining properties of its magmatic system. However, surface change such as snow fall can degrade InSAR and make wide regions around volcanoes (as well as the volcanoes themselves) difficult to image. We utilize a computationally fast, inexpensive neural network to classify snow cover in 29 Landsat-8 optical images spanning 2014-2021 and find that snow cover emplaced over bare rock regions reduces coherence from 1 to 0.3. We model inflation of a magma chamber as a point source at a range of depths (5-15 km) experiencing a range of positive volume changes (10-60 million m^3) and find that during times of high snow cover, the amount of visible pixels with centimeter scale deformation is reduced by 40% for all cases and is reduced ~85-90% for deep, low-volume increase cases. This suggests that for Mt. St. Helens, additional methods of viewing ground deformation such as GNSS should be enhanced with more site installations to monitor the volcano during months when there's widespread snow cover.

The neural network only produces a binary output of snow cover or no snow cover for each pixel in the optical imagery it classifies, but there are other naturally occurring land types besides

snow cover that degrade coherence such as vegetation (both deciduous and coniferous). A future step for this work involves adapting the neural network to read in multiple land cover types at once and output files that classify different surface covers in the same image. Being able to track various types of vegetation as well as snow cover over time would be useful for comparing how each land cover type degrades coherence. The model could also be applied to other volcanoes in the Cascade Volcanic Arc where snow cover is less prevalent but vegetation covers significant portions of the region (e.g. Newberry, Medicine Lake). The neural network could also be implemented on other arcs in various environments such as the Central American Volcanic Arc where there is less snow cover but prevalent tropical vegetation, as well as the Andes Volcanic Arc that experiences a combination of vegetation and snow cover similar to the volcanoes of the Cascades.

There is also the option to expand the data that the neural network utilizes for training and classification. Currently, six bands of Landsat-8 optical data are used, with the requirement that these bands come from acquisition dates that have less than 5% cloud cover. As a result, over a six year period there were only twenty nine usable Landsat-8 images to track snow cover. This number of available images could be augmented by adding in other satellites such as Sentinel-2 that also has multi-spectral optical capabilities. Other datasets beyond just optical could be utilized as well, either from bands such as the thermal band on Landsat-8 or from other satellites with thermal imaging capabilities such as ASTER. This would require adapting the model to train off various pixel values based off the different satellites, but could increase the amount of acquisitions available and bolster classification ability by utilizing various attributes of snow covered pixels.

Chapter IV maps vertical deformation at Medicine Lake Volcano with combined ascending and descending Sentinel-1 InSAR data spanning 2017-2021. Individual acquisitions as well as specific interferograms are removed to limit noise in the ascending and descending networks which

are then combined to create a vertical velocity map over Medicine Lake's edifice. This deformation is then used by a Markov Chain Monte Carlo (MCMC) model in a Bayesian framework to constrain sources of volume loss at depth beneath the edifice. The vertical velocity map indicates two patches of subsidence: (1) at the center of the caldera and (2) on the eastern side of the edifice. These two patches compete for determining where the volume loss source should be located, and as a result the source estimates sit between the two. The same MCMC model is run again on deformation data that assumes loading is contributing a constant percent of subsidence to the total velocity. The best fitting source comes from a sill at depth 8.2 km with a volume loss of 0.001 km³/yr with loading assumed.

For the work in Chapter IV, the models utilized assume constant deformation rates and behave elastically. Realistically however, in a region such as Medicine Lake where there is thought to be a large body of heat beneath the surface, viscoelastic behavior is likely occurring. One way to begin addressing the presence of viscoelastic deformation would be using a simple analytic model of a spherical chamber with a spherical viscoelastic shell surrounding it (Dragoni, 1989). This would provide another way to model volume loss while also considering the temporal evolution of the deformation, and timeseries of data could be used at various points around Medicine Lake as opposed to average velocity maps. Deformation data from this study as well as previous works could also be combined to (1) view points at Medicine Lake that have the temporal evolution of deformation more constrained (i.e. where the leveling, GNSS, and InSAR datasets intersect spatially) and (2) create timeseries at these points spanning decades. The viscoelastic shell model used could constrain additional properties such as the viscosity of the surrounding material as well as the potential start time of the subsidence. Constraining this start time, as well as the rate of decrease in subsidence (the taper over time often shown with the viscoelastic shell

modeling) would allow for better constraints on the mechanism causing the subsidence; if the start of the deformation was recent (last fifty years) and is tapering off soon, then the cause likely has to do with magma transport instead of a combination of long term processes such as edifice loading and cooling that are currently suggested.

There is also the challenge of understanding the region of subsidence to the east of the caldera where the initial leveling route did not cover and where there are no current continuous GPS stations. Given that the subsidence region to the east of the caldera is present both in InSAR data spanning 2004-2011 and 2017-2021, this could suggest another source of volume loss in the crust. It is crucial to understand the interplay between this eastern source of subsidence and the cause of caldera subsidence, as how these two regions deform could suggest connection between the two sources and a more active storage region than initially thought. Also, while gravity surveys have recently performed over the caldera, it could be useful to also perform a survey over this eastern region to see if any anomalies could be detected and what that might suggest for potential storage to the east of the caldera.

Throughout each of these chapters, the abilities, and challenges of different mapping techniques over volcanoes are displayed. Understanding the capabilities of each technique at different volcanic systems and what their data means as well as potential biases are crucial for determining the mapping methods that will provide the most insightful and helpful knowledge on volcanic systems when we are trying to mitigate their hazards.

REFERENCES CITED

- Anderson, C.A. (1941). Volcanoes of the Medicine Lake Highland. University of California Publications, Bulletin of Department of Geological Sciences, 25 (7), 347-422.
- Anderson, K. & Johanson, I. (2022). Incremental caldera collapse at Kīlauea Volcano recorded in ground tilt and high-rate GNSS data, with implications for collapse dynamics and the magma system. *Bulletin of Volcanology*, 84 (10), 89.
- Anderson, K. & Segall, P. (2013). Bayesian inversion of data from effusive volcanic eruptions using physics-based models: Application to Mount St. Helens 2004-2008. *Journal of Geophysical Research: Solid Earth*, 118, 2017-2037.
- Anderson, K. R., Johanson, I. A., Patrick, M. R., Gu, M., Segall, P., Poland, M. P., Montgomery-Brown, E.K. & Miklius, A. (2019), Magma reservoir failure and the onset of caldera collapse at Kīlauea Volcano in 2018. *Science*, 366(6470).
- Bargar, K.E. (2001). Fluid-inclusion studies of hydrothermal minerals from geothermal drill holes at MLV, northern California. *California Geology*, 54 (5), 12-21.
- Battaglia, M., Cervelli, P.F. & Murray, J.R. (2013). Modeling crustal deformation near active faults and volcanic centers-A catalog of deformation models. *U.S. Geological Survey Techniques and Methods*, 13, 96.
- Bebbington, M. (2013). Assessing probabilistic forecasts of volcanic eruption onsets. *Bulletin of Volcanology*, 75, 1-13.
- Bebbington, M. (2015). Spatio-volumetric hazard estimation in the Auckland volcanic field. *Bulletin of Volcanology*, 77, 1-39.
- Bebbington, M. & Cronin, S.J. (2011). Spatio-temporal hazard estimation in the Auckland Volcanic Field, New Zealand, with a new event-order model. *Bulletin of Volcanology*, 73, 55-72.
- Bennett, J.H., Sherburne, R.W., Cramer, C.H., Chesterman, C.W. & Chapman, R.H. (1979). Stephens Pass earthquakes, Mount Shasta-August 1978. *California Geology*, 32 (2), 27-34.
- Berardino, P., Fornaro, G., Lanari, R. & Sansosti, E. (2002), A new algorithm for surface deformation monitoring based on small baseline differential SAR interferograms. *IEEE Geoscience and Remote Sensing*, 40, 2375-2383.
- Biggs, J., Ebmeier, S.K., Aspinall, W.P., Lu, Z., Pritchard, M.E., Sparks, R.S.J. & Mather, T.A. (2014). Global link between deformation and volcanic eruption quantified by satellite imagery. *Nature Communications*, 5, 3471.
- Blakely, R.J., Christiansen, R.L., Guffanti, M., Wells, R.E., Donnelly-Nolan, J.M., Muffler, L.J.P., Clynne, M.A. & Smith, J.G. (1997). Gravity anomalies, Quaternary vents, and Quaternary

faults in the southern Cascade Range, Oregon and California, implications for arc and backarc evolution. *Journal of Geophysical Research*, 102, 22513-22527.

Bray, A., Wong, K., Barr, C. & Schoenberg, F. (2014). Voronoi residual analysis of spatial point process models with applications to California earthquake forecasts. *Annals of Applied Statistics*, 8, 2247-2267.

Brenna, M., Cronin, S.J., Smith, I., Sohn, Y.K., & Maas, R. (2012). Spatio-temporal evolution of a dispersed magmatic system and its implications for volcano growth, Jeju Island Volcanic Field, Korea. *Lithos*, 148, 337-352.

Brenna, M., Cronin, S.J., Smith, I., Tollan, P., Scott, J., Prior, D., Bambery, K., & Ukstins, I. (2018). Olivine xenocryst diffusion reveals rapid monogenetic basaltic magma ascent following complex storage at Pupuke Maar, Auckland Volcanic Field, New Zealand. *Earth and Planetary Science Letters*, 499, 13-22.

Brotchie, J.F. (1971). Flexure of a liquid-filled spherical shell in a radial gravity field. *Modern Geology*, 3, 15-23.

Brotchie, J.F. & Silvester, R. (1969). On crustal flexure. *Journal of Geophysical Research*, 74, 5240-5252.

Brumbaugh, D.S., Hodge, B.E., Linville, L. & Cohen, A. (2014). Analysis of 2009 earthquake swarm near Sunset Crater volcano, Arizona. *Journal of Volcanology and Geothermal Research*, 285, 18-28.

Bürgmann, R., Rosen, P. A., & Fielding, E. J. (2000), Synthetic aperture radar interferometry to measure Earth's surface topography and its deformation. *Annual review of earth and planetary sciences*, 28(1), 169-209.

Cañón-Tapia, E. (2020). Influence of method selection on clustering analyses of point-like features: Examples from three zones of distributed volcanism. *Geomorphology*, 354.

Cañón-Tapia, E. (2022). Kernel Analyses of Volcanic Vent Distribution: How Accurate and Complete are the Objective Bandwidth Selectors? *Frontiers in Earth Science*, 10, 779095.

Cassidy, J. & Locke, C. (2010). The Auckland volcanic field, New Zealand: Geophysical evidence for structural and spatio-temporal relationships. *Journal of Volcanology and Geothermal Research*, 195, 127-137.

Cebriá, J.M., Martín-Escorza, C., López-Ruiz, J., Morán-Zenteno, D.J. & Martiny, B.M. (2011). Numerical recognition of alignments in monogenetic volcanic areas: Examples from the Michoacán-Guanajuato Volcanic Field in Mexico and Calatrava in Spain. *Journal of Volcanology and Geothermal Research*, 201, 73-82.

- Champion, D.E. & Donnelly-Nolan, J.M. (1994). Duration of eruption at the Giant Crater lava field, Medicine Lake volcano, California, based on paleomagnetic secular variation. *Journal of Geophysical Research*, 99, 15,595-15,604.
- Chiarabba, C., Amato, A. & Evans, J.R. (1995). Variations on the NeHT high-resolution tomography method: a test of technique and results for Medicine Lake volcano, northern California. *Journal of Geophysical Research*, 100, 4035-4052.
- Christiansen, R. L., Peterson, D. W., Lipman, P. W., & Mullineaux, D. R. (1981), Chronology of the 1980 eruptive activity. *US Geologic Survey Professional Paper*, 1250, 17-30.
- Condit, C.D. & Connor C.B. (1996). Recurrence rates of volcanism in basaltic volcanic fields: An example from the Springerville volcanic field, Arizona. *Geological Society of America Bulletin*, 108, 1225-1241.
- Connor, C.B. (1990). Cinder cone clustering in the Trans-Mexican Volcanic Belt: Implications for Structural and Petrologic Models. *Journal of Geophysical Research*, 95, 19,395-19,405.
- Connor, C.B. & Hill, B. (1995). Three nonhomogeneous Poisson models for the probability of basaltic volcanism: Application to the Yucca Mountain region, Nevada. *Journal of Geophysical Research*, 100, 10,107-10,125.
- Connor, C.B., Condit, C., Crumpler, L. & Aubele, J. (1992). Evidence of Regional Structural Controls on Vent Distribution: Springerville Volcanic Field, Arizona. *Journal of Geophysical Research*, 97, 12,349-12,359.
- Connor, C.B., Connor, L.J., Germa, A., Richardson, J.A., Bebbington, M., Gallant, E. & Saballos, J.A. (2019). How to use kernel density estimation as a diagnostic and forecasting tool for distributed volcanic vents. *Statistics in Volcanology*, 5, 1-25.
- Conway, F.M., Connor, C.B., Hill, B.E., Condit, C.D., Mullaney, K. & Hall, C.M. (1998). Recurrence rates of basaltic volcanism in SP cluster, San Francisco volcanic field, Arizona. *Geology*, 26, 655-658.
- Cramer, C.H. (1978). The Stephen's Pass earthquake swarm of August 1978, east of Mt. Shasta, California. *Eos Transactions AGU*, 59 (12), 1130.
- Cressie, N.A.C. (1991). Statistics for spatial data. *New York: John Wiley and Sons*.
- Criswell, C. W. (1987), Chronology and pyroclastic stratigraphy of the May 18, 1980, eruption of Mount St. Helens, Washington. *Journal of Geophysical Research: Solid Earth*, 92(B10), 10237-10266.
- Deligne, N., Conrey, R., Cashman, K., Champion, D. & Amidon, W. (2016). Holocene volcanism of the upper McKenzie River catchment, central Oregon Cascades, USA. *GSA Bulletin*, 128, 1618-1635.

- Deng, F., Connor, C.B., Malservisi, R., Connor, L., White, J., Germa, A. & Wetmore, P. (2017). A Geophysical Model for the Origin of Volcano Vent Clusters in a Colorado Plateau Volcanic Field. *Journal of Geophysical Research: Solid Earth*, 122, 8910-8924.
- Di Traglia, F., Morelli, S., Casagli, N. & Monroy, V. (2014). Semi-automatic delimitation of volcanic edifice boundaries: Validation and application to the cinder cones of the Tancitaro-Nueva Italia region (Michoacán-Guanajuato Volcanic Field, Mexico). *Geomorphology*, 219, 152-160.
- Donnelly-Nolan, J.M. (2006). Chemical analyses and K-Ar ages of samples from 13 drill holes, Medicine Lake volcano, California. *U.S. Geologic Survey Open-File Report, 2006. 1041*, 20.
- Donnelly-Nolan, J.M. & Lanphere, M.A. (2005). Argon dating at and near Medicine Lake volcano, California: Results and data. *U.S. Geologic Survey Open-File Report, 2005. 1416*. 37
- Donnelly-Nolan, J.M., Champion, D.E., Grove, T.L. Baker, M.B., Taggart Jr., J.E., Bruggman, P.E. (1991). The Giant Crater lava field: Geology and geochemistry of a compositionally zoned, high-alumina basalt to basaltic andesite eruption at Medicine Lake volcano, California. *Journal of Geophysical Research*, 96, 21,843-21,863.
- Donnelly-Nolan, J.M., Grove, T.L., Lanphere, M.A., Champion, D.E. & Ramsey, D.W. (2008). Eruptive history and tectonic setting of Medicine Lake Volcano, a large rear-arc volcano in the southern Cascades. *Journal of Volcanology and Geothermal Research*, 177, 313-328. doi: 10.1016/j.jvolgeores.2008.04.023
- Duda, T. & Canty, M. (2010), Unsupervised classification of satellite imagery: Choosing a good algorithm. *International Journal of Remote Sensing*, 23, 2193-2212.
- Dunne, R. A. & Campbell, N. A. (1997), On the pairing of the softmax activation and cross-entropy penalty functions and the derivation of the softmax activation function. In *Proc. 8th Aust. Conf. on the Neural Networks, Melbourne* (Vol. 181, p. 185).
- Duong, T. (2007). ks: kernel density estimations and kernel discriminant analysis for multivariate data in R. *Journal of Statistical Software*, 21, 1-16.
- Duong, T. & Hazelton, M.L. (2003). Plug-in bandwidth selectors for bivariate kernel density estimation. *Journal of Nonparametric Statistics*, 15, 17-30.
- Dzurisin, D., Donnelly-Nolan, J.M., Evans, J.R. & Walter, S.R. (1991). Crustal Subsidence, Seismicity, and Structure Near Medicine Lake Volcano, California. *Journal of Geophysical Research*, 96, 16,319-16,333.
- Dzurisin, D., Lisowski, M. & Wicks, C.W. (2009), Continuing inflation at Three Sisters volcanic center, central Oregon Cascade Range, USA, from GPS, leveling and InSAR observations. *Bulletin of Volcanology*, 71, 1091-1110.

Dzurisin, D., Lisowski, M., Poland, M. P., Sherrod, D. R., & LaHusen, R. G. (2008), *Constraints and conundrums resulting from ground-deformation measurements made during the 2004-2005 dome-building eruption of Mount St. Helens, Washington* (No. 1750-14, pp. 281-300). US Geological Survey.

Dzurisin, D., Lisowski, M., Wicks, C. W., Poland, M. P., & Endo, E. T. (2006), Geodetic observations and modeling of magmatic inflation at the Three Sisters volcanic center, central Oregon Cascade Range, USA. *Journal of Volcanology and Geothermal Research*, 150(1-3), 35-54.

Dzurisin, D., Poland, M.P. & Bürgmann, R. (2002). Steady subsidence of Medicine Lake Volcano, Northern California, revealed by repeated leveling surveys. *Journal of Geophysical Research*, 107.

Ebmeier, S.K., Biggs, J., Mather, T.A., Elliott, J.R. Wadge, G. & Amelung, F. (2012). Measuring large topographic change with InSAR: Lava thicknesses, extrusion rate and subsidence rate at Santiaguito volcano, Guatemala. *Earth and Planetary Science Letters*, 335-336, 216-225.

Evans, J.R. & Zucca, J.J. (1988). Active high-resolution seismic tomography of compressional wave velocity and attenuation structure at Medicine Lake volcano, northern California Cascade Range. *Journal of Geophysical Research*, 93, 15,016-15,036.

Farr, T. G., & Kobrick, M. (2000), Shuttle Radar Topography Mission produces a wealth of data. *Eos, Transactions American Geophysical Union*, 81(48), 583-585.

Fitton, J.R., James, D., Kempton, P.D., Ormerod, D.S., & Leeman, W.P. (1988). The role of lithospheric mantle in the generation of late Cenozoic basic magmas in the western United States. *Journal of Petrology, Special Lithosphere Issue*, 331-349.

Fornaciai, A., Favalli, M., Karátson, D., Tarquini, S. & Boschi E. (2012). Morphometry of scoria cones, and their relation to geodynamic setting: A DEM-based analysis. *Journal of Volcanology and Geothermal Research*, 217-218, 56-72.

Fuis, G.S., Zucca, J.J., Mooney, W.D., & Milkereit, B. (1987). A geologic interpretation of seismic-refraction results in northeastern California. *Geological Society of America Bulletin*, 98, 53-65.

Gallant, E., Cole, L. Connor, C., Donovan, A., Molisee, D., Morin, J., Walshe, R. & Wetmore, P. (2021). Modelling eruptive source parameters in distributed volcanic fields. *Volcanica*, 4, 325-343.

Germa, A., Connor, L., Cañón-Tapia, E. & Le Corvec, N. (2013). Tectonic and magmatic controls on the location of post-subduction monogenetic volcanoes in Baja California, Mexico, revealed through spatial analysis of eruptive vents. *Bulletin of Volcanology*, 75, 1-14.

Gómez-Vasconcelos, M., Macías, J., Avellán, D., Sosa-Ceballos, G., Garduño-Monroy, V., Cisneros-Máximo, G., Layer, P., Benowitz, J., López-Loera, H., López, F. & Pertón, M. (2020).

The control of preexisting faults on the distribution, morphology, and volume of monogenetic volcanism in the Michoacán-Guanajuato Volcanic Field. *GSA Bulletin*, 132, 2455-2474.

Gonzalez-Santana, J., Wauthier, C. & Burns, M. (2022). Links between volcanic activity and flank creep behavior at Pacaya Volcano, Guatemala. *Bulletin of Volcanology*, 84, 84.

González, P.J., Tiampo, K.F., Camacho, A.G. & Fernández, J. (2010). Shallow flank deformation at Cumbre Vieja volcano (Canary Islands): Implications on the stability of steep-sided volcano flanks at oceanic islands. *Earth and Planetary Science Letters*, 297, 545-557.

Grose, T.L.T., Saucedo, G.J. & Wagner, D.L. (1989). The Walker Lane in Northeastern California. *Eos*, 70, 1362.

Grosse, P., Ramacciotti, M., Fochi, F., Guzmán, S., Orihashi, Y. & Sumino, H. (2020). Geomorphology, morphometry, spatial distribution and ages of mafic monogenetic volcanoes of the Peinado and Incahuasi fields, southernmost Central Volcanic Zone of the Andes. *Journal of Volcanology and Geothermal Research*, 401, 106966.

Guffanti, M. & Weaver, C. (1988). Distribution of Late Cenozoic Volcanic Vents in the Cascade Range: Volcanic Arc Segmentation and Regional Tectonic Considerations. *Journal of Geophysical Research*, 93, 6513-6529.

Hasenaka, T. (1994). Size, distribution, and magma output rate for shield volcanoes of the Michoacán-Guanajuato volcanic field, Central Mexico. *Journal of Volcanology and Geothermal Research*, 63, 13-31.

Hasenaka, T. & Carmichael, I. (1985). The cinder cones of Michoacán-Guanajuato, central Mexico: their age, volume and distribution, and magma discharge rate. *Journal of Volcanology and Geothermal*, 25, 105-124.

Hayward, B.W. & Hopkins J.L. (2019). Basis for modified ages of Auckland volcanoes in “volcanoes of Auckland: a field guide, 2019”. *Geocene*, 21, 2-10.

Henderson, S.T., Delgado, F., Elliott, J. Pritchard, M. & Lundgren, P. (2017). Decelerating uplift at Lazufre volcanic center, Central Andes, from A.D. 2010 to 2016 and implications for geodetic models. *Geosphere*, 13 (5), 1489-1505.

Hildreth, W. (2007). Quaternary magmatism in the Cascades – geologic perspectives. *U.S. Geologic Survey Professional Paper*, 1744, 125.

Hildreth, W., Fierstein, J. & Calvert, A. (2012). Geologic Map of the Three Sisters Volcanic Clusters, Cascade Range, Oregon. *U.S. Geological Survey Scientific Investigations Map 3186*, scale 1:24,000.

Hinde, A.L. & Miles, R.E. (1980). Monte carlo estimates of the distributions of the random polygons of the voronoi tessellation with respect to a poisson process. *Journal of Statistical Computation and Simulation* 10, 205–223.

Hooper, A. (2008), A multi-temporal InSAR method incorporating both persistent scatterer and small baseline approaches. *Geophysical Research Letters*, 35(16).

Hopkins, J., Wilson, C., Millet, M., Leonard, G., Timm, C., McGee, L., Smith, I. & Smith, E. (2017). Multi-criteria correlation of tephra deposits to source centres applied in the Auckland Volcanic Field, New Zealand. *Bulletin of Volcanology*, 79, 54-89.

Hopkins, J.L., Smid, E.R., Eccles, J.D., Hayes, J.L., Hayward, B.W., McGee, L.E., van Wijk, K., Wilson, T.M., Cronin, S.J., Leonard, G.S., Lindsay, J.M., Németh, K. & Smith I.E.M. (2021). Auckland Volcanic Field magmatism, volcanism, and hazard: a review. *New Zealand Journal of Geology and Geophysics*, 64, 1-22.

Hulen, J.B. & Lutz, S.J. (1999). Altered volcanic rocks as hydrologic seals on the geothermal system of Medicine Lake volcano, California. *Geothermal Research Council Bulletin*, 28 (7), 217-222.

Ide, H., & Kurita, T. (2017), Improvement of learning for CNN with ReLU activation by sparse regularization. In *2017 international joint conference on neural networks (IJCNN)*, 2684-2691.

Jaimes-Viera, M.C., Martin Del Pozzo, A.L., Layer, P.W., Benowitz, J.A. & Nieto-Torres, A. (2018). Timing the evolution of a monogenetic volcanic field: Sierra Chichinautzin, Central Mexico, *Journal of Volcanology and Geothermal Research*, 356, 225-242.

Jin, S., Homer, C., Yang, L., Danielson, P., Dewitz, J., Li, C., Zhu, Z., Xian, G. & Howard, D. (2019), Overall Methodology Design for the United States National Land Cover Database 2016 Products. *Remote Sensing*, 11(24), 2971.

Karlstrom, L., Wright, H.M. & Bacon, C. (2015). The effect of pressurized magma chamber growth on melt migration and pre-caldera vent locations through time at Mount Mazama, Crater Lake, Oregon. *Earth and Planetary Science Letters*, 412, 209-219.

Kereszturi, G., Cappello, A., Ganci, G., Procter, J., Németh, K., Del Negro, C. & Cronin, S.J. (2014). Numerical simulation of basaltic lava flows in the Auckland Volcanic Field, New Zealand-implication for volcanic hazard assessment. *Bulletin of Volcanology*, 76, 1-17.

Kinzler, R.J., Donnelly-Nolan, J.M. & Grove, T.L. (2000). Late Holocene hydrous mafic magmatism at the Paint Pot Crater and Callahan flows, Medicine Lake volcano, N. California and the influence of H₂O in the generation of silicic magmas. *Contributions to Mineralogy and Petrology*, 138, 1-16.

Kiyosugi K, Connor CB, Wetmore PH, Ferwerda BP, Germa AM, Connor LJ & Hintz AR (2012). Relationship between dike and conduit distribution in a highly eroded monogenetic volcanic field: San Rafael, Utah, USA. *Geology*, 40, 695-698.

- Kiyosugi, K., Connor, C.B., Zhao, D., Connor, L.J. & Tanaka, K. (2010). Relationships between volcano distribution, crustal structure, and P-wave tomography: an example from the Abu Monogenetic Volcano Group, SW Japan, *Bulletin of Volcanology*, 72, 185-204.
- Kumar, V. & Venkataraman, G. (2011), SAR interferometric coherence analysis for snow cover mapping in the western Himalayan region. *International Journal of Digital Earth*, 4(1), 78-90.
- Lary, D., Alavi, A., Gandomi, A. & Walker, A. (2016), Machine learning in geosciences and remote sensing. *Geoscience Frontiers*, 7, 3-10.
- Le Corvec, N., Bebbington, M., Lindsay, J. & McGee, L. (2013b). Age, distance, and geochemical evolution within a monogenetic volcanic field: Analyzing patterns in the Auckland Volcanic Field eruption sequence. *Geochemistry, Geophysics, Geosystems*, 14, 3648-3665.
- Le Corvec, N., Spörli, K., Rowland, J. & Lindsay, J. (2013a). Spatial distribution and alignments of volcanic centers: Clues to the formation of monogenetic volcanic fields. *Earth-Science Reviews*, 124, 96-114.
- Legrand, D., Pertou, M., Macías, J.L., Siebe, C., Pacheco, J., Chacón, F., Lermo, J., Quintanar, L. & Cisneros, G. (2023). Repeated seismic swarms near Parícutin volcano: precursors to the birth of a new monogenetic volcano in the Michoacán-Guanajuato volcanic field, México? *Bulletin of Volcanology*, 85, 1-15.
- Leonard, G.S., Calvert, A., Hopkins, J., Wilson, C., Smid, E., Lindsay, J. & Champion, D. (2017). High precision $^{40}\text{Ar}/^{39}\text{Ar}$ dating of Quaternary basalts from Auckland Volcanic Field, New Zealand, with implications for eruption rates and paleomagnetic correlations. *Journal of Volcanology and Geothermal Research*, 343, 60-74.
- Lin, J., Feng, X., Xiao, P., Li, H., Wang, J. & Li, Y. (2012), Comparison of Snow Indexes in Estimating Snow Cover Fraction in a Mountainous Area in Northwestern China. *IEEE Geoscience and Remote Sensing Letters*, 9(4), 725-729.
- Linnell, T., Shane, P., Smith, I., Augustinus, P., Cronin, S., Lindsay, J. & Maas, R. (2016). Long-lived shield volcanism within a monogenetic basaltic field: The conundrum of Rangitoto volcano, New Zealand. *GSA Bulletin*, 128, 1160-1172.
- Lohman, R. B., & Simons, M. (2005), Some thoughts on the use of InSAR data to constrain models of surface deformation: Noise structure and data downsampling. *Geochemistry, Geophysics, Geosystems*, 6.
- Lowenstern, J.B., Donnelly-Nolan, J., Wooden, J.L. & Charlier, B.L.A. (2003). Volcanism, plutonism and hydrothermal alteration at Medicine Lake volcano, California. Proceedings, Twenty-Eighth Workshop on Geothermal Reservoir Engineering. Stanford University, Stanford, California.
- Luhr, J. & Simkin, T. (1993). Parícutin: The volcano born in a Mexican cornfield. U.S. Geoscience Press.

- Lundgren, P., Poland, M., Miklius, A., Orr, T., Yun, S.H., Fielding, E., Liu, Z. Tanaka, A., Szeliga, W., Hensley, S. & Owen, S. (2013). Evolution of dike opening during the March 2011 Kamoamo fissure eruption, Kilauea Volcano, Hawai'i. *Journal of Geophysical Research: Solid Earth*, 118, 897-914.
- Lutz, T.M. & Gutmann, J.T. (1995). An improved method of determining alignments of point-like features and its implications for the Pinacate volcanic field, Mexico. *Journal of Geophysical Research*, 100, 17659-17670.
- Magill, C.R., McAneney, K.J. & Smith, I.E.M. (2005). Probabilistic assessment of vent locations for the next Auckland Volcanic Field event. *Math Geology*, 37, 227-242.
- Magna, T. Wiechert, U., Grove, T.L & Halliday, A.N. (2006). Lithium isotope fractionation in the southern Cascadia subduction zone. *Earth and Planetary Science Letters*, 250, 428-443.
- Massonnet, D., Rossi, M., Carmona, C., Adragna, F., Peltzer, G., Feigl, K., & Rabaute, T. (1993), The displacement field of the Landers earthquake mapped by radar interferometry. *Nature*, 364(6433), 138-142.
- Maxwell, a., Warner, T. & Fang F. (2018), Implementation of machine-learning classification in remote sensing: an applied review. *International Journal of Remote Sensing*, 39 (9), 2784-2817.
- Mazzarini, F. (2004). Volcanic vent self-similar clustering and crustal thickness in the northern Main Ethiopian Rift. *Geophysical Research Letters*, 31, 1-4.
- Mazzarini, F. & D'Orazio, M. (2003). Spatial distribution of cones and satellite-detected lineaments in the Pali Aike Volcanic Field (southernmost Patagonia): insights into the tectonic setting of a Neogene rift system. *Journal of Volcanology and Geothermal Research*, 125, 291-305.
- Mazzarini, F., Ferrari, L. & Isola, I. (2010). Self-similar clustering of cinder cones and crust thickness in the Michoacan-Guanajuato and Sierra de Chichinautzin volcanic fields, Trans-Mexican Volcanic Belt. *Tectonophysics*, 486, 55-64.
- Mazzarini, F., Fornaciai, A., Bistacchi, A. & Pasquarè, F. (2008). Fissural volcanism, polygenetic volcanic fields and crustal thickness in a compressional tectonic setting: the Payen Volcanic Complex on the central Andes foreland (Mendoza, Argentina). *Geochemistry, Geophysics, Geosystems*, 9, 1-17.
- Mazzarini, F., Le Corvec, N., Isola, I. & Favalli, M. (2016). Volcanic field elongation, vent distribution, and tectonic evolution of a continental rift: The Main Ethiopian Rift example. *Geosphere*, 12, 706-720.
- Mnich, M. & Condit, C. (2018). Basaltic magmatic mapping: A suggested methodology and the resulting petrologic and volcanic hazard implications from the Springerville Volcanic Field, east central Arizona. *Journal of Volcanology and Geothermal Research*, 366, 58-73.

- Mogi, K. (1958), Relations between the Eruptions of Various Volcanoes and the Deformations of the Ground Surfaces around them. *Bulletin of the Earthquake Research Institute*, 36, 99-134.
- Møller, J. (1994). Poisson-Voronoi tessellations. *Lectures on Random Voronoi Tessellations*, 87, 83-124.
- Molloy, C., Shane, P. & Augustinus, P. (2009). Eruption recurrence rates in a basaltic volcanic field based on tephra layers in maar sediments: Implications for hazards in the Auckland volcanic field. *GSA Bulletin*, 121, 1666-1677.
- Morfulis, M., Báez, W., Retamoso, S., Bardelli, L., Filipovich, R. & Sommer, C. (2020). Quantitative spatial distribution analysis of mafic monogenetic volcanism in the southern Puna, Argentina: Implications for magma production rates and structural control during its ascent. *Journal of South American Earth Sciences*, 104.
- Morse, S.A. (1980). Basalts and phase diagrams. New York, Springer-Verlag.
- O'Hara, D. & Karlstrom, L. (2023). The arc-scale spatial distribution of volcano erosion implies coupled magmatism and regional climate in the Cascades arc, United States. *Frontiers in Earth Science*, 11.
- O'Hara, D., Karlstrom, L. & Ramsey, D.W. (2020). Time-evolving surface and subsurface signatures of Quaternary volcanism in the Cascades Arc. *Geology*, 48, 1088-1093.
- Okada, Y. (1985). Surface deformation due to shear and tensile faults in a half-space. *Bulletin of the Seismological Society of America*, 75 (4), 1135-1154.
- Parker, A.L., Biggs, J. & Lu, Z. (2014). Investigating long-term subsidence at Medicine Lake Volcano, CA, using multitemporal InSAR. *Geophysical Journal International*, 199, 844-859.
- Pivarunas, A., Blatter, D., Muffler, L.J., Clynne, M., Calvert, A., Harrison, L. & Christiansen, R. (2023). Paleomagnetically defined brief lifespans for two large shield volcanoes in the Cascades Arc. *Journal of Volcanology and Geothermal Research*, 434.
- Poland, M. P., & de Zeeuw-van Dalzen, E. (2021), Volcano geodesy: A critical tool for assessing the state of volcanoes and their potential for hazardous eruptive activity. In *Forecasting and Planning for Volcanic Hazards, Risks, and Disasters* (pp. 75-115).
- Poland, M. P., & Lu, Z. (2008), Radar interferometry observations of surface displacements during pre-and coeruptive periods at Mount St. Helens, Washington, 1992–2005. *US geological survey professional paper*, 1750, 361-382.
- Poland, M., Bürgmann, R., Dzurisin, D., Lisowski, M., Masterlark, T., Owen, S. & Fink, J. (2006). Constraints on the mechanism of long-term, steady subsidence at Medicine Lake volcano, northern California, from GPS, leveling and InSAR. *Journal of Volcanology and Geothermal Research*, 150, 55-78.

Pozzobon, R., Mazzarini, F., Massironi, M. & Marinangeli, L. (2014). Self-similar clustering distribution of structural features on Ascræus Mons (Mars): implications for magma chamber depth. *Geological Society, London, Special Publications*.

Purcell, V., Reddin, E., Ebmeier, S.K., González, P.J., Watson, A., Morishita, Y. & Elliott, J. (2022). Nearly Three Centuries of Lava Flow Subsidence at Timanfaya, Lanzarote. *Geochemistry, Geophysics, Geosystems*, 23, 10.

Ramsey, D.W. & Siebert, L. (2017). Spatial and temporal database compilation of Holocene volcanic vents in the western conterminous United States. *International Association of Volcanology and Chemistry*.

Ripley, B.D. (1981) *Spatial Statistics*, Wiley, New York.

Ritter, J.R.R. & Evans, J.R. (1997). Deep structure of Medicine Lake volcano, California. *Tectonophysics*, 275, 221-241.

Rodríguez-Molina, S., González, P.J., Charco, M., Negredo, A.M. & Schmidt, D.A. (2021). Time-Scales of Inter-Eruptive Volcano Uplift Signals: Three Sisters Volcanic Center, Oregon (United States). *Frontiers in Earth Science*, 8, 1-19.

Roman, A. & Lundgren, P. (2023). Magma Transport and Storage Along Rift Zones Through Volcanic Conduits. *Journal of Geophysical Research: Solid Earth*, 128.

Rosen, P. A., Gurrola, E., Sacco, G. F., & Zebker, H. (2012), The InSAR scientific computing environment. In *EUSAR 2012; 9th European conference on synthetic aperture radar* (pp. 730-733). VDE.

Rosen, P.A., Hensely, S., Joughin, I.R., Li, F.K., Madsen, S.N., Rodriguez, E. & Goldstein, R. (2000), Synthetic aperture radar interferometry. *Proceedings of the IEEE*, 88, 333-382.

Rowe, M.C., Graham, D.W., Smid, E. & McGee, L. (2020). Unusually homogeneous helium isotope composition of the Auckland Volcanic Field and its implications for the underlying mantle. *Chemical Geology*, 545.

Rubin, A.M. & Pollard, D.D. (1987). Origins of blade-like dikes in volcanic rift zones. In: Decker, R.W., Wright, T.L., Stauffer, P.H. (Eds.), *Volcanism in Hawaii, USGS Professional Paper, 1350*, 1449-1470.

Runge, M., Bebbington, M., Cronin, S., Lindsay, J., Kenedi, C. & Moufti, M. (2014). Vents to events determining an eruption event record from volcanic vent structures for the Harrat Rahat, Saudi Arabia. *Bulletin of Volcanology*, 76, 1-16.

Sherrod, D. R., Scott, W. E., & Stauffer, P. H. (2008), *A volcano rekindled: The renewed eruption of Mount St. Helens, 2004-2006* (No. 1750). US Geological Survey.

Sigmundsson, F., Parks, M., Geirsson, H., Hooper, A., Drouin, V., Vogfjörð, K., Ófeigsson, B.G., Greiner, S.H.M., Yang, Y., Lanzi, C., Pascale, G., Jónsdóttir, K., Hreinsdóttir, S., Tolpekin, V., Fridriksdóttir, H.M., Einarsson, P. & Barsotti, S. (2024), Fracturing and tectonic stress drives ultrarapid magma flow into dikes. *Science*.

Silverman, B.W. (1986). Density Estimation for Statistics and Data Analysis. *Monographs on Statistics and Applied Probability*, London: Chapman and Hall.

Singh, D.K., Thakur, P. K., Prasad Naithani, B. & Kaushik, S. (2021), Quantifying the Sensitivity of Band Ratio Methods for Clean Glacier Ice Mapping. *Spatial Information Research*, 29(3), 281-295.

Stelten, M., Downs, D., Dietterich, H., Mahood, G., Calvert, A., Sisson, T. Zahran, H. & Shawali, J. (2018). Timescales of magmatic differentiation from alkali basalt to trachyte within the Harrat Rahat volcanic field, Kingdom of Saudi Arabia. *Contributions to Mineralogy and Petrology*, 173, 1-17.

Stephens, K. J., Wauthier, C., Bussard, R. C., Higgins, M., & LaFemina, P. C. (2020), Assessment of mitigation strategies for tropospheric phase contributions to InSAR time-series datasets over two Nicaraguan volcanoes. *Remote Sensing*, 12(5), 782.

Tanemura, M. (2003). Statistical distributions of Poisson Voronoi cells in two and three dimensions. *Forma*, 18, 221–247. MR2040084

Taye, M. M. (2023), Theoretical understanding of convolutional neural network: concepts, architectures, applications, future directions. *Computation*, 11(3), 52.

Till, C.B., Kent, A.J.R., Abers, G.A., Janiszewski, H.A., Gaherty, J.B. & Pitcher, B.W. (2019). The causes of spatiotemporal variations in erupted fluxes and compositions along a volcanic arc. *Nature Communications*, 10.

Valentine, G. A. & Perry, F. V. (2007). Tectonically controlled, time-predictable basaltic volcanism from a lithospheric mantle source (central Basin and Range Province, USA). *Earth and Planetary Science Letters*, 261, 201-216.

Valentine, G.A., Ort, M. & Cortés, J. (2021). Quaternary basaltic volcanic fields of the American Southwest. *Geosphere*, 17, 2144-2171.

Varugu, B. & Amelung, F. (2021). Southward growth of Mauna Loa's dike-like magma body driven by topographic stress. *Scientific Reports*, 11, 9816.

Wadge, G. & Cross, A. (1988). Quantitative methods for detecting aligned points: An application to the volcanic vents of the Michoacán-Guanajuato volcanic field, Mexico. *Geology*, 16, 815-818.

- Walter, S. & Dzurisin, D. (1989). The September 1988 earthquake swarm at Medicine Lake volcano, northern California. *Eos Transactions AGU*, 70 (43), 1189-1190.
- Węglarczyk, S. (2018). Kernel density estimation and its application. *ITM Web of Conferences*, 23, 37.
- Wells, R.E. & McCaffrey, R. (2013). Steady rotation of the Cascade Arc. *Geology*, 41, 1027-1030.
- Wicks, C.W., Dzurisin, D., Ingebritsen, S., Thatcher, W., Lu, Z. & Iverson, J. (2002). Magmatic activity beneath the quiescent Three Sisters volcanic center, central Oregon Cascade Range, USA. *Geophysical Research Letters*, 29 (7), 1122.
- Williams, S., Bock, Y. & Fang, P. (1998), Integrated satellite interferometry: Tropospheric noise, GPS estimates and implications for interferometric synthetic aperture radar products. *Journal of Geophysical Research*, 103, 27,051–27,067.
- Wittmann, W., Sigmundsson, F., Dumont S. & Lavallée, Y. (2017). Post-emplacement cooling and contraction of lava flows: InSAR observations and a thermal model for lava fields at Hekla volcano, Iceland. *Journal of Geophysical Research: Solid Earth*, 122 (2), 946-965.
- Wu, W., R. J. May, H. R. Maier, and G. C. Dandy (2013), A benchmarking approach for comparing data splitting methods for modeling water resources parameters using artificial neural networks, *Water Resources Research*, 49, 7598–7614.
- Yunjun, Z., Fattahi, H., & Amelung, F. (2019). Small baseline InSAR time series analysis: Unwrapping error correction and noise reduction. *Computers & Geosciences*, 133, 104331. doi: 10.1016/j.cageo.2019.104331
- Zebker, H. A., and Villasenor, J. (1992), Decorrelation in interferometric radar echoes, *IEEE Trans. Geosci. Remote Sens.*, 30, 950–959.
- Zhang, M., Wang, X., Shi, C. & Yan, D. (2019), Automated Glacier Extraction Index by Optimization of Red/SWIR and NIR/SWIR Ratio Index for Glacier Mapping Using Landsat Imagery. *Water* 2019, 11(6), 1223.
- Zhou, D. X. (2020), Theory of deep convolutional neural networks: Downsampling. *Neural Networks*, 124, 319-327.
- Zucca, J.J., Fuis, G.S., Milkereit, B., Mooney, W.D. & Catchings, R.D. (1986). Crustal structure of northeastern California. *Journal of Geophysical Research*, 91, 7359-7382.